AD-A042 784 HONEYWELL CORPORATE RESEARCH CENTER BLOOMINGTON MINN F/G 20/3
ADVANCED DEVELOPMENT ON GALLIUM PHOSPHIDE MATERIALS FOR SATELLI--ETC(U)
APR 77 P E PETERSEN, R G SCHULZE, M W SCOTT F33615-75-C-5244
UNCLASSIFIED HR-47108 AFML-TR-77-37 NL

1 OF 2
AD A042784



ADA042784

AFML-TR-77-37

(12)

ADVANCED DEVELOPMENT ON GALLIUM PHOSPHIDE MATERIALS FOR SATELLITE ATTITUDE SENSORS

Honeywell Inc.
Corporate Research Center
10701 Lyndale Avenue South
Bloomington, Minnesota 55420

April 1977

Technical Report AFML-TR-77-37
Final Technical Report for Period 15 May 1975 - 31 December 1976

Approved for public release; distribution unlimited

DISTRIBUTION STATEMENT A
Approved for public release;
Distribution Unlimited

DDC
RECEIVED
AUG 11 1977
B

AIR FORCE MATERIALS LABORATORY
AIR FORCE WRIGHT AERONAUTICAL LABORATORIES
AIR FORCE SYSTEMS COMMAND
WRIGHT-PATTERSON AIR FORCE BASE, OHIO 45433

DDC FILE COPY

NOTICE

When Government drawings, specifications, or other data are used for any purpose other than in connection with a definitely related Government procurement operation, the United States Government thereby incurs no responsibility nor any obligation whatsoever; and the fact that the Government may have formulated, furnished, or in any way supplied the said drawings, specifications, or other data, is not to be regarded by implication or otherwise as in any manner licensing the holder or any other person or corporation, or conveying any rights or permission to manufacture, use, or sell any patented invention that may in any way be related thereto.

This technical report has been reviewed and is approved for publication.

Robert L. Hickmott

ROBERT L. HICKMOTT
Project Monitor

FOR THE COMMANDER

W D G Frederick

WILLIAM G. D. FREDERICK
Chief
Laser and Optical Materials Branch
Electromagnetic Materials Division

Copies of this report should not be returned unless return is required by security considerations, contractual obligations, or notice on a specific document.

AIR FORCE - 14 JUL 77 - 150

UNCLASSIFIED

SECURITY CLASSIFICATION OF THIS PAGE (WHEN DATA ENTERED)

REPORT DOCUMENTATION PAGE

READ INSTRUCTIONS BEFORE COMPLETING FORM

1. REPORT NUMBER: AFML-TR-77-37
2. GOV'T ACCESSION NUMBER:
3. RECIPIENT'S CATALOG NUMBER:
4. TITLE (AND SUBTITLE): ADVANCED DEVELOPMENT ON GALLIUM PHOSPHIDE MATERIALS FOR SATELLITE ATTITUDE SENSORS.
5. TYPE OF REPORT/PERIOD COVERED: Final Technical Report, 15 May 75 - 31 Dec 76
6. PERFORMING ORG. REPORT NUMBER: HR-47108
7. AUTHOR(S): P.E. Petersen, R.G. Schulze M. W. Scott
8. CONTRACT OR GRANT NUMBER(S): F33615-75-C-5244
9. PERFORMING ORGANIZATIONS NAME/ADDRESS: Honeywell Corporate Research Center, 10701 Lyndale Avenue South, Bloomington, Minnesota 55343
10. PROGRAM ELEMENT, PROJECT, TASK AREA & WORK UNIT NUMBERS: Project - 7371; Task - 737102; Work Unit - 73710233
11. CONTROLLING OFFICE NAME/ADDRESS: Air Force Materials Laboratory, Air Force Systems Command, Wright Patterson AFB, Ohio 45433
12. REPORT DATE: April 1977
13. NUMBER OF PAGES: 142
14. MONITORING AGENCY NAME/ADDRESS (IF DIFFERENT FROM CONT. OFF.): 144p.
15. SECURITY CLASSIFICATION (OF THIS REPORT): UNCLASSIFIED
15a. DECLASSIFICATION DOWNGRADING SCHEDULE:
16. DISTRIBUTION STATEMENT (OF THIS REPORT): Approved for public release, distribution [redacted].

DISTRIBUTION STATEMENT A
Approved for public release;
Distribution Unlimited

17. DISTRIBUTION STATEMENT (OF THE ABSTRACT ENTERED IN BLOCK 20, IF DIFFERENT FROM REPORT):
18. SUPPLEMENTARY NOTES:
19. KEY WORDS (CONTINUE ON REVERSE SIDE IF NECESSARY AND IDENTIFY BY BLOCK NUMBER): III-V Compounds, GaP, Liquid Phase Epitaxy, Solution Growth, Photoconductivity

20. ABSTRACT (CONTINUE ON REVERSE SIDE IF NECESSARY AND IDENTIFY BY BLOCK NUMBER)

The objective of this research program is to develop the solution-growth technology of GaP so that crystals of sufficient size and uniformity can be produced for Air Force photodetector applications. To accomplish this objective, two growth techniques, bulk solution growth (BSG) and liquid phase epitaxy (LPE), have been developed.

LPE has been successfully developed as a crystal growth technique capable of producing high-performance GaP: Cu photoconductors. An advanced slider technique is used to grow 0.6 cm² layers. These layers have

DD FORM 1 JAN 73 1473 EDITION OF 1 NOV 55 IS OBSOLETE

UNCLASSIFIED

SECURITY CLASSIFICATION OF THIS PAGE (WHEN DATA ENTERED)

407 493

20. ABSTRACT (Continued)

been characterized by C-V and photoconductivity analysis. The spectral response of the photoconductivity of these LPE layers exhibits an extremely broad spectral response from 2.25 to 5.0 eV. Photoconductive gains in the range 10^4 to 10^5 have been measured. The photoconductive response times are in the 1 to 10 msec range, and spatial uniformity of ~10 percent over a 3-mm slit length has been achieved.

BSG is phosphorus diffusion-controlled growth from a gallium solution. The preferred variation of this technique provides an elemental phosphorus source rather than the compound GaP. The technique is called synthesis-solute-diffusion (SSD). During this program, the SSD technique was developed for the growth of single-crystal GaP. Single crystals as large as 1.2 cm diameter x 1 cm long were grown which were inclusion free. Dislocation densities $\leq 10^3$ cm^{-2} were measured.

The grown material has been evaluated by Hall, IR spectroscopy and capacitance techniques. Hall analysis has been used to (1) identify the principal impurities in the material, (2) identify the primary scattering mechanisms, (3) determine the degree of compensation and (4) show sample to sample uniformity. IR spectroscopy has been used especially for the identification of carbon in p-type GaP. Dark and photocapacitance measurements on Schottky barriers have been used to characterize the deep acceptors and electron traps in GaP.

PREFACE

This final report describes work performed by personnel of the Honeywell Corporate Research Center, 10701 Lyndale Avenue South, Bloomington, Minnesota 55420 during the period from 15 May 1975 through 31 December 1976 under Contract F33615-75-C-5244, Project 7371. The program was monitored by Dr. Robert J. Spry and Mr. Robert L. Hickmott, Air Force Materials Laboratory, Wright-Patterson Air Force Base, Ohio.

The program was directed toward the growth and evaluation of copper-doped gallium phosphide by liquid phase epitaxy and bulk solution growth. This investigation was conducted by Dr. P. E. Petersen (principal investigator), Mr. R. G. Schulze, Dr. M. W. Scott and Mr. S. R. Peterson with the technical assistance of Mr. D. W. Tuft and Mr. J. D. Hintgen.

ACCESSION for
NTIS White Section ☑
DDC Buff Section ☐
UNANNOUNCED ☐
JUSTIFICATION
BY
DISTRIBUTION/AVAILABILITY CODES
Dist. AVAIL. and/or SPECIAL
A

DDC
RECEIVED
AUG 11 1977
B

TABLE OF CONTENTS

SECTION		PAGE
I	INTRODUCTION	1
II	EXPERIMENTAL TECHNIQUES AND APPARATUS	4
	A. Bulk Solution Growth Apparatus	6
	B. Liquid Phase Epitaxial Growth Apparatus	11
	C. Material Evaluation — Techniques and Apparatus	16
	1. Photoconductivity	16
	2. Transport Measurements	18
	3. Infrared Spectroscopy	19
	4. Capacitance Spectroscopy	21
III	EXPERIMENTAL RESULTS	23
	A. Bulk Solution Growth	23
	B. Liquid Phase Epitaxial Growth	30
	C. Material Evaluation	45
	1. Photoconductivity	45
	2. Transport Measurements	60
	3. IR Spectroscopy	75
	4. Junction Capacitance Studies	77
	5. Etch Pit Density	86
IV	DISCUSSION	89
	A. Bulk Solution Growth	89
	B. Liquid Phase Epitaxial Growth	92
	C. Electrical and Optical Properties of GaP	93
	1. Photoconductivity	93
	2. Transport Measurements	99
	3. IR Spectroscopy	106

TABLE OF CONTENTS (Continued)

SECTION		PAGE
	4. Junction Capacitance Measurements	111
	5. Summary	116
V	PROGRESS AND ACCOMPLISHMENTS	119
VI	REFERENCES	120
APPENDIX A	Photoconductivity in Wide Bandgap Materials	122

LIST OF ILLUSTRATIONS

FIGURE		PAGE
1	Alternate growth techniques for bulk solution growth . . .	6
2	Furnace configuration and temperature profile for the BSG process using a cooling jet to establish the temperature gradient.	8
3	BSG apparatus using a graphite crucible and tip cooling	9
4	SSD apparatus using a graphite crucible and tip cooling	10
5	Common-source substrate LPE apparatus	12
6	LPE growth slider mechanism 2	12
7	LPE growth slider mechanism 3	14
8	LPE growth apparatus	14
9	*Photoconductivity measuring* apparatus schematic	17
10	High-resistivity Hall apparatus schematic	18
11	Photoconductivity system used with Digilab FTS-14 spectrometer	20
12	Capacitance-measuring apparatus	22
13	Wafers from BSG-22 growth run	27
14	LPE layers from (a) LPE-11-68 and (b) LPE-11-70	36
15	Grown layer from LPE-13-76	37
16	Cross-section of modified LPE slider mechanism 3	38
17	Surface topography of LPE-17-93	40
18	Surface topography of LPE-24-118	42
19	Spectral response for two LPE GaP:Cu samples. LPE-20-100 has an as-grown surface; LPE-18-95 has had an HCl etch	47
20	Photoconductive gain vs photon energy for LPE-11-69 GaP:Cu photoconductor	49

LIST OF ILLUSTRATIONS (Continued)

FIGURE		PAGE
21	Photosignal vs photon flux intensity at 2.7 eV for LPE-11-69 GaP:Cu photoconductor	49
22	Frequency dependence of the photosignal of LPE-11-69 GaP:Cu	50
23	Spatial uniformity of the photosignal for three slits on LPE-11-69 GaP:Cu	51
24	Photoconductive gain vs photon energy for LPE-23-117 GaP:Cu photoconductor	53
25	Photosignal vs photon flux intensity at 3.0 eV for LPE-23-117 GaP:Cu photoconductor	54
26	Frequency dependence of the photosignal of LPE-23-117 GaP:Cu	54
27	Spatial uniformity of the photosignal for two slits on LPE-23-117 GaP:Cu	55
28	Photoconductive gain vs photon energy for LPE-29-142 GaP:Cu photoconductor	56
29	Photosignal vs photon flux intensity at 3.0 eV for LPE-29-142 GaP:Cu photoconductor	57
30	Photosignal of LPE-29-142 at (a) 20°C and (b) 90°C. Scales are the same for both measurements	58
31	Optical quenching in LPE-18-95 GaP:Cu photoconductor	59
32	Photosignal vs photon flux intensity for a high resistivity (LPE-18-95) GaP:Cu photoconductor	61
33	Spectral response of a Schottky barrier photodiode fabricated on LPE-13-76	62
34	Carrier concentration divided by (temperature)$^{3/2}$ for two samples from BSG-10	66
35	Temperature dependence of the mobility for an n-type sample from BSG-10 ($n = 3 \times 10^{17}$ cm^{-3})	67

LIST OF ILLUSTRATIONS (Continued)

FIGURE		PAGE
36	Temperature dependence of the mobility for an n-type sample from BSG-15 ($n = 8 \times 10^{17}$ cm^{-3})	68
37	Mobility vs. temperature for three BSG samples. The theoretical curves for optical phonon scattering and ionized impurity scattering are included.	69
38	Carrier concentration divided by (temperature)$^{3/2}$ as a function of reciprocal temperature for four BSG growth runs	70
39	Hall coefficient vs. reciprocal temperature for four BSG growth runs	71
40	Resistivity vs. reciprocal temperature for four BSG growth runs	73
41	Temperature dependence of the mobility for four SSD samples	74
42	Temperature dependence of the mobility for an LPE 10-62 n-type sample	75
43	Absorption coefficient as a function of wave number for BSG-10 at 82 K and 5 K	76
44	Excitation spectrum of carbon acceptors in GaP in the far infrared.	78
45	Relative photoconductive response as a function of wave number for BSG-4 at 7 K showing the oscillatory behavior of the photoconductivity	79
46	Inverse capacitance squared vs. applied bias for five Au/GaP Schottky barriers on p-type SSD-3	80
47	Inverse capacitance squared vs. applied bias for three Schottky barriers on LPE-17-94	81
48	Inverse capacitance squared vs. applied bias for two Au/GaP Schottky barriers on LPE-25-129 (diodes 1 and 2 are 15 μm and 50 μm from the growth interface, respectively)	83
49	Conductance as a function of temperature at three different frequencies for a Au/GaP Schottky barrier on a BSG substrate	85

LIST OF ILLUSTRATIONS (concluded)

FIGURE		PAGE
50	Dependence of the capacitance on the energy of the probe radiation at three frequencies in a Au/GaP Schottky barrier (the sample is simultaneously illuminated with 2.8 eV radiation)	85
51	Change in capacitance of an LPE-25-129 Au/GaP Schottky barrier due to photoexcitation with less than bandgap energy radiation. Carrier concentration of the GaP = 3×10^{15} cm^{-3}	86
52	Etch pits in GaP LPE-17-93 (EPD - 3×10^4 cm^{-2})	88
53	Etch pits in GaP SSD-3 (EPD - 10^3 cm^{-2})	88
54	Bulk Solution Growth — Furnace gradient producing concave isotherms	91
55	Bulk Solution Growth — Flat furnace profile with tip cooling producing convex isotherms	91
56	Energy of the photoconductivity minima as a function of the minimum number (the intercept at 400 cm^{-1} gives the impurity ionization energy)	110
57	Band schematic of a Schottky barrier and the corresponding space charge distribution for three different bias conditions .	112
58	Frequency divided by (temperature)$^{3/2}$ as a function of reciprocal temperature for two Au/GaP Schottky Barriers	114
59	Equilibrium band schematic of a Schottky diode on an n-type substrate with deep donor and acceptor states.	115
60	Defect levels in gallium phosphide	117

LIST OF TABLES

TABLE		PAGE
1	Summary of GaP BSG crystal growth runs	24
2	Summary of GaP BSG and SSD crystal growth runs	26
3	Summary of LPE growth runs with slider mechanism 2 . . .	31
4	Summary of LPE growth runs with slider mechanism 3 . . .	32
5	Tabulation of Hall data (first half of program)	64
6	Tabulation of Hall data (second half of program)	65
7	Average value, $\bar{X}$, and standard deviation, S, for the photosignal in three GaP:Cu photoconductors	96
8	Spatial uniformity of samples from LPE-23-117	97
9	Comparison of the donor density determined from the Hall data and from the ionized impurity expression for the mobility	105
10	Summary of impurities found in GaP	107

SECTION I
INTRODUCTION

The gallium phosphide research program at Honeywell has established the technical feasibility of using copper-doped gallium phosphide (GaP:Cu) for the fabrication of high-performance visible radiation detectors. We have shown that these detectors can meet the requirements of the Air Force for space attitude reference systems. However, prior to research conducted under the program reported herein, problems still existed in obtaining adequate reproducibility, size, and uniformity of the GaP:Cu crystals. These limitations were primarily due to the random nucleation solution growth method which had been employed during the initial research. This growth process was selected for the early research due to its lack of complexity and ease of implementation.

The objective of the program reported herein was to further develop the GaP:Cu crystal growth process so that it could reproducibly yield material of quality suitable for the high-performance detector applications specified by the Air Force. To achieve this objective, we elected to further develop solution-growth techniques which, in addition to the excellent detector characteristics already demonstrated, have the potential to yield the required size and uniformity. It is well known that the Czochralski growth technique yields large-area GaP crystals. Our decision to further advance the solution-growth techniques was based on the following considerations:

- Excellent photoproperties had been observed in solution-grown GaP:Cu.
- To date, all reports of photoconductivity in non-solution-grown GaP:Cu give very long response times.
- GaP grown by the liquid encapsulated Czochralski (LEC) technique is not suitable for the direct fabrication of light-emitting diodes (LEDs), but is used as substrate material for subsequent liquid phase epitaxy (LPE) or vapor phase epitaxy (VPE) growth. The junction for the LED is formed in the epitaxially grown material.

- Even if adequate photoproperties could be achieved in LEC GaP:Cu, a significant research effort would still be required to develop reproducibility and uniformity with that process.

We have developed two complementary solution growth techniques: bulk solution growth (BSG) and liquid phase epitaxy (LPE). BSG is a phosphorus-diffusion-controlled growth from a gallium solution in a temperature gradient. The preferred variation of this technique provides an elemental phosphorus source rather than the compound GaP. The technique is called synthesis-solute-diffusion (SSD).

The research on these two growth approaches performed in the present program has been successful. The two variations of the bulk solution process, BSG and SSD, were developed for the purpose(s) of providing large area GaP:Cu crystals and/or providing solution grown substrates for LPE. During the program, it became clear that LPE was the best way to grow GaP:Cu photoconductor material. Therefore, the main objective of the bulk solution growth became the development of the method for the growth of crystals suitable for LPE substrates. This objective was achieved. SSD single-crystal GaP ingots as large as 1.2 cm diameter x 1 cm long were grown and were inclusion free and had a much lower dislocation density than typical Czochralski GaP.

During the course of this program, we successfully developed LPE as a crystal growth technique capable of producing large area high performance GaP:Cu photoconductors. The development proceeded from some initial feasibility experiments with a common source substrate apparatus to a slider technique and finally to an advanced version of the slider technique. With the advanced slider, we are able to reproducibly grow 0.6 cm^2 layers, most of which are smooth and flat enough for photoconductor fabrication.

In order to support the crystal growth experiments, a substantial material evaluation program was carried out. Experiments were conducted in the areas of (1) photoconductivity, (2) transport properties, (3) infrared absorption and (4) capacitance spectroscopy. As a result of this evaluation, the principal defects in GaP:Cu have been measured, including shallow donors and acceptors, electron traps and deep acceptors. The dominant scattering mechanisms at room temperature and below have been identified in GaP:Cu. Photoconductive gain, spectral response and response time measurements have shown that LPE has produced the highest performance GaP:Cu to date.

The balance of this report is contained in four major sections as follows:

- Section II is a description of the experimental techniques and apparatus employed throughout this work.
- Section III gives the experimental results obtained. We have purposefully tried to refrain from interpretation of the results in this section.
- Section IV is a discussion of the significance and, where possible, an interpretation of the results presented in Section III.
- Section V is a recapitulation of the significant accomplishments achieved during this program.

SECTION II
EXPERIMENTAL TECHNIQUES AND APPARATUS

The objective of this program is to develop a new process for the growth of Cu-doped gallium phosphide. Solution growth (i.e., precipitation of single-crystal GaP from a saturated gallium solution at a temperature 300 to 500°C below the melting point of the compound) was very deliberately selected at the inception of our GaP:Cu photoconductor work for the following reasons:

- The large body of scientific literature on photoluminescence and electroluminescence in GaP (and also GaAs) shows that solution-grown material and junctions made in solution-grown material have the smallest concentrations of defects and impurities.
- Experimental and theoretical determinations of the phase diagrams for GaP show that the Ga vacancy concentration (which has been correlated with nonradiative "killer center" concentration) decreases by 10^3 from the melting point of GaP to 1100°C.
- Previously reported photoconductive measurements in GaP:Cu prepared by other than solution-growth methods have shown response times much longer than the corresponding electron lifetimes.

Two methods, bulk solution growth (BSG) and liquid phase epitaxy (LPE), have been used to prepare undoped and Cu-doped GaP crystals. The rationale for the two aspects of this crystal growth program are shown below. The two methods are not seen as alternatives, but as two interdependent parts of the growth program.

Technique	Purpose
Bulk Solution Growth	To provide a possible method for the growth of large, uniformly doped GaP:Cu crystals which are suitable for LPE substrates.

Technique	Purpose
Liquid Phase Epitaxy	To provide large-area, uniformly doped GaP:Cu crystals with "as-grown" surfaces.

During the first part of the program, progress reported in AFML-TR-76-79(1) include the following:

- Improved LPE surface morphology and larger LPE area.
- Demonstration of sensitized and short-wavelength photoconductivity in GaP:Cu LPE layers.
- Design and construction of BSG apparatus.
- BSG growth of ~5-mm-diameter GaP single crystals.
- Demonstration of ampoule tip cooling as an important technique for enhancing single-crystal BSG growth.

Thus, having demonstrated the feasibility of our approach for the growth of large-area Cu-doped GaP for high-performance visible radiation detectors, we report here principally the results of work designed to further upgrade our growth process with some reference to earlier work[1] for illustration. Specifically, we have directed our efforts toward the following crystal growth objectives:

- Increased BSG crystal size, both in diameter and length.
- Improved single crystallinity of BSG crystals through use of modified ampoule tip cooling configurations for graphite crucibles.
- Development of the synthesis-solute-diffusion (SSD) variation of the BSG process.
- Modification of the slider mechanism for improved LPE layer flatness and smoothness.
- Improved control of Cu doping in LPE layers.

---

1 AFML-TR-76-79 Report on "Advanced Development on Gallium Phosphide Materials for Satellite Attitude Sensors," Contract F33615-75-C-5244.

A. BULK SOLUTION GROWTH APPARATUS

Two methods of crystal growth were performed in this program, bulk growth and LPE. We have investigated two variations of the bulk process. One starts with GaP and recrystallizes it from a gallium solution. The other starts by compounding the GaP from phosphorus vapor and gallium and then recrystallizing it. These two variations are called bulk solution growth (BSG) and synthesis-solute-diffusion (SSD) growth, respectively, and are illustrated schematically in Figure 1. The SSD method is preferred since it starts with the elements Ga and P whose purities are more rigorously specified by suppliers than is the purity of commercially available GaP. However, developing the furnace configuration and other important elements of the growth system which are common to both BSG and SSD was done much more efficiently using the BSG method. The first 22 runs were BSG, then the SSD method was begun.

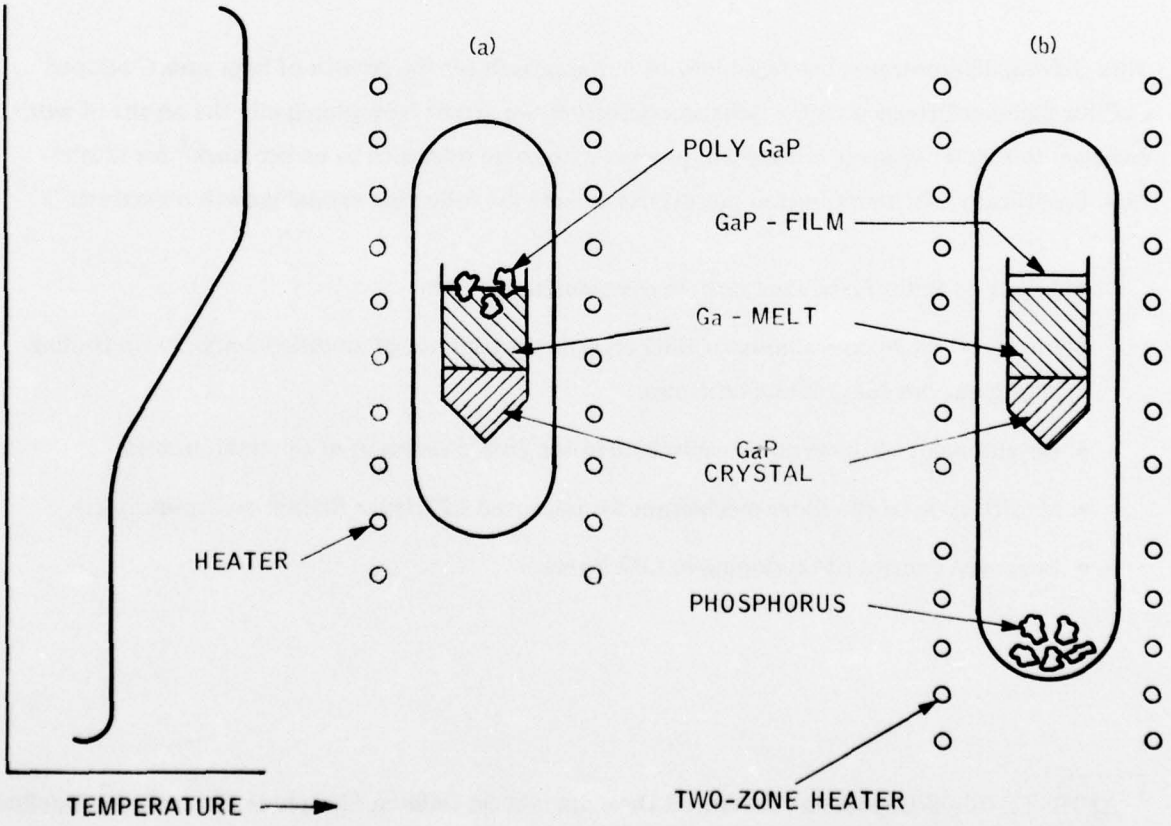


Figure 1. Alternate growth techniques for bulk solution growth.

As mentioned earlier, in our previous program, important improvements were made in the way in which the temperature gradient was established in the melt so as to achieve a convex growth interface which promotes single-crystal growth. This was achieved by using an isothermal furnace environment combined with forced air cooling of a carefully restricted portion of the tip of the growth ampoule. These experiments were initially done with quartz as shown in Figure 2 rather than with a graphite crucible because of the ease of varying the quartz crucible. During the remainder of the work, the tip cooling technique was applied to the graphite crucible which was machined from a special semiconductor grade (DFP-3-2) of a high-purity graphite by Poco Graphite Inc.[a]

The configuration is shown schematically in Figure 3. The cup-shaped piece, which forms the GaP seed retainer and bottom of the graphite crucible, was machined to provide a close fit over the cooling dimple in the quartz ampoule. It is important to establish as low a thermal resistance as possible between the cooling gas stream and the GaP seed and Ga column.

For the SSD method, the same graphite crucible was used except for one run which used a quartz crucible. For SSD, however, the crucible cap is removed and a quartz cup for the phosphorus is located in the ampoule above the crucible. This arrangement is shown in Figure 4.

For SSD growth, the furnace also had to be modified to provide a lower temperature zone of about 400°C for the phosphorus. The vapor pressure of phosphorus at 400°C is approximately 300 Torr. During the growth run, the temperatures at the locations T_p, T_1 and T_2 were recorded. The graphite crucible is cleaned by etching in $HCl:H_2O:HNO_3$ in the ratio 2:2:1 at 50°C. It is then successively rinsed in deionized distilled water, acetone, methanol and, finally, hot deionized distilled water.

The Amersil[b] fused quartz ampoules, sealing plugs and phosphorus cups were cleaned with detergent and water followed by acetone, methanol and a cleaning solution of $H_2O:HF:HNO_3$ in the ratio 5:2:3. After 10 rinses with deionized distilled water, the ampoule, along with the graphic crucible which had been cleaned as previously described, is vacuum baked at 1150°C for $\sim$ 3 hr. The 1150°C bake removed any residual hydroxyl radicals.

---

[a] Poco Graphite Inc., 1601 South State Street, Decatur, Texas 76234.

[b] Amersil, Inc., 685 Ramsey Avenue, Hillside, New Jersey 07205.

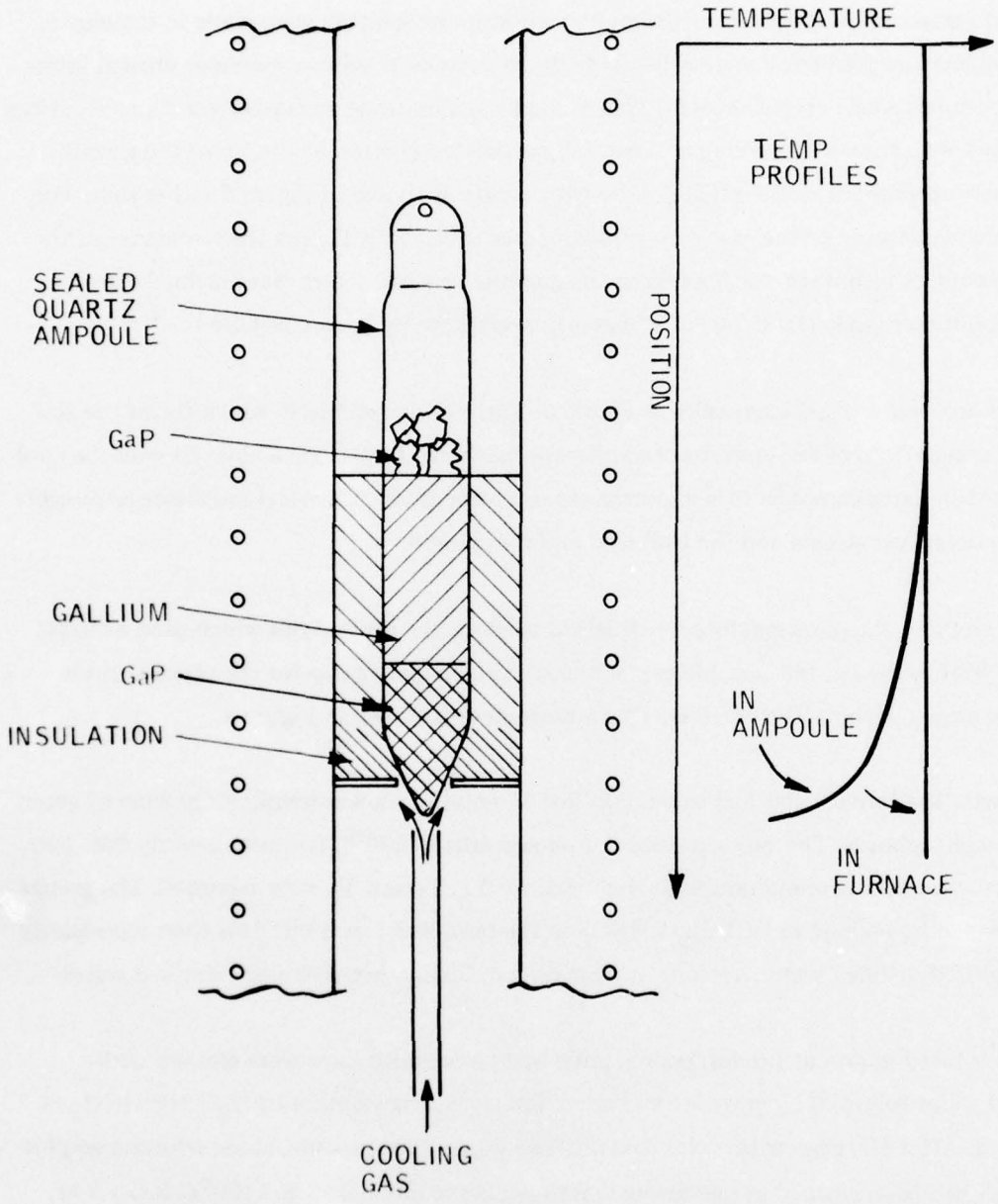


Figure 2. Furnace configuration and temperature profile for the BSG process using a cooling jet to establish the temperature gradient.

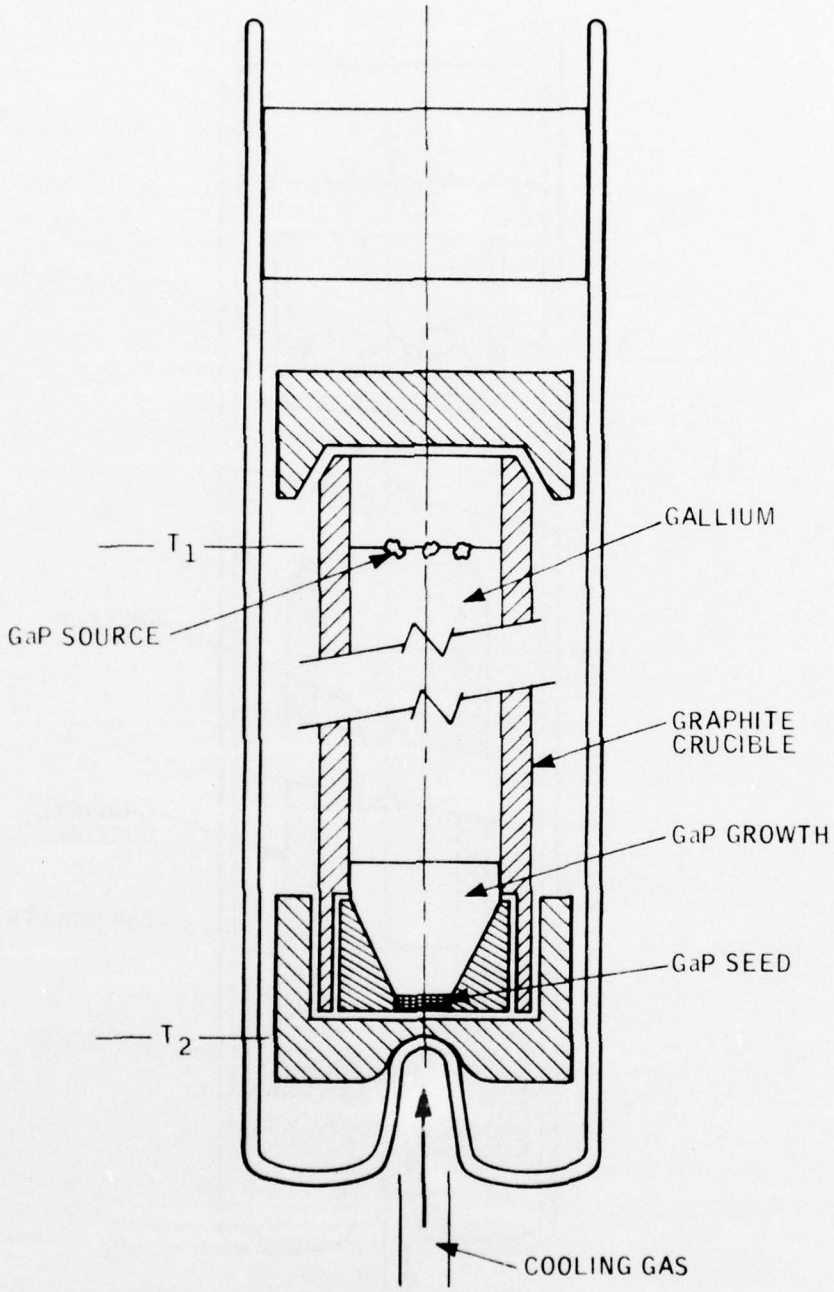


Figure 3. BSG apparatus using a graphite crucible and tip cooling.

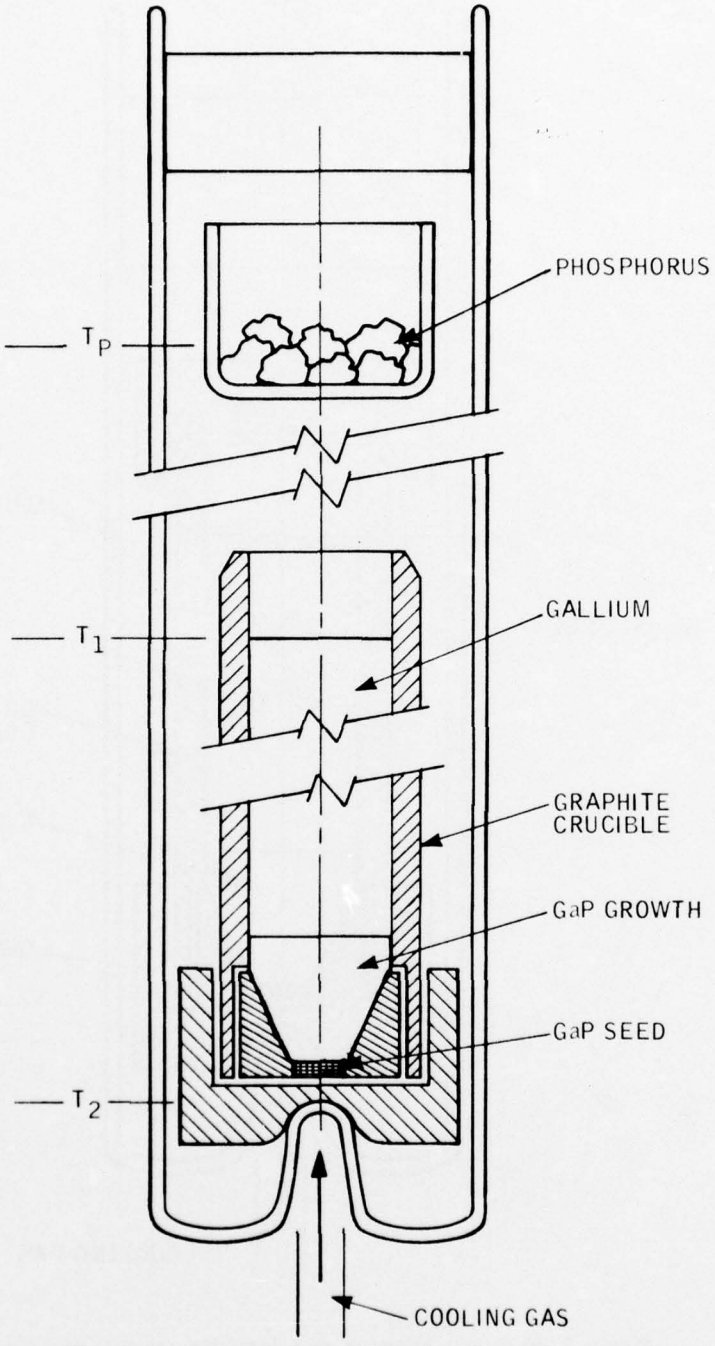


Figure 4. SSD apparatus using a graphite crucible and tip cooling.

The 99.9999 % pure Ga for the BSG and SSD runs is obtained from Eagle-Picher Industries[c]. 99.9999% pure red phosphorus is obtained from Atomergic Chemicals Corporation. The glass phosphorus ampoule is stored in a dessicator after opening. GaP $\langle \bar{1}\,\bar{1}\,\bar{1} \rangle$ seed crystals were cut from Czochralski ingots purchased from Cambridge IMANCO[d]. The seed crystals were further prepared by removing saw cut damage by lapping with 3.0 μm alumina on glass, 3.0 μm alumina on cloth and free etching in dilute aqua regia ($HCl:H_2O:HNO_3$ in the ratio 2:2:1) at 45°C. The final rinses are with deionized distilled water.

After loading the Ga, GaP source, GaP seed and phosphorus (if used), the ampoule is evacuated to $\sim 10^{-5}$ Torr using an oil-free sputter-ion sorption vacuum system and sealed off. The growth process has been carried out for from 5 to 17 days.

B. LIQUID PHASE EPITAXIAL GROWTH APPARATUS

Two LPE growth methods were used, a common-source substrate technique and a slider technique, although only a few runs were made with the first, which is illustrated in Figure 5. With this method, a single piece of Czochralski GaP acts both as the source of GaP to saturate the Ga during heat up and as the substrate on which LPE crystal growth occurs during cool down.

The slider method was used for all the remaining runs. One of the slider mechanisms (mechanism 2)[e] employed in this technique is shown in Figure 6. All of the parts are machined from pyrolytic graphite stock obtained from Union Carbide Corporation[f].

---

[c] Eagle-Picher Industries, Inc., PO Box 737, Quapaw, Oklahoma 74363.

[d] Cambridge IMANCO Division, Cambridge Instrument Inc., 40 Robert Pitt Drive, Monsey, New York 10952.

[e] Slider mechanism 1 was designed and constructed during an earlier program. Slider mechanisms 2 and 3 are improved versions of this first design.

[f] Union Carbide Corporation, Carbon Products Division, 120 South Riverside Plaza, Chicago, Illinois 60606.

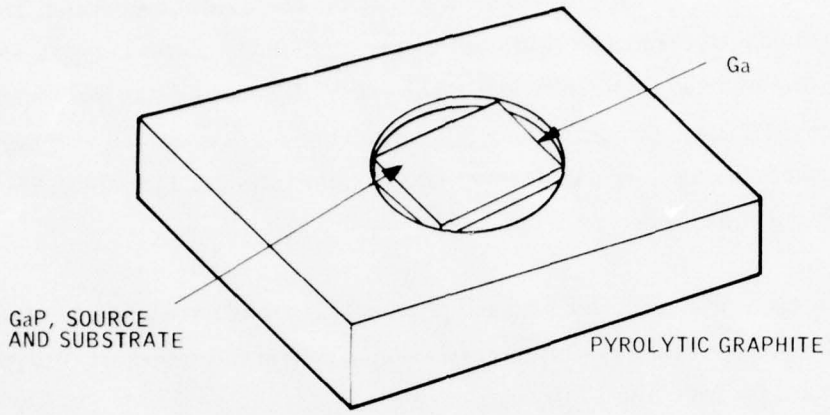


Figure 5. Common-source substrate LPE apparatus.

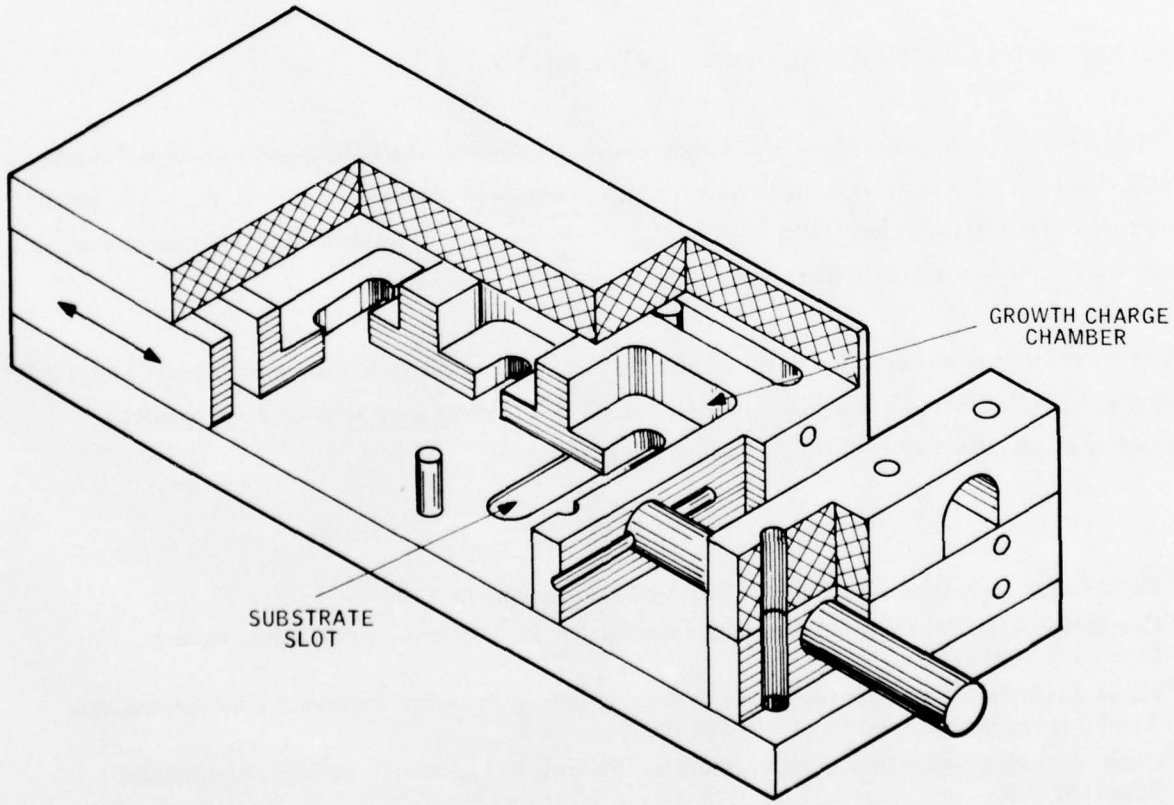


Figure 6. LPE growth slider mechanism 2.

The experience gained using the common source-substrate technique and slider mechanism 2 is covered more fully in AFML-TR-76-79[1]. An advanced slider mechanism was designed and built on the basis of that experience. Slider mechanism 3, shown in Figure 7, was machined from a special semiconductor grade (DFP-3-2) of high-purity graphite by Poco Graphite Inc. Compared to previous designs which we have used, the slider shown in Figure 7 incorporates the following improved features:

- Isotropic graphite which is less fragile than pyrolytic graphite.
- Freedom from the constraints imposed by the very large anisotropic thermal conductivity and expansion coefficient of pyrolytic graphite.
- Capacity for six substrates.
- Larger area LPE layer capability (4.7 mm x 12.7 mm).
- A cooling cavity located in the graphite directly below the substrate slots which is used to establish a temperature gradient across the growth interface.
- A gallium-well machined in the graphite directly over the cooling cavity to reduce lateral thermal gradients.

The addition of a cooling cavity is the most significant improvement in the design of this new slider. A well-controlled temperature gradient across the substrate-melt growth interface is necessary for the growth of smooth LPE layers.

The furnace growth tube and associated fittings are shown schematically in Figure 8. A single-ended (to minimize the possibility of leaks) Coors alumina tube[g] was placed inside a special stainless steel alloy tube. This alloy, RA333, will withstand cyclic operation to 1100°C. The stainless steel tube is a safety feature which prevents an explosion in the event the alumina tube cracks during use of a high-percentage-hydrogen growth atmosphere.

---

[1] AFML TR-76-79, Report on "Advanced Development on Gallium Phosphide Materials for Satellite Attitude Sensors," Contract F33615-75-C-5244.

[g] Coors Porcelain Company, 600 9th Street, Golden, Colorado 80401.

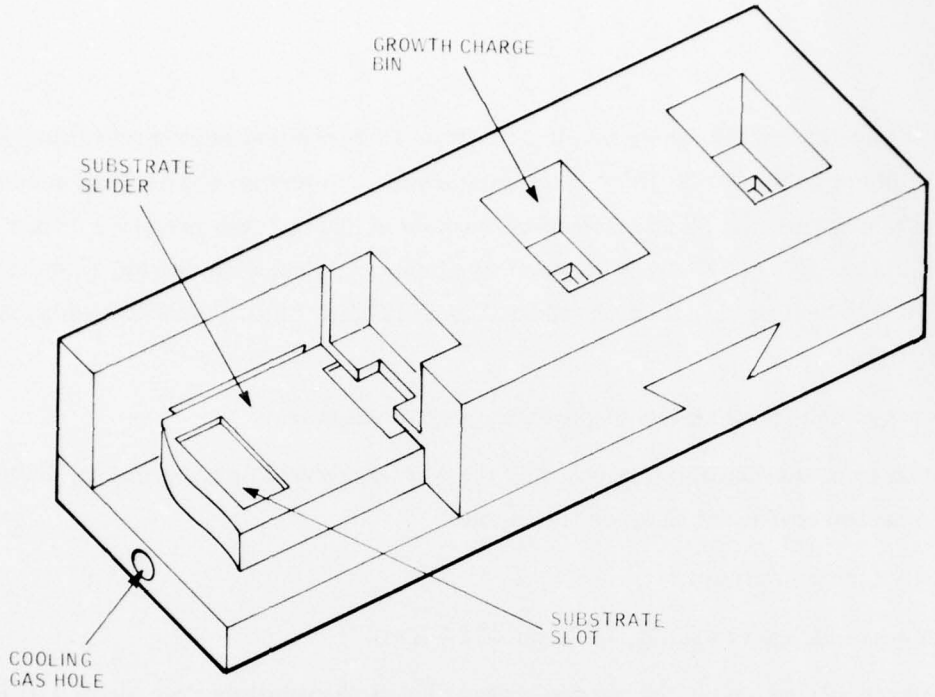


Figure 7. LPE growth slider mechanism 3.

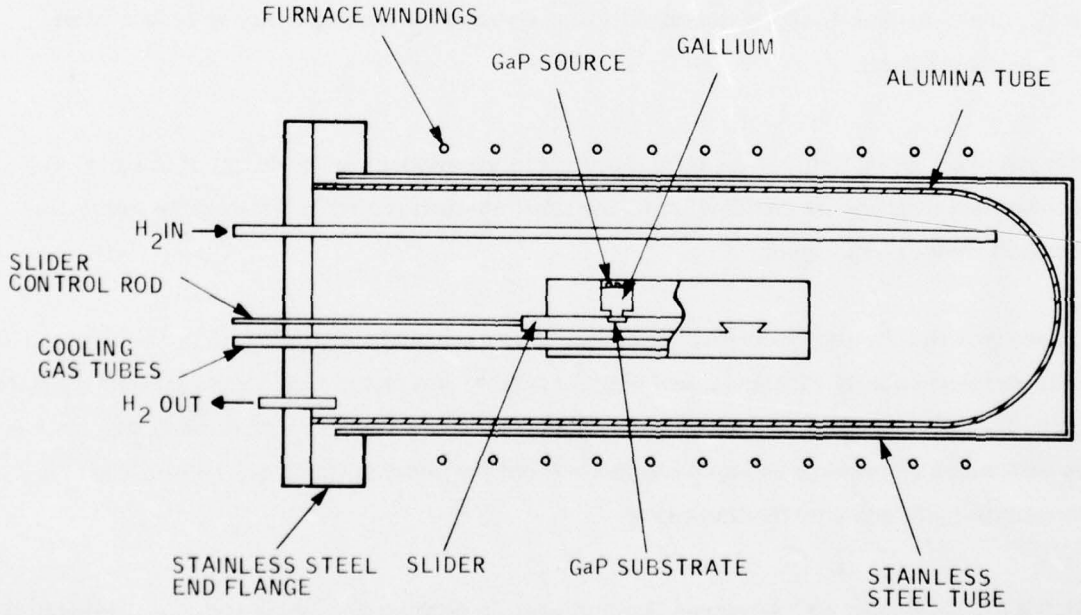


Figure 8. LPE growth apparatus.

All of the substrates used for LPE growth in this program were cut from three different Czochralski ingots purchased from Cambridge IMANCO. Some of the GaP had been precut into wafers by the supplier and the rest was cut into wafers using 0.005-in. wire saw and 600-mesh silicon carbide abrasive. Typically, the wafers were mounted on a flat glass lapping block with beeswax and hand lapped to a predetermined thickness using 3-μm aluminum oxide on glass. The wafers are then chemical-mechanically polished by removing $\sim$0.002 in. of material with a 1% Br-methanol solution using a Multipol lapping machine and a polyurethane lap. The feed rate of the 1% Br-methanol solution does not appear to be critical; about 80 drops/min. gives good results.

The wafers are removed from the glass lapping block and dipped in melted beeswax for protection. The wafers are remounted on glass slides and cut to appropriate size for use as substrates. Chloroform is a useful solvent for beeswax and is the principal solvent used for final cleaning. Just before loading into the slider, the substrates are free etched for $\sim$15 min. at 80°C in a stirred potassium ferricyanide etch [0.5M KOH, 1.0M $K_3Fe(CN)_6$]. The wafers are rinsed in deionized distilled water and blown dry with nitrogen. The substrates are immediately loaded in the slider and the liquid gallium metal, GaP source material and Cu dopant (if used) are placed in the growth bins. The gallium is from Eagle-Picher and is 99.99999% pure; the copper is 99.999% pure and was obtained from Materials Research Corporation[h] and from Inlab Materials[i]. The GaP source material was of several types depending on the purpose of the particular run. Undoped polycrystalline porous GaP was obtained from Monsanto[j]. Undoped Czochralski single material (the same as the material used for substrates) was obtained from Cambridge IMANCO, as previously mentioned. Polycrystalline ingot GaP was also obtained from Cambridge IMANCO. Sulfur-doped Czochralski single crystal GaP was purchased from General Electric Corporation[k].

The slider works in the following way. Ga and GaP (and Cu dopant if used) are put in the growth charge chambers; lapped and polished GaP substrates are placed in the substrate slots. The sliding

---

[h]Materials Research Corporation, Orangeburg, New York 10962.

[i] Inlab Materials, PO Box 269, Utica, New York 13503.

[j] Monsanto, Electronic Materials, PO Box 8, St. Peters, Missouri 63376.

[k]General Electric Corporation, Miniature Lamp Products Department, Nela Park, Cleveland, Ohio 44112.

member (the middle one) is positioned so that the growth charge columns are not over the substrates. The assembly is raised to about 1050°C in a palladium-diffused H_2 atmosphere. After the system has reached thermal equilibrium, the slider is moved to position the growth charge over the substrate. The furnace is cooled at 2.5°C/hr. for a time corresponding to the desired layer thickness. A 15°C cool down produces a layer which is $\sim$ 15 μm thick. After the growth, the slider is returned to the starting position, and the furnace is cooled to room temperature for removal of the LPE layers.

C. MATERIAL EVALUATION—TECHNIQUES AND APPARATUS

Four major techniques were used to evaluate the material grown during this program:

- Photoconductivity
- Transport measurements
- Infrared spectroscopy
- Capacitance spectroscopy.

This section discusses the techniques and apparatus generally employed in each of these measurements.

1. Photoconductivity

GaP samples, grown from solution, are generally oriented in the $\langle \bar{1},\bar{1},\bar{1} \rangle$ direction. We used the phosphorous surface for photoconductivity studies. This surface is easily distinguished from the gallium surface because a polishing etch such as potassium ferricyanide polishes the phosphorus side while putting a matte finish on the gallium side. We used the alloyed Ag:Te/Ni contact which was developed earlier for the low-resistance contact to the material[2, 3]. The active area of the photoconductor was defined by the contacts in the so-called "slit" configuration (length $>>$ width).

[2]H. Nakatsuka, A. J. Domenico and G. L. Pearson, Solid-State Electron. 14, 849 (1971).
[3]R. G. Schulze and P. E. Petersen, J. Appl. Phys. 45,5307 (1974).

The apparatus used in the photoconductivity studies is shown schematically in Figure 9. A xenon arc lamp in conjunction with a Perkin Elmer Model 98 spectrometer [l] is the illumination source. The sample is mounted on a three-way translation stage in a shielded light-tight box. Reflecting optics focus the radiation on the sample. The photoconductive signal can be read out in three different ways. The d-c photocurrent is measured with a Keithley electrometer[m]. For an a-c photomeasurement, a current-sensitive preamplifier in conjunction with a PAR-124 lock-in amplifier is used.

The response to a single radiation pulse can be displayed on a storage oscilloscope by using the PAR-114 signal conditioning amplifier [n] to amplify the signal. The optical system is calibrated with a EG&G calibrated photodiode[o].

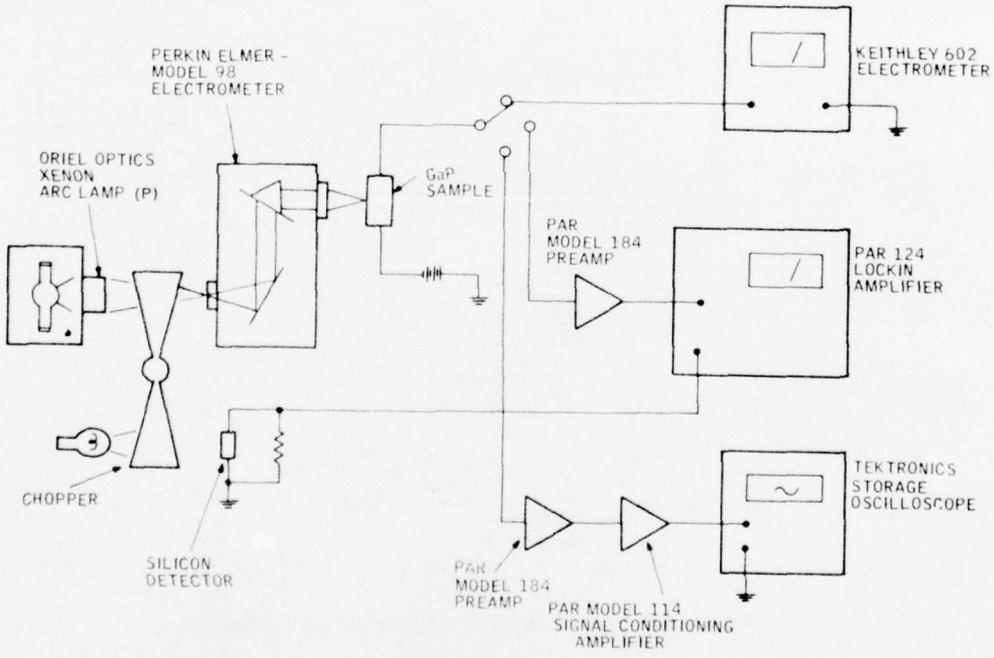


Figure 9. Photoconductivity measuring apparatus schematic.

[l] Perkin Elmer Corporation, Main Avenue, Norwalk, Connecticut 06856.

[m] Keithley Instruments, 28775 Aurora Road, Cleveland, Ohio 44139.

[n] Princeton Applied Research Corporation, PO Box 2565, Princeton, New Jersey 08540.

[o] EG&G Inc., 160 Brookline Avenue, Boston, Massachusetts 02215.

[p] Oriel Corporation of America, 15 Market Street, Stamford, Connecticut 06902.

2. Transport Measurements

Three different systems are available for Hall and resistivity analysis. In each of these systems, the sample is mounted in a Janis Model 8DT research dewar[q] which can be cooled to the liquid helium temperature. The sample temperature can be controlled to 0.1 K with a Lakeshore Cryotronics DT-500 temperature controller[r]. The first system requires a standard bridge-shaped Hall sample and is capable of measuring samples with resistances up to $10^9\ \Omega$. To enable measurement of samples with arbitrary shapes, we constructed the necessary apparatus to make van der Pauw Hall measurements. In addition, we have a Hall system which is capable of making measurements on samples with resistances up to $10^{13}\ \Omega$[s]. A schematic of this apparatus is shown in Figure 10.

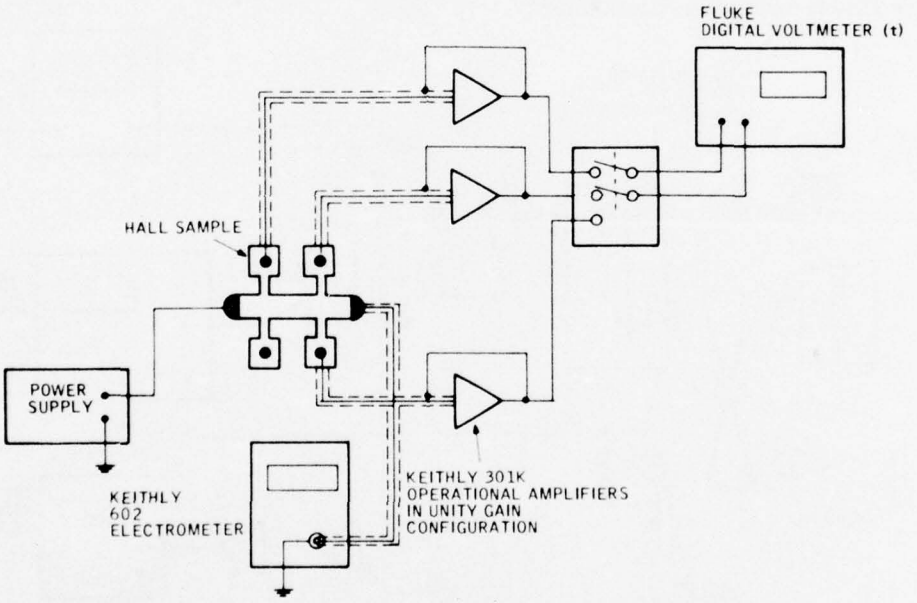


Figure 10. High-resistivity Hall apparatus schematic.

---

[q] Janis Research Co., Inc., 22 Spencer, Stoneham, Massachusetts 02180.

[r] Lakeshore Cryotronics Inc., 9629 Sandrock Tr., Eden, New York 14057.

[s] Dr. Patrick Hemenger of the Air Force Materials Laboratory assisted in the design of this system.

[t] John Fluke Manufacturing Company, Inc., PO Box 7428, Seattle, Washington 98133.

3. Infrared Spectroscopy[u]

The infrared transmittance spectra of GaP crystals were obtained with the Digilab FTS-14 Fourier transform spectrometer[v]. The samples were attached to the cold finger of an Air-Products Cryo-Tip helium cryostat[w] and cooled to about 8 K for measurement. The sample temperature was determined by using a Au-7 atomic percent Fe-versus-Cu thermocouple soldered to the cold finger. The sample surfaces were lapped and polished before measurement, with no chemical surface treatment being used. In most cases, the samples were lapped with a 1.0° taper in the thickness to eliminate interference fringes in the transmitted signal. The energy transmitted by the sample is measured and divided by the energy transmitted by the cryostat system without the sample. The sample and reference energy spectra are measured sequentially, so the transmittance is limited in accuracy by the stability of the spectrometer system and by the accuracy with which the cryostat can be repositioned between measurements. The reproducibility is generally better than 5%.

To obtain accurate measurements of the impurity concentration by infrared spectroscopic measurements, the absorption cross-section of characteristic lines of the impurity have to be determined. This is accomplished by first correlating the optical measurements with electrical determinations of carrier concentration on a few samples. Once this has been done, carrier concentrations can generally be determined to a precision of about $\pm$ 50%. This procedure of calibration has been done for a number of shallow donors, but has not been completed for carbon doped material.

The photoconductivity system we have adapted for the FTS is shown schematically in Figure 11. The sample is cooled in the helium cryostat where the temperature can be varied from 300 K to about 5 K. The photocurrent is amplified and filtered with a PAR-114 signal conditioning amplifier used in conjunction with either the PAR-116 voltage preamplifier or the PAR-184 current-sensitive preamplifier. The latter is used when the sample resistance becomes greater than about $10^6\ \Omega$. The signal from these amplifiers is then further processed by the digital data system of the spectrometer.

[u] The IR Spectroscopy measurements reported herein were funded by Honeywell.

[v] Digilab Inc., 237 Putnam Avenue, Cambridge, Massachusetts 02139.

[w] Air Products and Chemicals, Inc., Allentown, Pennsylvania 18103.

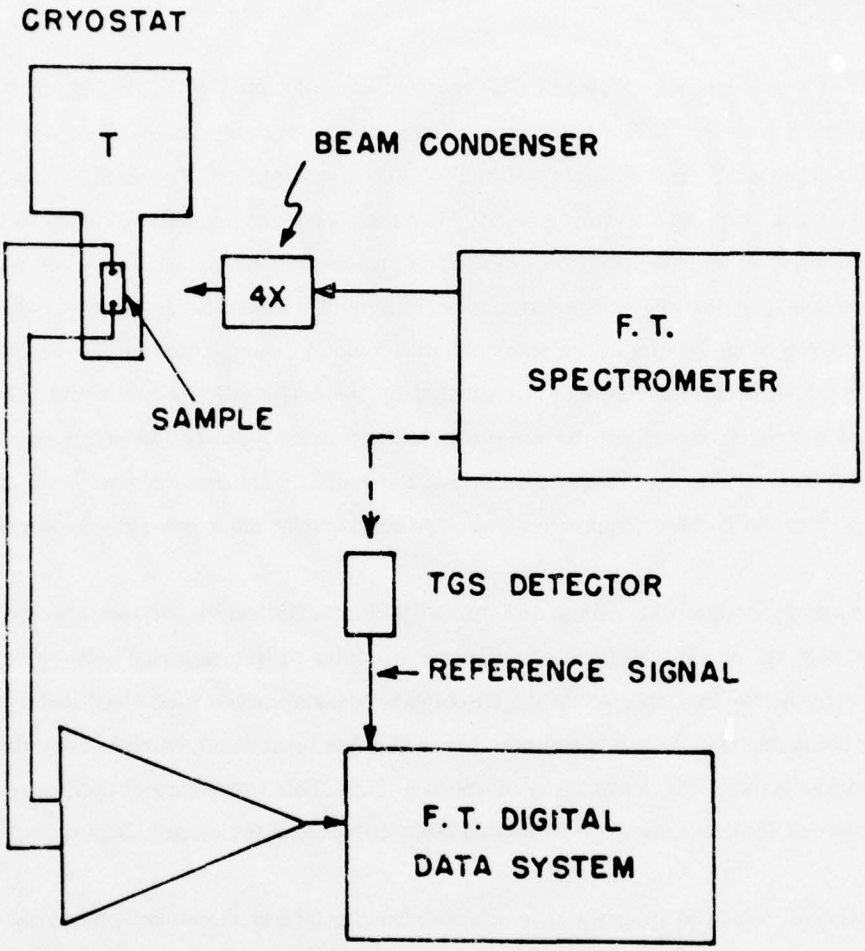


Figure 11. Photoconductivity system used with Digilab FTS-14 spectrometer.

To obtain the relative photoconductive response, the energy spectrum is measured with a triglycine sulphate detector. A Harrick beam condenser[x] with reflective optics is used along with a specially modified cryostat system to increase the power density incident on the sample. The beam condenser provides a 4x decrease in the optical beam diameter at the focal point.

Extrinsic photoconductivity measurements of impurities generally have the disadvantage of not providing quantitative information on the concentration of the impurities. This technique is far more sensitive than the transmittance measurements, so it is extremely useful for detecting the presence of trace amounts of impurities. From a practical standpoint, this technique is also useful in a new crystal growth area where there are limitations on the size of the samples available. With the beam-condensing optics of the spectrometer, a small sample can be measured which could not be handled by the standard transmittance techniques.

4. Capacitance Spectroscopy

A schematic of the capacitance measuring apparatus is shown in Figure 12. The lock-in amplifier is balanced with a standard low-loss capacitor in the circuit. The a-c measuring bias is supplied by the reference output of the lock-in. The unknown is then substituted for the standard, and a measurement of the in-phase and quadrature components of the current through the sample yield respectively the equivalent parallel capacitance and conductance of the unknown. The d-c sample bias can be varied from 0 to 250 V. Measurements can be made over a frequency range from 100 to 2×10^5 Hz. The sample is mounted in a cryogenic dewar so the temperature can be varied from room temperature to 77 K. In addition, it is possible to illuminate the sample with two different radiation sources, so it is possible to use this system for double-source photocapacitance measurements.

[x]Harrick Scientific Corporation, Croton Dam Road, PO Box 867, Ossining, New York 10562.

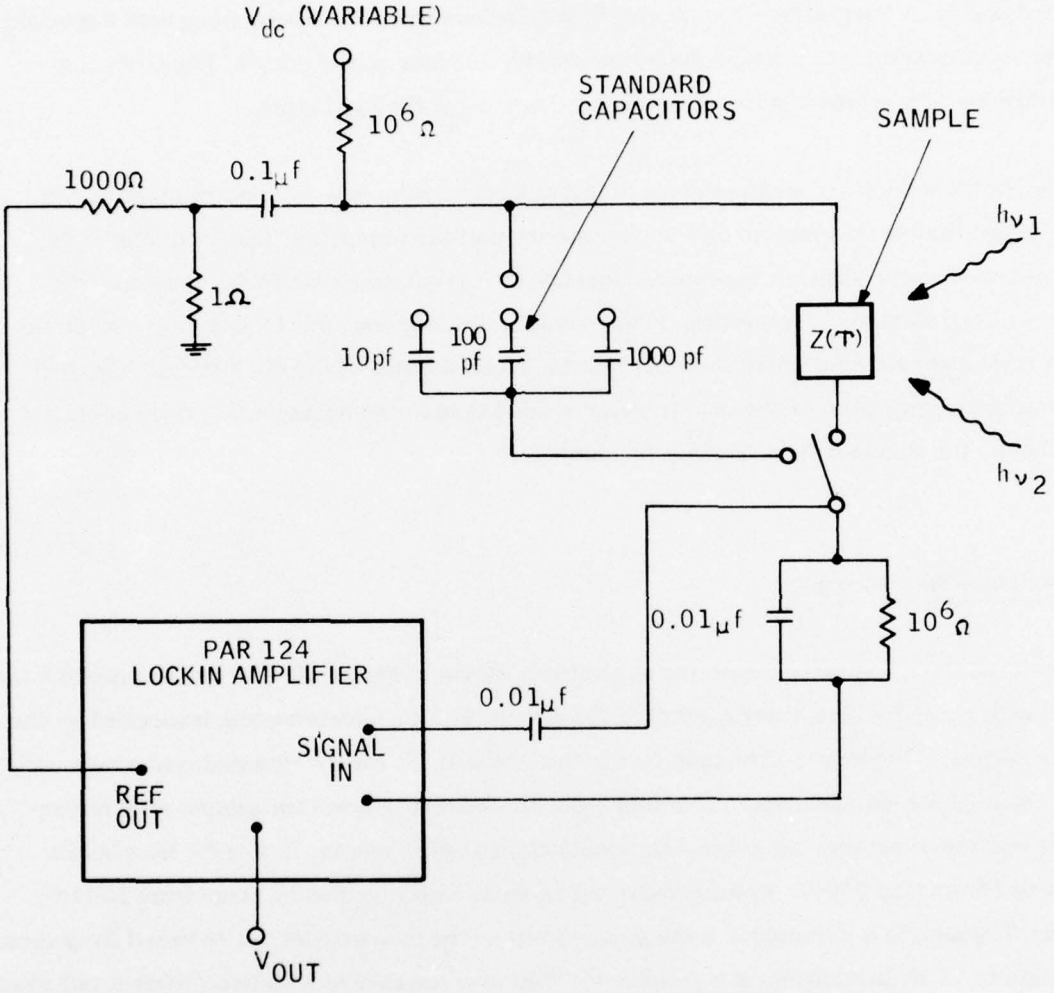


Figure 12. Capacitance-measuring apparatus.

SECTION III
EXPERIMENTAL RESULTS

The objective of the GaP materials development program is to improve the growth process in order to increase yield, size and uniformity of GaP:Cu crystals. The experimental results presented in this section show an iterative progression from the initial design of the BSG apparatus through its development into the SSD method. The LPE growth advances from the preliminary common source-substrate experiments through two versions of LPE slider apparatus. The results of the first 19 BSG runs and 11 LPE runs, reported more completely in AFML-TR-76-79[1], are summarized here to give the background leading to the following results which are presented in more detail. When feasible, we have evaluated the material grown, using the methods described in Section II. The experimental results are discussed in Section III. Section IV discusses the implications and conclusions which can be drawn from interpretation of these results.

A. BULK SOLUTION GROWTH[y]

The 19 BSG runs which were reported in AFML-TR-76-79 are summarized in Table 1. One of the principal results of this series of growths was the establishment of a flat furnace temperature profile with ampoule tip cooling as a successful method for promoting single-crystal growth. A more detailed analysis of this method is presented in Section IV.

The ampoule tip cooling experiments were started with BSG-15 and continued through BSG-19 using quartz crucibles. It is easier to modify the heat flow pattern in a quartz crucible than in a graphite crucible. This series of growth runs clearly demonstrated the presence of a convex growth interface. As growth proceeded, the ingot became increasingly single crystal.

---

[1] AFML-TR-79 Report, "Advanced Development on GaP materials for Satellite Attitude Sensors," Contract F33615-75-C-5244.

[y] Growth runs BSG 19-21 were funded by Honeywell.

TABLE 1.

SUMMARY OF GaP BSG CRYSTAL GROWTH RUNS

Run Number	Time (Days)	Starting Material	Crucible Temperature (°C)		Results
			Top	Bottom	
BSG-1A	---	Monsanto polyporous chunk (M.PPC)	---	---	Broken crucible.
BSG-1B	6	M.PPC	963	888	No growth; excessive vapor transport out of unsealed crucible.
BSG-2A	6.5	M.PPC	Broken thermocouples		Sealed crucible in sealed tube; tube broken; small growth.
BSG-2B	1.5	M.PPC	1000	870	Regrowth of unopened crucible from BSG-2A; no outer tube; no growth.
BSG-2C	4.5	M.PPC	1140	993	4-mm-long polycrystalline growth.
BSG-3	6	M.PPC	1118	914	No growth; insufficient starting material.
BSG-4	3.5	M.PPC	1117	921	3-mm-long growth, 3 or 4 single crystals.
BSG-5	11.5	M.PPC	1117	920	No growth; excessive vapor transport of GaP to crucible plug.
BSG-6	4	M.PPC	1099	883	Crucible shortened; vapor transport eliminated; 6-mm-long polycrystalline growth.
BSG-7	4.5	M.PPC	1050	924	6-mm-long void-free polycrystalline growth; crucible loaded into hot furnace.
BSG-8	5	GE Czochralski, sulfur doped $\sim 10^{18}$ cm^{-3}	1058	920	11-mm-long void-free polycrystalline growth.
BSG-9	---		---	---	Furnace core burned out.
BSG-10	11.5		1059	935	2-cm-long single crystal.
BSG-11	11	Same as BSG-8 and 4.8 mole % Cu	1063	907	Crucible expanded; polycrystalline growth filled with inclusions; first copper doping experiment.
BSG-12	10	GE Czochralski, sulfur doped $\sim 10^{18}$ cm^{-3}	1060	935	First graphite crucible run; polycrystalline hollow-cone-shaped growth.
BSG-13	9	IMANCO Czochralski and 6.0 mole % Cu	1059	935	8-mm-long polycrystalline growth with some inclusions, plus 9-mm-long polycrystalline growth with many inclusions.
BSG-14	13	GE Czochralski, sulfur doped $\sim 10^{18}$ cm^{-3}	1059	790	Second graphite crucible run; air cooling of low-temperature end of growth tube; polycrystalline hollow-cone-shaped growth much like BSG-12.
BSG-15	10.5	Same as BSG-14 and 5.0 mole % Cu	1071	Broken thermocouples	Quartz crucible with air cooling of tip; growth started up from tip; aggregate of several small crystals.
BSG-16	3	Same as BSG-14	1144	986	Quartz crucible-no furnace gradient forced air tip cooling; polycrystalline growth did not start at tip.
BSG-17	12	Same as BSG-14	1140	995	Same arrangement as BSG-16 with increased tip cooling 1.5-cm-long ingot increasingly single crystal toward top; convex growth interface.
BSG-18	12.5	IMANCO Czochralski and 6.0 mole % Cu	1110	920	Quartz crucible-furnace gradient, no cooling; polycrystalline growth 2.5-cm long.
BSG-19	11.5	M.PPC	1135	1009	Same arrangement as BSG-17; ingot 1.6-cm long; increasingly single-crystal toward tip; convex growth interface.

BSG-20 and succeeding growth runs are summarized in Table 2.

Run BSG-20 was the second attempt to use the graphite crucible with ampoule tip cooling. The first attempt, BSG-14, failed because of inadequate thermal conductance between the cooled tip of the ampoule and the growth column. BSG-20 used the modified ampoule tip and crucible bottom configuration shown in Figure 3. A $\langle \bar{1}\bar{1}\bar{1} \rangle$ oriented and lapped and polished Czochralski seed crystal was used. During the run, the collar which confines the cooling gas to the tip of the ampoule broke. This resulted in a very polycrystalline growth.

Run BSG-21 was essentially a repeat of BSG-20 with an improved cooling tip collar and with the cone-shaped base of the graphite crucible bored out to 0.5 in. from the original 0.020 in. This results in a much larger seed area under the growth solution. The results were excellent. A single-crystal growth occurred over the entire area of the seed crystal, and the growth interface is convex upward. As discussed later in this section, Hall measurements showed BSG-21 to be p-type.

Run BSG-22 was the same as BSG-21 except that IMANCO polydense ingot GaP was used instead of Monsanto polyporous chunk and the growth time was doubled. The purpose of the experiment was to see if the starting material was responsible for the p-type doping found in BSG-21. Although a disrupted cooling tip flow may have been responsible for the development of a lopsided growth interface (at least late in the run), a 1-cm-diameter single crystal was achieved. Wafers cut from the crystal are shown in Figure 13. Electrical measurements, discussed later in this section, showed BSG-22 also to be p-type, thus giving no evidence of the role of the starting material in the p-type doping.

Since the p-type dopant has been identified as carbon, we have turned our attention to other possible sources. The graphite crucible might be suspect. It has been shown[z], however, that the use of Poco graphite in contact with a Ga-GaAs solution leads to carbon contamination of no more than $10^{14} cm^{-3}$.

Two other more likely possibilities were found. In all previous runs, the graphite crucible had been cleaned in solvents and had not been baked out at greater than 500°C prior to loading; 500°C is

[z] R. A. Logan, Bell Telephone Laboratories, private communication.

TABLE 2.

SUMMARY OF GaP BSG AND SSD CRYSTAL GROWTH RUNS

Run Number	Time (Days)	Starting Materials				Temperature (°C)			Results
		GaP Charge	GaP Seed	P_4	Ga	T_1	T_2	T_p	
BSG-20	5	Monsanto polyporous chunk (M.PPC) 99969	IMANCO-2 Czochralski N_d-N_a~5 x 10^{16} cm^{-3}	N/A	Eagle-Picher 7-9's A-331-I	1148	964	N/A	Tip cooling disrupted by broken collar resulted in very poly-crystalline growth.
BSG-21	5	M.PPC	IMANCO-2 Czochralski N_d-N_a~5 x 10^{16} cm^{-3}	N/A	Eagle-Picher 7-9's A-331-I	1131	1112	N/A	Bottom of graphite crucible bored to 0.5-inch diameter to expose larger seed area. Convex growth interface; single crystal approximately 1-cm-diameter.
BSG-22	10	IMANCO polydense ingot (I.PDI) R-246/L2	IMANCO-2 Czochralski N_d-N_a~5 x 10^{16} cm^{-3}	N/A	Eagle-Picher 7-9's A-331-I	1125	1094	N/A	Lopsided growth front (possible tip cooling leak), but 1-cm-diameter single crystal grown.
SSD-1	7	None	IMANCO-2 Czochralski N_d-N_a~5 x 10^{16} cm^{-3}	Galland-Schlei-singer 6-9's C-8076	Eagle-Picher 7-9's A-331-I	1104	1054	375	First SSD run. Seed dissolved before Ga could saturate with P_4; growth polycrystalline, but convex and improving with growth time.
SSD-2	17	None	None	Galland-Schlei-singer 6-9's C-8076	Eagle-Picher 7-9's A-331-I	1123	1082	340	Tip cooling supply interrupted; polycrystalline growth, but improving with growth time. GaP charge and seed omitted to assess inherent purity.
SSD-3	14	IMANCO-2 and 1% GE (sulfur doped)	IMANCO-2 Czochralski N_d-N_a~5 x 10^{16} cm^{-3}	Galland-Schlei-singer 6-9's C-8076	Eagle-Picher 7-9's A-331-I	1124	1090	401	Largest single crystal grown-1.2 cm diameter x 1.0 cm long.
SSD-4	10	None	None	Galland-Schlei-singer 6-9's C-8076	Eagle-Picher 7-9's A-331-I	1130	1083	400	First use of evapor-ion vacuum system. Material still p-type.
SSD-5	11	None	None	Galland-Schlei-singer 6-9's C-8076	Eagle-Picher 7-9's A-331-I	1125	---	401	Quartz crucible and evapor-ion evacuation. n-type material.

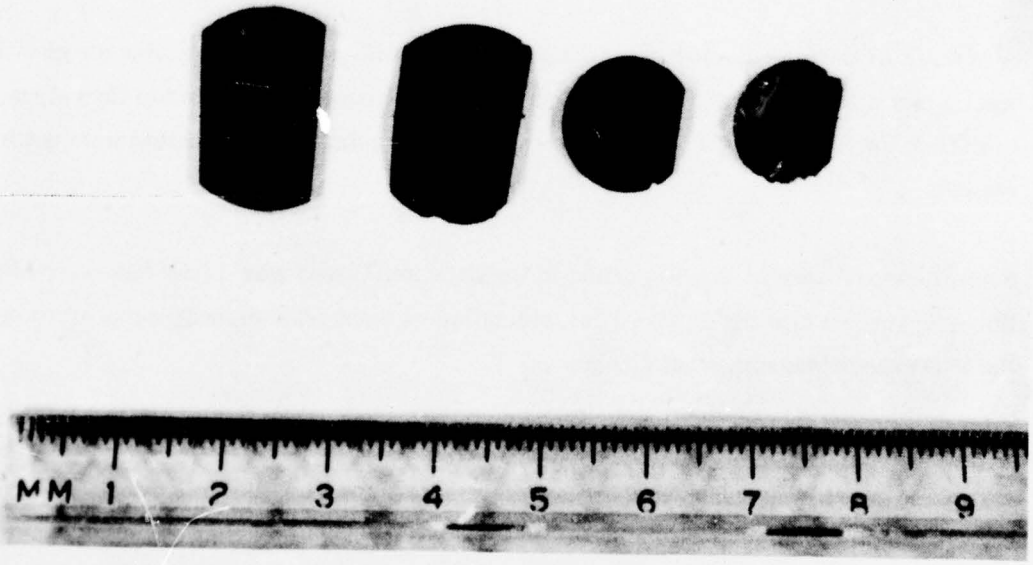


Figure 13. Wafers from BSG-22 growth run.

significantly below the growth temperature. Residual solvents could be responsible for the carbon doping. Provisions were made for discontinuation of solvent rinsing and for vacuum bake-out at 1100°C. Another possibility is backstreaming of oil from the vacuum system that has been used for evacuating the ampoules prior to seal-off.

Run SSD-1 was the first attempt to use the synthesis-solute-diffusion (SSD) growth method. The same graphite used in the BSG runs was used with a quartz ampoule modified to hold a quartz cup for the phosphorus supply as shown in Figure 4. The Czochralski GaP seed dissolved in the Ga during heatup before the phosphorus vapor source could saturate the Ga. It was clear that GaP had to be dispersed in the Ga in order to prevent the seed from dissolving. This starting GaP will have to be prepared from an unseeded SSD run if the purity of the total process is to be held at the highest level.

As a result of the seed dissolving in SSD-1, the growth was polycrystalline, but the growth interface was convex upward. Therefore, the growth was less polycrystalline at the top than at the beginning of nucleation. Single-crystal pieces sufficiently large to permit Hall evaluation were cut from the growth.

Since the seed dissolved, any impurities in the Czochralski seed would have been carried into solution and regrown into the crystal. Thus, evaluation of the crystal impurity concentration due to the SSD process was somewhat ambiguous.

Run SSD-2 was designed to eliminate this ambiguity by eliminating the seed crystal. While a polycrystalline growth was anticipated as a result of not using a seed, SSD-1 showed that large enough crystals would probably be available for Hall evaluation. The tip cooling air supply was disrupted during this 17-day run, resulting in a very polycrystalline growth over about half of the volume of the crystal. However, since the cooling tip air supply was restored before the end of the run, the growth interface was convex upward and the size of the crystals was increasing toward the top of the growth. Single crystals were cut from SSD-2 of sufficient size for Hall evaluation.

The Hall measurements showed the material from SSD-2 to be p-type at $\sim 10^{17} cm^{-3}$ with an activation energy suggesting carbon as the primary acceptor. The most likely source of the carbon

was the oil diffusion vacuum system used to evacuate the ampoules prior to seal-off. An evapor-ion vacuum system was constructed to replace the oil diffusion system, but was not ready to be used until SSD-4.

Run SSD-3 used both a seed crystal and a GaP charge to prevent dissolution of the seed as had occurred in SSD-1. The GaP charge was principally undoped Czochralski ingot with about 1% sulfur-doped Czochralski GaP added. The growth run was very successful in terms of ingot size and crystallinity. The seed crystal did not dissolve and, as a result, a single crystal ingot 1.2 cm diameter x 1 cm long was grown. At the end of the 1 cm length, the growth became polycrystalline, indicating a possible limit to the extent of the convex isotherms in the Ga melt. Hall analysis showed the material to be p-type at $\sim 6.6 \times 10^{16} cm^{-3}$ with a 0.040 eV activation energy, again suggesting carbon as the residual acceptor impurity.

Run SSD-4 was the first growth run to use the evapor-ion vacuum system for evacuation prior to ampoule seal-off. Also, the graphite crucible was given a double 1150°C vacuum bake-out in its quartz ampoule prior to loading. No seed or charge GaP was used since the purpose of the run (and that of SSD-5 which followed) was to assess the purity limits of the growth apparatus with as few possible sources of carbon contamination as possible. Since no seed crystal was used, the growth was polycrystalline, but single crystals of sufficient size for Hall evaluation were cut from the ingot. The material was again p-type.

Although the graphite cannot directly introduce carbon into the melt, any residual oxygen or water vapor in the ampoule will react with the graphite to give CO, which can dissolve in the melt and dope the GaP crystal with carbon. Since other sources of carbon had been eliminated in SSD-4, SSD-5 was designed to use a quartz crucible instead of graphite. Since the graphite crucible should be retained, the more desirable course would be to eliminate the source of water vapor or oxygen. However, in order to test the hypothesis, it was much easier to replace the graphite crucible. Other growth parameters for SSD-5 were held the same as SSD-4. The results substantiated the hypothesis; the material was n-type.

A comparison with earlier BSG runs which used quartz ampoules and persistently gave p-type material is appropriate. The ampoules for those runs were all evacuated with an oil diffusion

vacuum system which we believe was also a source of carbon contamination. It is clear that in order to use a graphite crucible and avoid carbon doping, one must eliminate oxygen and water vapor as well as prevent hydrocarbon contamination in the growth ampoule.

The BSG and SSD runs have shown that we have developed a growth process that can provide single-crystal, solution-grown GaP with substantially larger crystal size than the random nucleation method. These crystals are large enough for LPE substrates.

B. LIQUID PHASE EPITAXIAL GROWTH

A series of Cu-doped LPE common-source substrate growth runs was carried out at the beginning of the program to demonstrate, with a minimum of effort, that GaP could be doped with Cu via LPE. These experiments were successful in that compensated photosensitive GaP was grown; however, as expected, the grown surfaces were irregular with many growth steps and steep ridges ~1 mm high at the edge. The technique was dropped in favor of the slider LPE technique. The slider shown in Figure 6 was used for runs LPE-1 through LPE-9. It produced layers 3 mm x 8 mm on slightly larger substrates.

Runs LPE-1 through LPE-9 are summarized in Table 3. During the course of these runs, several design improvements were incorporated in a new slider, previously described and shown in Figure 7. This slider (Number 3) can grow larger areas (4.7 mm x 12.7 mm) and has a hole in the base for introducing cooling gas. Although the LPE growth cycle uses a cool-down to precipitate GaP from solution, it is generally believed that it is necessary to maintain the substrate somewhat cooler than the melt to prevent dendritic growth which can result from constitutional super cooling. The LPE growth runs performed with slider mechanism 3 are listed in Table 4.

LPE-10 was the first run with the new slider mechanism 3. Both doped and undoped growth charges were prepared. Undoped source material, Monsanto polyporous chunk, was used for the first time for all layers except LPE-10-65. With the new stainless steel safety tube encasing the alumina growth tube, 100% palladium-diffused hydrogen was used as the growth ambient. The slider base

TABLE 3.

SUMMARY OF LPE GROWTH RUNS — Slider No. 2

Run Number	Growth Temperature (°C)			Substrate Orientation	Substrate Number	Mole % Cu	Atmosphere	GaP Source	Substrate GaP	Results
	Start	Stop								
LPE-1	1008	700	2°C/hour	$\langle 1\bar{3}^{\circ}$ $(\bar{1}, 1, \bar{1})$	34 35 36 37	3.3 5.0 5.0 7.5	He	---	---	Slider stuck with growth columns over substrates. Layers thick, but fairly smooth.
LPE-2	977	965	2°C/hour	$\langle 2^{\circ}$ $(\bar{1}, \bar{1}, \bar{1})$	38 39 40 41	0 0 0 0	He	---	---	Very good appearing layers; quite thin.
LPE-3	1019	986	2°C/hour	$\langle 2^{\circ}$ $(\bar{1}, \bar{1}, \bar{1})$	42 43	0 0	He	---	---	Wider temperature interval, layers correspondingly thicker.
LPE-4	--	--	2°C/hour	$\langle 2^{\circ}$ $(\bar{1}, \bar{1}, \bar{1})$	44 45 46 47	0 0 0 0	He	General Electric (GE)	(GE)	Vacuum leak; no growth.
LPE-5	930	913	2°C/hour	$\langle 2^{\circ}$ $(\bar{1}, \bar{1}, \bar{1})$	48 49	0 0	He	(GE)	(GE)	Layer somewhat off center of substrate; good appearance.
LPE-6	975	963	2°C/hour	$\langle 2^{\circ}$ $(\bar{1}, \bar{1}, \bar{1})$	50 51	0 0	He	(GE)	(GE)	Melt back; questionable film thickness.
LPE-7	974	963	2°C/hour	$\langle 2^{\circ}$ $(\bar{1}, \bar{1}, \bar{1})$	52 53	0 0	4%H_2 in He	(GE)	(GE)	Much cleaner growth charge after run; LPE layer thickness~12 μm.
LPE-8	975	951	2°C/hour	$\langle 2^{\circ}$ $(\bar{1}, \bar{1}, \bar{1})$	54 55	0 0	4%H_2 in He	(GE)	(GE)	Similar to run 7.
LPE-9	974	944	2°C/hour	$\langle 2^{\circ}$ $(\bar{1}, \bar{1}, \bar{1})$	56 57 58 59	3.0	10%H_2 in He	A. D. Little	A. D. Little	Surfaces similar to two previous runs; growth steps and irregularities, but specularly reflecting.

TABLE 4.
SUMMARY OF LPE GROWTH RUNS - SLIDER NO. 3

Run Number	Substrate GaP		Orientation Error	GaP Source	Temperature Cycle (°C)			Mole % Cu	Comments
	Number	Supplier	(111) (Deg.)		High	Start	Stop		
LPE-10	60	A.D. Little	1.5	Monsanto	964	964	20	0	First run with slider mechanism 3, substrates too thick; layers thin, but quite smooth.
	61	A.D. Little	1.5	Monsanto				3.0	
	62	A.D. Little	1.5	Monsanto				4.2	
	63	A.D. Little	1.5	Monsanto				5.8	
	64	A.D. Little	1.5	Monsanto				8.2	
	65	A.D. Little	1.5	IMANCO-2				0	
LPE-11	66	IMANCO-2	1.5	Monsanto	1049	1049	1044	0	Much improved layer smoothness over those with slider mechanism 2.
	67	A.D. Little	1.5	Monsanto				0	
	68	A.D. Little	1.5	Monsanto				4.0	
	69	IMANCO-2	1.5	Monsanto				6.0	
	70	A.D. Little	1.5	Monsanto				7.9	
LPE-12	71	A.D. Little	0.3	M.PPC*	See comments.			0	Lost temperature control; substrates dissolved.
	72	A.D. Little	0.3	M.PPC				4.1	
	73	A.D. Little	0.3	M.PPC				6.0	
	74	IMANCO-2	1.5	M.PPC				6.0	
	75	A.D. Little	0.3	M.PPC				8.0	
LPE-13	76	A.D. Little	0.4	M.PPC	1030	1030	1025	0	Generally good appearance. Thickness ranged from 0 to 30 μm.
	77	A.D. Little	0.6	M.PPC	Questionable temperature measurements; lost thermocouples.			4.2	
	78	A.D. Little	0.2	M.PPC				5.7	
	79	IMANCO-2	1.5	M.PPC				5.8	
	80	A.D. Little	0.6	M.PPC				8.2	
LPE-14	81	IMANCO-2	1.5	M.PPC	1040	1040	1040	0	Meltback experiment only. Constant temperature while growth charge on substrate. Meltback did occur.
	82	IMANCO-2	1.5	M.PPC					
LPE-15	83	IMANCO-2	0.6	M.PPC	1047	1042	1036	0	Note change in temperature cycle - temperature decreased 5% from "high" before moving growth charge onto substrate. Furnace profile found to be very poor. Average thickness = 8 to 30 μm.
	84	IMANCO-2	0.2	M.PPC				0	
	85	IMANCO-2	0.3	M.PPC				4.2	
	86	IMANCO-2	0.4	M.PPC				6.0	
	87	IMANCO-2	0.6	M.PPC				8.0	

* M.PPC = Monsanto polyporous chunk.

TABLE 4. (Continued)

Run Number	Substrate GaP Number	Substrate GaP Supplier	Orientation Error (111) (Deg.)	GaP Source	Temperature Cycle (°C) High	Start	Stop	Mole % Cu	Comments
LPE-16	88	IMANCO-2	—	None	1050	1045	1040	N/A	No growth for substrate 88. Cooling gas tube broke during run. Furnace temperature profile releveled. Ga well machined under slider. Average thickness = 8 to 18 μm.
	89	IMANCO-2	< 1.5	M.PPC				0	
	90	IMANCO-2	0.4	M.PPC				0	
	91	IMANCO-2	0.3	M.PPC				0	
	92	IMANCO-2	0.3	M.PPC				0	
LPE-17	93	IMANCO-2	0.3	M.PPC	1048	1043	1038	0	Average thickness = 5 to 15 μm.
	94	IMANCO-2	0.5	M.PPC				0	
LPE-18	95	IMANCO-2	0.6	M.PPC	1049	1044	1039	4.0	Slider baked out at 1050°C in H_2 before run. Average thickness = 8 to 14 μm.
	96	IMANCO-2	0.4	M.PPC				6.0	
LPE-19	97	IMANCO-2	< 0.5	M.PPC	1048	1042	1036	0	No substrate cooling. Slider baked out at 1050°C in H_2 before run. Average thickness = 8 to 17 μm.
	98	IMANCO-2	< 0.5	M.PPC				0	
	99	IMANCO-2	< 0.5	M.PPC				0	
LPE-20	100	IMANCO-3	~ 0.8	I.PDI**	1052	1046	1041	5.5	Slider baked out at 1050°C before run. No potassium ferricyanide substrate etch used. Average thickness = 20 to 30 μm.
	101	IMANCO-3		I.PDI				5.6	
	102	IMANCO-3		I.PDI				5.6	
	103	IMANCO-3		I.PDI				5.5	
	104	IMANCO-3	~ 0.8	I.PDI				5.5	
LPE-21	105	IMANCO-2		M.PPC	1056	1047	1043	6.0	Slider baked out at 1090°C in H_2 before run. Average thickness = 9 to 14 μm.
	106	IMANCO-2		M.PPC				6.0	
LPE-22	107	IMANCO-3		I.PDI	1048	1044	1039	0	Slider baked out at ~1050°C in H_2 before run. Leak found in flange - growth tube seal after run, p-type conductivity observed. Average thickness = 6 to 10 μm.
	108	IMANCO-3		M.PPC				0	
	109	IMANCO-2		M.PPC				0	
	110	IMANCO-3		I.PDI				0	
	111	IMANCO-3		M.PPC				0	
	112	IMANCO-2		M.PPC				0	
LPE-23	113	IMANCO-3	0.75	I.PDI + 8% sulfur doped GE (GE:S)	1047	1041	1038	0	New furnace tube with water-cooled flange. Average thickness = 2 to 6 μm.
	114	IMANCO-3	0.75					0	
	115	IMANCO-3	0.75					2.0	
	116	IMANCO-3	0.75					4.2	
	117	IMANCO-3	0.75					8.0	Excellent photoconductor.

** I.PDI = IMANCO polycrystalline ingot.

TABLE 4. (Concluded)

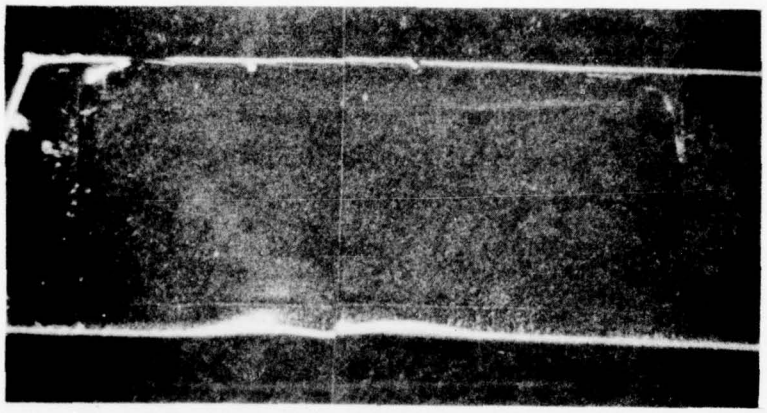
Run Number	Substrate GaP		Orientation Error	GaP Source	Temperature Cycle (°C)			Mole % Cu	Comments
	Number	Supplier	(lll) (Deg.)		High	Start	Stop		
LPE-24	118	IMANCO-3	0.75	LPDI + 4% GE:S	1048	1043	1039	0	Less GE:S used, resistivity up. Average thickness = 4 to 7 μm.
	119	IMANCO-3	0.75					2.0	
	120	IMANCO-3	0.75					3.5	
	121	IMANCO-3	0.75					5.2	
	122	IMANCO-3	0.75					5.2	
	123	IMANCO-3	0.75					8.0	
LPE-25	124	IMANCO-3	0.75	LPDI	1045	1042	1029	0	Cool down interval and cool down rate increased x3. Support tube broke - layers very thick (~100 μm).
	125	IMANCO-3	0.75					1	
	126	IMANCO-3	0.75					2	
	127	IMANCO-3	0.75					0	
	128	IMANCO-3	0.75					3.5	
	129	IMANCO-3	0.75					5.2	
LPE-26	130	IMANCO-4	0.6	LPDI + 9% GE:S	1049	1044	1029	0	New quartz support tube seal failure, layers very thick (~100 μm).
	131	IMANCO-4	0.6					0	
	132	IMANCO-4	0.6					2.0	
	133	IMANCO-4	0.6					3.5	
	134	IMANCO-4	0.6					5.2	
	135	IMANCO-4	0.6					8.0	
LPE-27	136	IMANCO-4	0.6	LPDI + 5% GE:S	1049	1045	1031	3.4	Precursor technique, poor surfaces.
	137	IMANCO-4	0.6					5.2	
	138	IMANCO-4	0.6					8.0	
LPE-28	139	IMANCO-4	0.6	LPDI + 5% GE:S	1050	1045	1035	3.5	Precursor technique, poor surfaces.
	140	IMANCO-4	0.6					8.0	
	141	IMANCO-4	0.6					5.2	
LPE-29	142	IMANCO-2	0.6	LPDI + 5% GE:S	1045	1040	1027	3.4	Precursor technique, poor surfaces not due to substrates.
	143	IMANCO-4	0.6					5.2	
	144	IMANCO-2	0.6					8.0	

cooling system was not operative during this run. The grown layers were found to be too thick to move the slider after the designed growth temperature cool-down. Hence, the substrates remained under the growth columns during the entire cool-down which resulted in very thick layers (~100 μm).

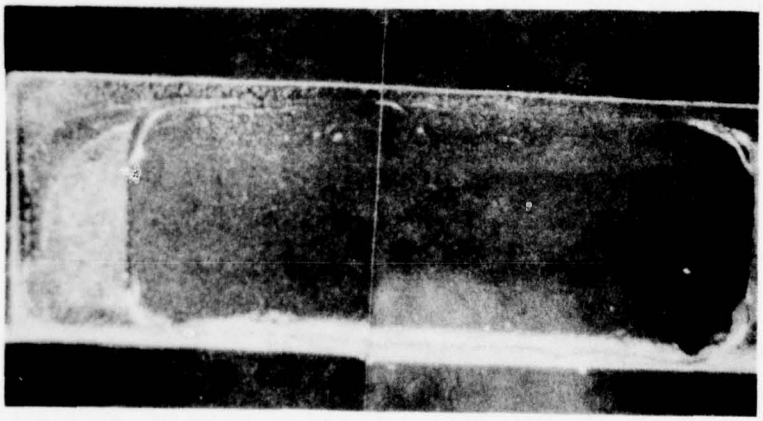
For run LPE-11, the substrates were lapped to give approximately 0.002 in. clearance after growth. The slider moved with ease and wiped all of the Ga from three of the five grown layers and approximately 90% of the Ga from the remaining two layers. This growth run used the slider base cooling, with the flow rate such that the temperature drop in the base cooling hole was 0.8°C. The growth temperature interval was moved to a substantially higher temperature (1049°C) for this run (see Table 4). This temperature increase was based on increasing evidence, from both the BSG and LPE growth experiments, that close compensation of GaP is not achieved for temperatures less than 1000°C. In these experiments, 4-8 mole % of Cu was added to the growth charge. Photographs of two of the five layers are shown in Figure 14.

Loss of temperature control resulted in dissolving the substrates during LPE-12; hence, no growth was achieved. LPE-13 was similar to LPE-12, but the temperature cycle went as planned, and the layers came out with a cleaner Ga wipe-off than any previous run. The layers appeared very smooth to the eye, as shown in Figure 15, and surface topography measurements confirmed surface roughness to be less than 0.2 μm over large (~0.5 cm) distances. However, variations in layer thickness were found to be as much as 20 μm over distances of a few mm. These measurements also gave evidence of substrate meltback even though a surplus of GaP starting material had been used. This run did provide Cu-doped layers which were used in photoconductor evaluation and are described later in this section.

Because of the meltback evidence that was seen in LPE-13, LPE-14 was designed to determine whether meltback was occurring due to subsaturation of the melt at the initiation of the growth. The growth cycle was performed as usual, except the cool-down was eliminated while the growth column was over the substrate. The growth column was left over the substrate for only 11 minutes. Meltback of the substrate was clearly observed. To solve this problem, a pre-growth cool-down of



a



b

Figure 14. LPE layers from (a) LPE 11-68 and (b) LPE 11-70.

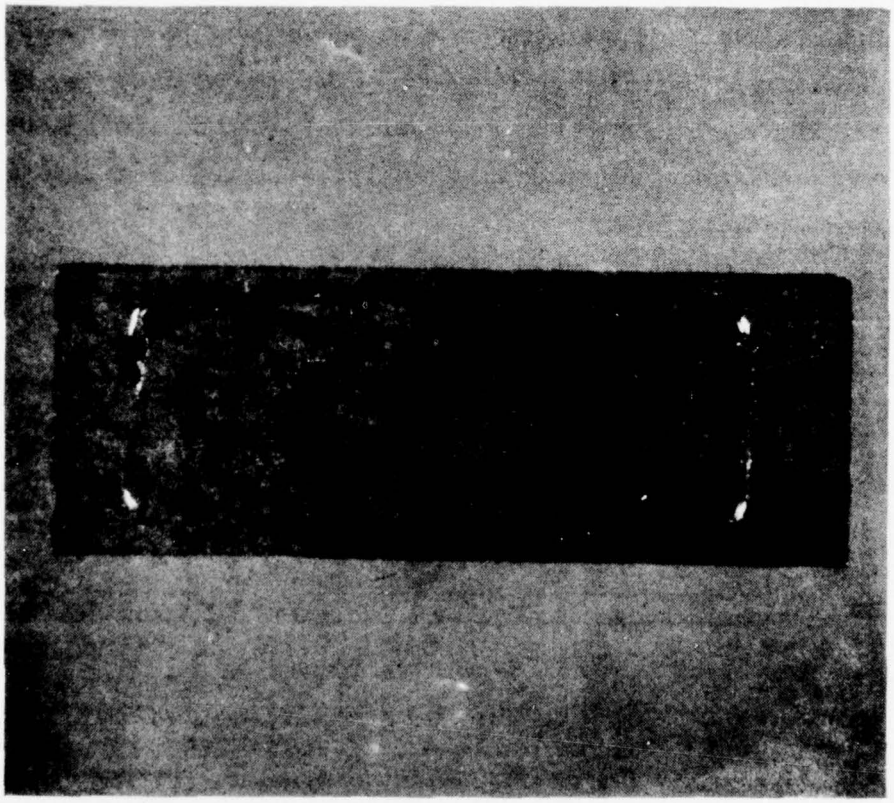


Figure 15. Grown layer from LPE-13-76.

5°C was added to the growth cycle following the usual 4-hour soak at the highest temperature of the cycle. Note in Table 4 that beginning with LPE-15, all growth runs used this pre-growth cool-down.

LPE-15 demonstrated the success of this modification; no evidence of meltback was observed. However, the variation of surface height along the length of the LPE layer remained. Since the length (0.75 in.) of the substrate is perpendicular to the length of the cooling gas hole (diameter = 0.375 in.), uneven cooling across the growth interface was suspected. To reduce temperature variations over the areas of the substrate, a cavity was machined in the top surface of the slider base as shown in Figure 16. This cavity is filled with liquid Ga when the slider is assembled. Because Ga has a higher thermal conductivity than graphite and the ability to mix by convection, a temperature leveling contact is made to the bottom of the substrate slider. This maintained the substrate at a more uniform temperature than before.

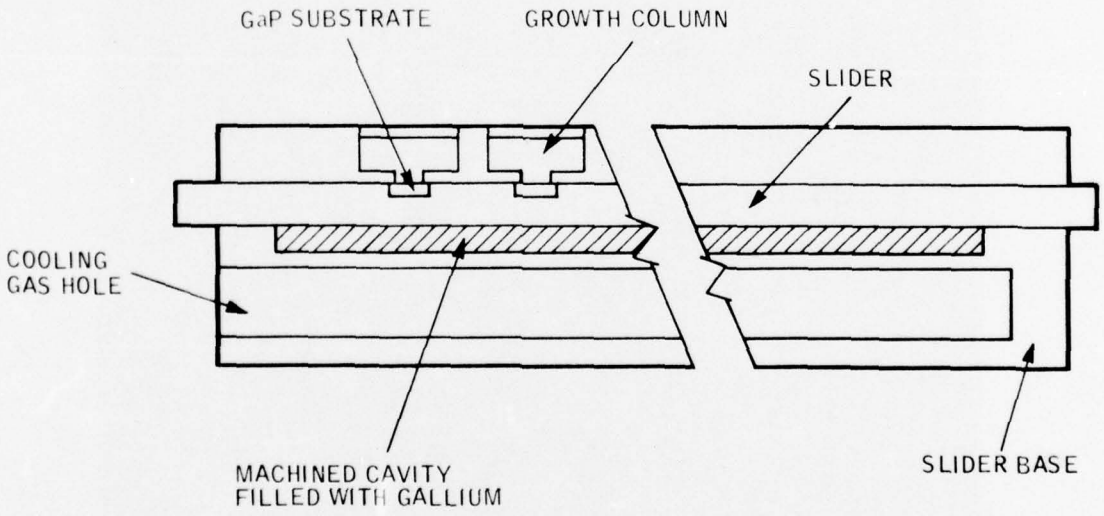


Figure 16. Cross-section of modified LPE slider mechanism 3.

LPE-16 (three substrates, all undoped growth charges) incorporated these modifications. LPE-16 layers were much flatter over larger distances than layers from any previous run. Both smoothness and flatness appear to be acceptable.

No growth charge was used in the bin for substrate 88. The purpose was to reveal the amount of substrate surface deterioration which occurs in the environment of the LPE system. A fair amount of surface pitting was seen such as might occur if traces of water vapor were present. Later evidence of persistent p-type conductivity (LPE-19, LPE-21 and LPE-22), which could result from interaction of oxygen or water vapor with the graphite slider to incorporate carbon into the growth charge, resulted in several growth process modifications. These modifications, included storage of the slider in a dry atmosphere between runs, minimum exposure of the slider to the atmosphere and pre-growth bake-out of the slider at $50^{o}C$ above the growth temperature.

LPE-17 was an undoped run using just two substrates. It used a low-temperature slider bake-out for the first time. C-V measurements showed the layers to be n-type at $2x10^{17}cm^{-3}$. A large featureless area of the surface of LPE-17-93 as seen with Nomarski interference microscopy is shown in Figure 17. Note the higher concentration of growth steps in the vicinity of a surface defect.

LPE-18 was very similar to LPE-17 except that both layers were Cu doped. These layers showed very high photoconductive gain.

LPE-19 was also similar to LPE-17. However, the substrate cooling did not function properly. All the layers were p-type. A possible cause of the p-type doping will be discussed in the description of LPE-21 and LPE-22.

LPE-20 used new substrate and source material. An undoped Czochralski ingot from IMANCO (number 3) provided the substrates and polycrystalline dense ingot GaP, also from IMANCO, was used for source material. All of these Cu-doped layers turned out n-type. However, Hall analysis of the substrate wafers showed them to be quite nonuniform, including many regions of p-type conductivity. Problems were also experienced in the use of the usual potassium ferricyanide etch, and a bromine etch was used instead. Most of the material was returned to the supplier for replacement.

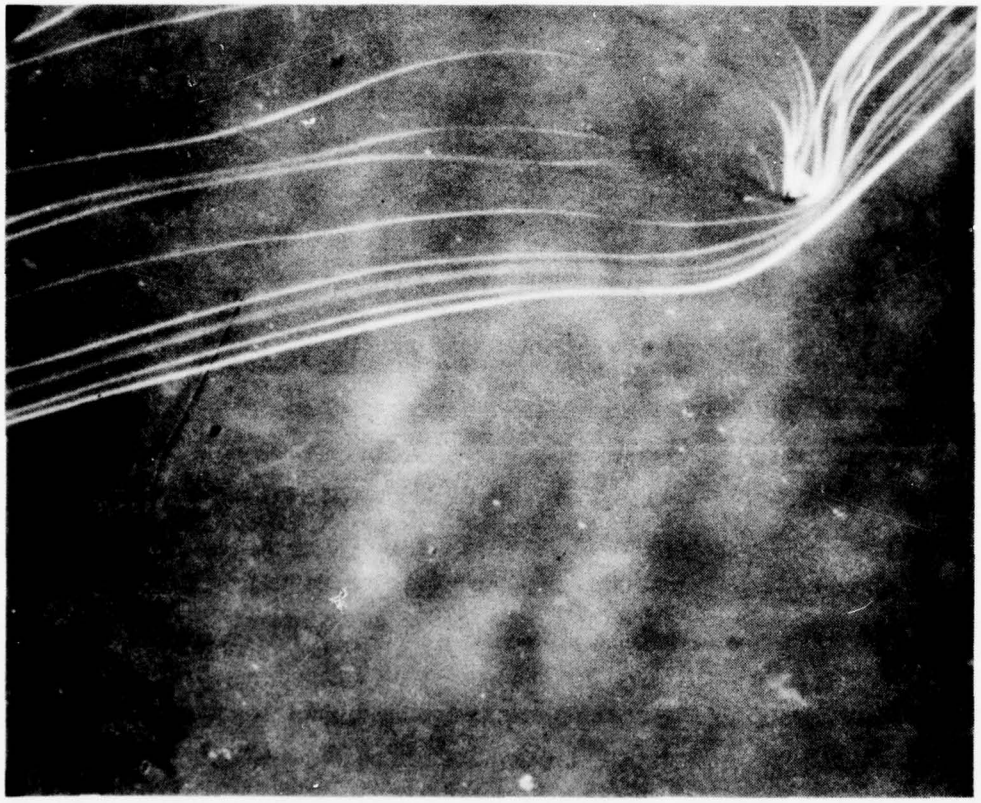


Figure 17. Surface topography of LPE-17-93.

LPE-21 returned to the use of a Czochralski GaP substrate material which was previously purchased from IMANCO and labeled number 2. LPE-22 used both IMANCO-2 and IMANCO-3 for substrates. The two layers of LPE-21 were Cu doped; the six layers of LPE-22 were all undoped. Both runs yielded all p-type layers, which reduced suspicion of the source and substrate materials as the cause of the increasing number of layers exhibiting p-type behavior since LPE-19. After LPE-22, a leak in the growth apparatus was discovered between the alumina furnace tube and the stainless steel end flange. This seal was made with room-temperature-curing Si rubber. The seal failed partly because of excess temperature of the flange and partly due to a poor bond to the stainless steel. Decomposing Si rubber will evolve methyl groups and could be at least partly responsible for the carbon doping and consequent p-type conductivity seen in later LPE runs. The other aspect of the seal failure that could have contributed to carbon doping involves the interaction of water vapor with the graphite slider that was previously discussed.

After LPE-22, the flange was redesigned with water cooling to keep its temperature less than 50^{o}C.

LPE-23 was a five-substrate growth run with two layers undoped and three layers doped by adding 2,4 and 8 mole % Cu to the respective growth charges. In addition, $\sim$30 mgm of Czochralski GaP sulfur-doped to $\sim 1 \times 10^{-18} cm^{-3}$ n-type was added to the growth charge. The purpose of adding the S-doped GaP charge material was to attempt to control the n-type doping of the LPE in order to obtain more consistent results from the Cu counter doping.

All five layers turned out n-type and the Cu-doped layers exhibited excellent photoproperties which are discussed in detail later in this section.

LPE-24 was essentially a repeat of LPE-23 with less S-doped GaP charge material added. The purpose was to achieve higher resistivity than measured on LPE-23 layers. LPE-24 was also the first run to use several modifications in the growth procedure designed to improve purity including a double 1100^{o}C slider bake-out in H_2, storage of the slider in a H_2 atmosphere between runs and a reduced time of exposure to the atmosphere during loading (13 min. in this case). These layers had excellent growth morphology. Surface topography measurements showed variations in surface height as little as 1 μm over a distance of 1.2 cm. as shown in Figure 18 for LPE 24-118, the reduc-

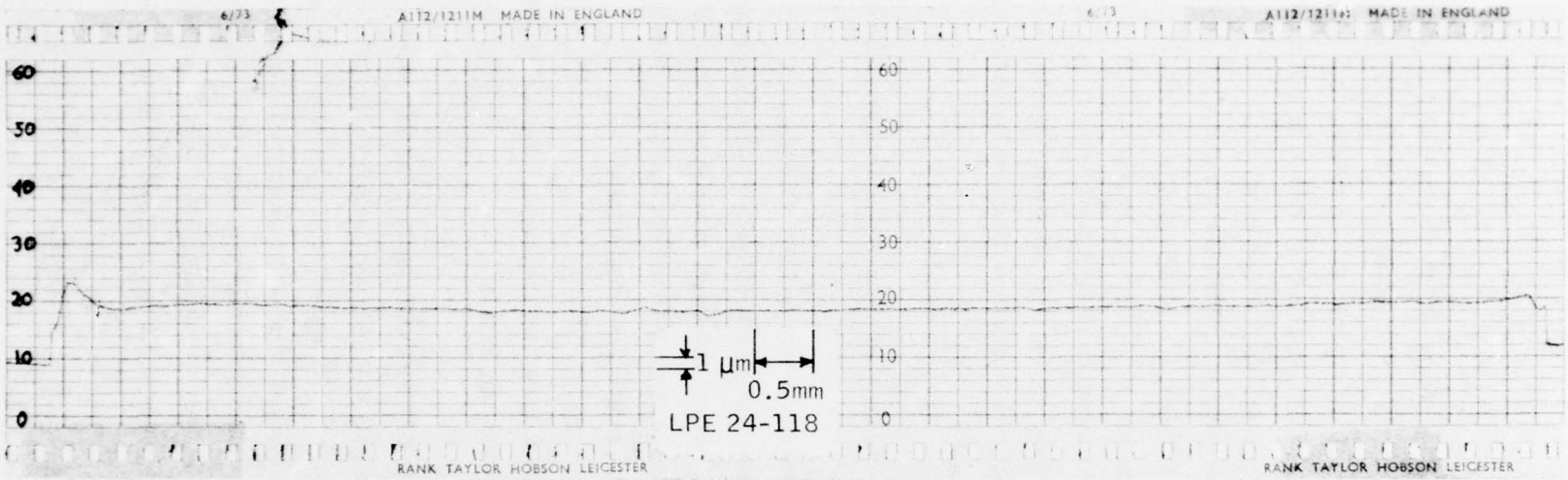


Figure 18. Surface topography of LPE 24-118.

tion in the amount of S-doped GaP charge material resulted in the planned increase in resistivity. It was up about a factor of 10^3 over the resistivity of LPE-23.

The photoconductive gain was lower in the layers from LPE-24 than in similarly doped layers from LPE-23, indicating that less Cu becomes electrically active when the donor density is reduced. This suggests that the amount of Cu which is incorporated in the GaP depends on other impurities which are present in the melt.

LPE-25 was also six layers; two were undoped and four were grown from charges containing 2.0 to 8.0 mole % Cu, respectively. No sulfur dopant was added to the charge in order to better assess the reduction in the carbon contamination problem resulting from the new end flange seal that was installed prior to LPE-23.

The growth cycle for LPE-25 was modified to extend the growth temperature interval from 5 to 15°C in order to produce a layer three times as thick as previous runs. The cool-down rate was also increased from 2.5°C/hr to 6.7°C/hr so that growth time would be only slightly increased. During the run, the slider support tube broke, making it impossible to slide the growth columns off the substrates. Growth therefore continued during the entire furnace cool-down. As a result, the layers were 125 μm thick, making it very difficult to remove the substrate holder from the slider. Their appearance is surprisingly good, but they do have much deeper growth steps than in the thinner layers which we usually grow. The layers showed n-type conductivity (as did all layers LPE-23 through LPE-29), demonstrating that the new end flange seal eliminated a major source of carbon contamination.

Another support tube failure during LPE-26 again prevented termination of growth and resulted in very thick layers since growth continued through the entire cool-down.

Runs LPE-27 through LPE-29 explored a variation of our LPE technique which uses a precursor substrate to complete saturation of the growth charge. In this variation, a growth charge is placed in every other bin, and substrate slots hold alterately a growth substrate and a precursor substrate. In this technique, the melt is initially slightly undersaturated. After the apparatus is brought up to

temperature, the melt is moved over a GaP precursor substrate which partially dissolves and saturates the melt. The melt is then brought over the LPE substrate for growth. The use of a precursor is intended to insure that equilibrium conditions exist at the growth interface and hence yield better growth morphology and thickness control. In this run, substrate cooling was eliminated. The LPE-27 layers exhibited a very poor surface morphology.

LPE-28 was a duplicate of LPE-27. A careful examination of the substrates after the final potassium ferricyanide free etch revealed a pattern of grooves similar to that seen in the grown layers of LPE-27, although on a much smaller scale of depth and width. The substrates were then repolished with bromine methanol, which removed nearly all of surface features which appeared after the potassium ferricyanide etch. The layers grown in LPE-28 were very similar to those of LPE-27; a high density of grooves 2 to 20 μm deep with some extending all the way to the substrate. Since the growth cycle is significantly different, it cannot be ruled out as the cause of the degraded surfaces, but also suspect is the substrate material which is from a new IMANCO boule for runs LPE-27 and LPE-28. Subsequent etching experiments on samples of previously used IMANCO boule 2 and on the new IMANCO boule 4 GaP conclusively establish that boule 4 becomes very rough and grooved while boule 2 gets smoother in the same potassium ferricyanide etch.

Another possible explanation of the poor surface morphology in spite of the modifications which should have improved the growth is the absence of the substrate cooling. Substrate cooling, which produces a temperature difference across the growth interface, may be of crucial importance in obtaining smooth LPE layers in our apparatus.

LPE-29 also used the precursor technique. Both IMANCO-2 and IMANCO-4 substrates were used in order to test one of the explanations of the poor LPE surface morphology suggested above. Although the surfaces on the IMANCO-2 substrates were slightly better than those in LPE-27 or LPE-28, the explanation seems to be other than in the properties of the substrate. We believe the substrate cooling is the most likely factor and should be restored in all future LPE growth runs either with or without the precursor technique.

C. MATERIAL EVALUATION

This subsection summarizes the results of our material evaluation experiments. The objectives of the material evaluation program are twofold—(1) to characterize the material parameters which are important to the photodetection properties of the material and where possible correlate these with the growth parameters, and (2) to gain an improved understanding of the basic mechanisms which determine the photoconductive and transport properties of GaP.

The material presented is discussed under the following subheadings:

- Photoconductivity
- Transport measurements
- Infrared absorption
- Capacitance spectroscopy

In previous publications[1, 3], we have discussed these techniques and their application to the study of GaP. In the following paragraphs, we present the principal results obtained during the present program. A discussion of these results is given in the next section.

1. Photoconductivity

The principal objective of this program was to define a growth technique which could be used to grow large-area photosensitive crystals of GaP. Earlier Honeywell work[3, 4] had demonstrated that GaP:Cu, grown by the so-called random nucleation solution growth technique, had very

---

[1] AFML-TR-76-79 Report, "Advanced Development on GaP Materials for Satellite Attitude Sensors," Contract F33615-75-C-5244.

[3] R. G. Schulze and P. E. Petersen, J. Appl. Phys. 45, 5307 (1974).

[4] P. E. Petersen and R. G. Schulze, United States Patent No. 3,976,872, Gallium Phosphide Photodetector Having an As-Grown Surface and Producing an Output from Radiation having Energies of 2.2 to 3.8 eV.

desirable photoproperties. This technique was very useful for establishing technical feasibility. It was not, however, capable of providing the large single-crystal as-grown surfaces which are desired for device fabrication.

This part of the investigation was intended to study the photoproperties of GaP:Cu grown by liquid phase epitaxy (LPE) in order to determine the potential of LPE for the growth of sensitized GaP material.

Our past experience with bulk solution growth has shown that as-grown GaP surfaces have a significantly lower surface recombination velocity than do lapped and polished surfaces. Consequently, we are most interested in the photoproperties of as-grown LPE surfaces. Therefore, the LPE samples for photoconductivity studies are not mechanically or chemically polished in any way. The only preparation prior to contacting is an organic solvent rinse followed by a series of deionized water rinses. The ohmic contact on n-type samples is made by evaporating 750 Å of Ag:1% Te followed by 550 Å of Ni and heat treating at 680°C for 10 minutes. The dark and photo I-V characteristics were linear for fields up to 10^4V/cm for the samples used in the photomeasurements. This indicates that the current transport in these samples is not limited by minority carrier sweep-out, space charge limited currents or contact effects.

The sharp distinction in the shape of the spectral response curve for an as-grown and "treated" GaP surface is shown in Figure 19. Sample LPE-20-100 has an as-grown untreated surface and exhibits a very broad spectral response curve. LPE-18-95 had been etched in HCl acid to dissolve some free Ga droplets which were left on the surface after growth. HCl is not an etchant for GaP; nevertheless, it clearly destroys the photoresponse for photon energies $>$ 2.8 eV. In solution-grown GaP:Cu samples, we have measured the spectral response on an as-grown surface, and then polished the surface and remeasured the spectral response. The results for the as-grown and treated surface were similar to those shown in Figure 19.

Three important characteristics for a photoconductor are (1) dependence of the photoconductive gain on the photon energy, (2) dependence of the photoconductive gain on the photon flux intensity,

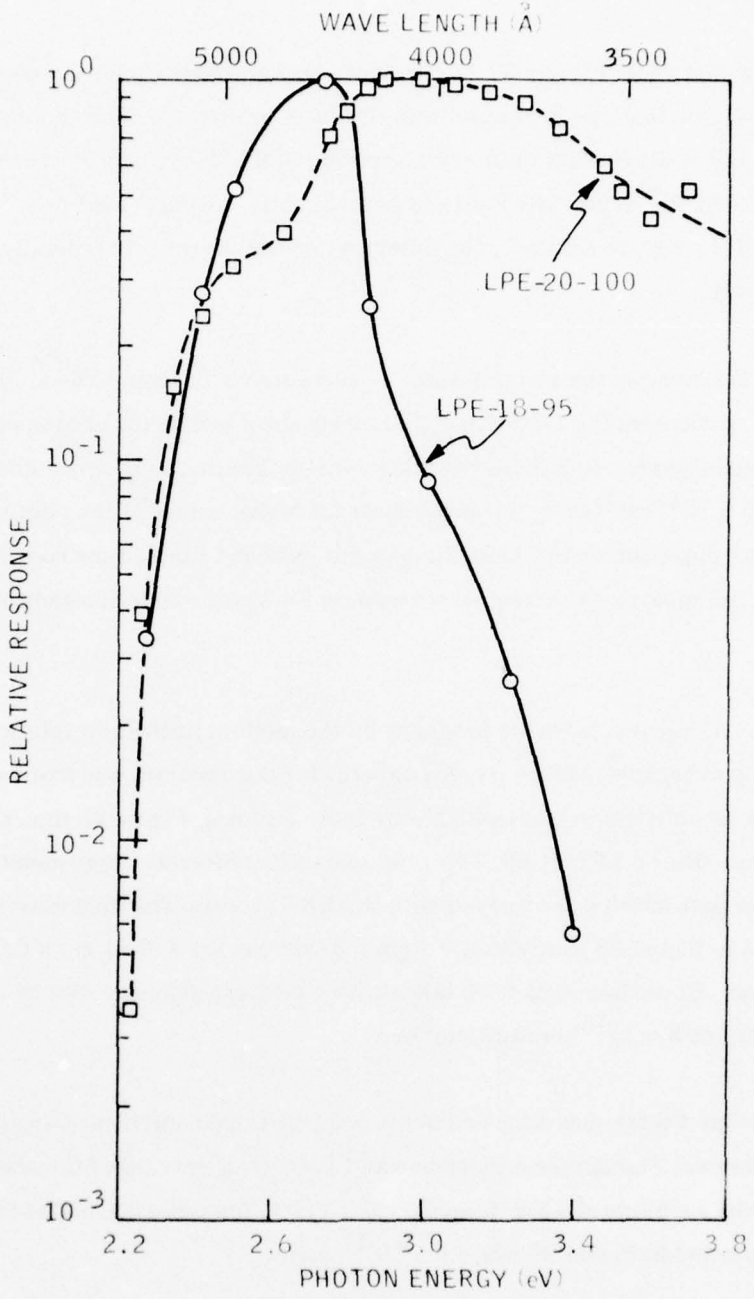


Figure 19. Spectral response for two LPE GaP:Cu samples. LPE-20-100 has an as-grown surface; LPE-18-95 has had an HCl etch.

and (3) the response time. Figures 20 - 22 show these characteristics for sample LPE-11-69, which is a Cu-doped sample that was grown midway through the program. The contacts for this sample were in the so-called slit configuration with a spacing of 0.002 cm. The electric field impressed on the sample was $\sim 2 \times 10^3$ V/cm. The field and consequently the gain could be increased by about a factor of 10. However, to eliminate the potential for breakdown, we generally keep the fields in the mid 10^3 range.

Note that, for this sample, the spectral response curve shown in Figure 20 exhibits a soft edge around 2.2 eV, peaks near 2.7 eV and has a relatively slow decline for photon energies above 2.8 eV. The photogain/photon flux intensity characteristic (Figure 21) is nearly linear for a photon flux less than $5 \times 10^{13} \text{cm}^{-2}\text{sec}^{-1}$, but is sublinear for higher values of the photon flux. The frequency response curve shown in Figure 22 does not exhibit a simple time constant characteristic. For the sake of comparison, the frequency response for a single time constant of 4×10^{-4} sec is shown.

Samples which were grown in earlier programs by the random nucleation solution (RNS) growth process lacked good spatial uniformity. An impetus for this program was that we believed the LPE growth process would yield crystals which were more uniform. Figure 23 shows the spatial uniformity for three slits on LPE-11-69. This represents a considerable improvement in the spatial uniformity over that which was observed with the RNS process. The dimensions of the active area for the samples in Figure 23 were slit 1, 0.2 cm x 0.002 cm; slit 2, 0.21 cm x 0.007 cm; and slit 3, 0.08 x 0.002 cm. All of these data were taken with a 0.01-cm-diameter spot of 2.7 eV radiation with an intensity of 5×10^{15} photons/cm^2-sec.

While the LPE GaP:Cu samples discussed above were Cu doped and hence sensitized, they were not closely compensated. The sample resistance was $< 1000\ \Omega$. Hence, all of the above measurements were taken in the a-c mode at a low frequency ($\sim$15 Hz). The noise current of the sample for which data is plotted in Figure 20 was 4.5×10^{-11} amps.

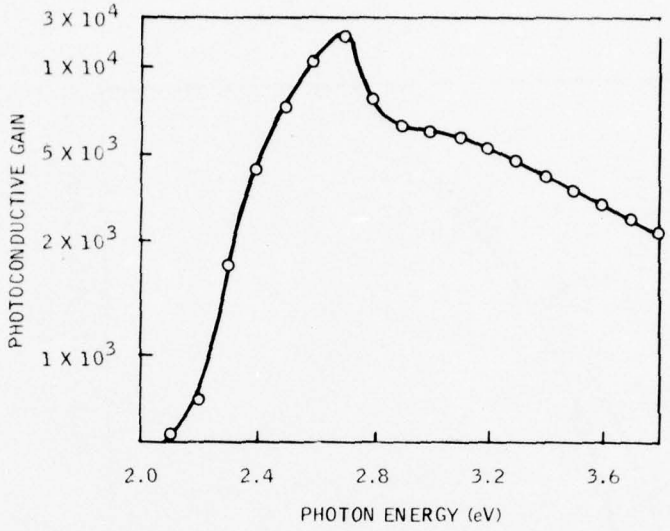


Figure 20. Photoconductive gain vs. photon energy for LPE-11-69 GaP:Cu photoconductor.

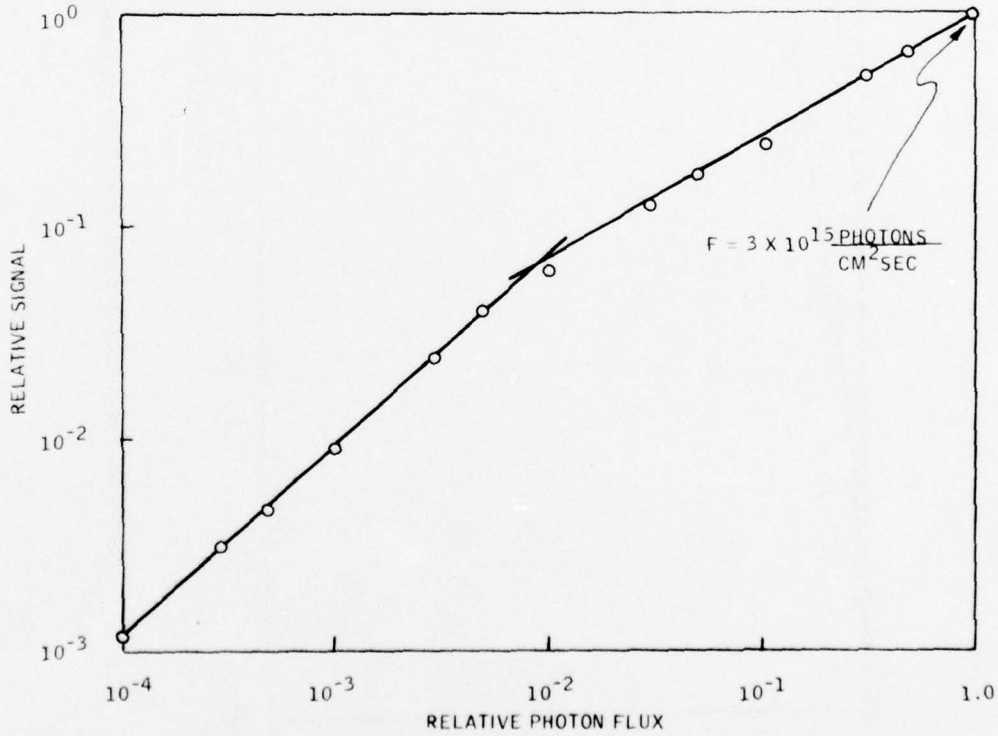


Figure 21. Photosignal vs photon flux intensity at 2.7 eV for LPE-11-69 GaP:Cu photoconductor.

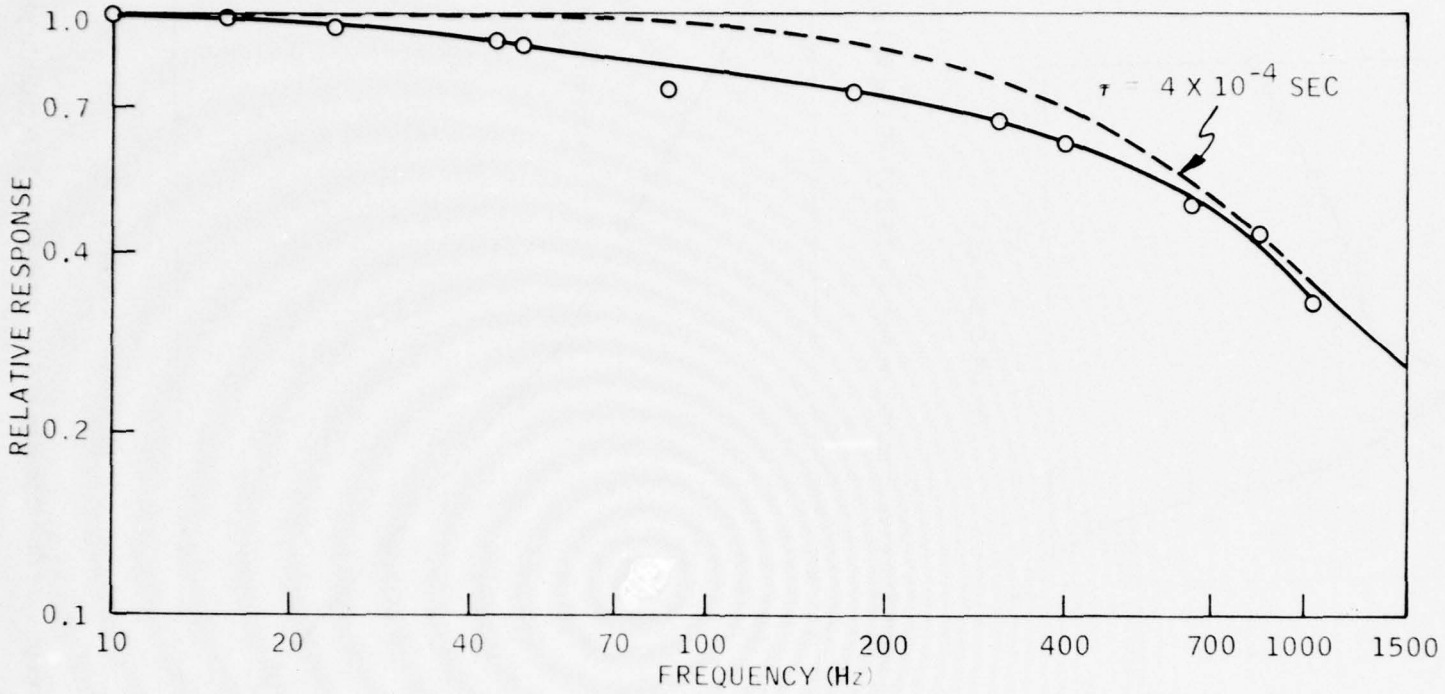


Figure 22. Frequency dependence of the photosignal of LPE-11-69 GaP:Cu.

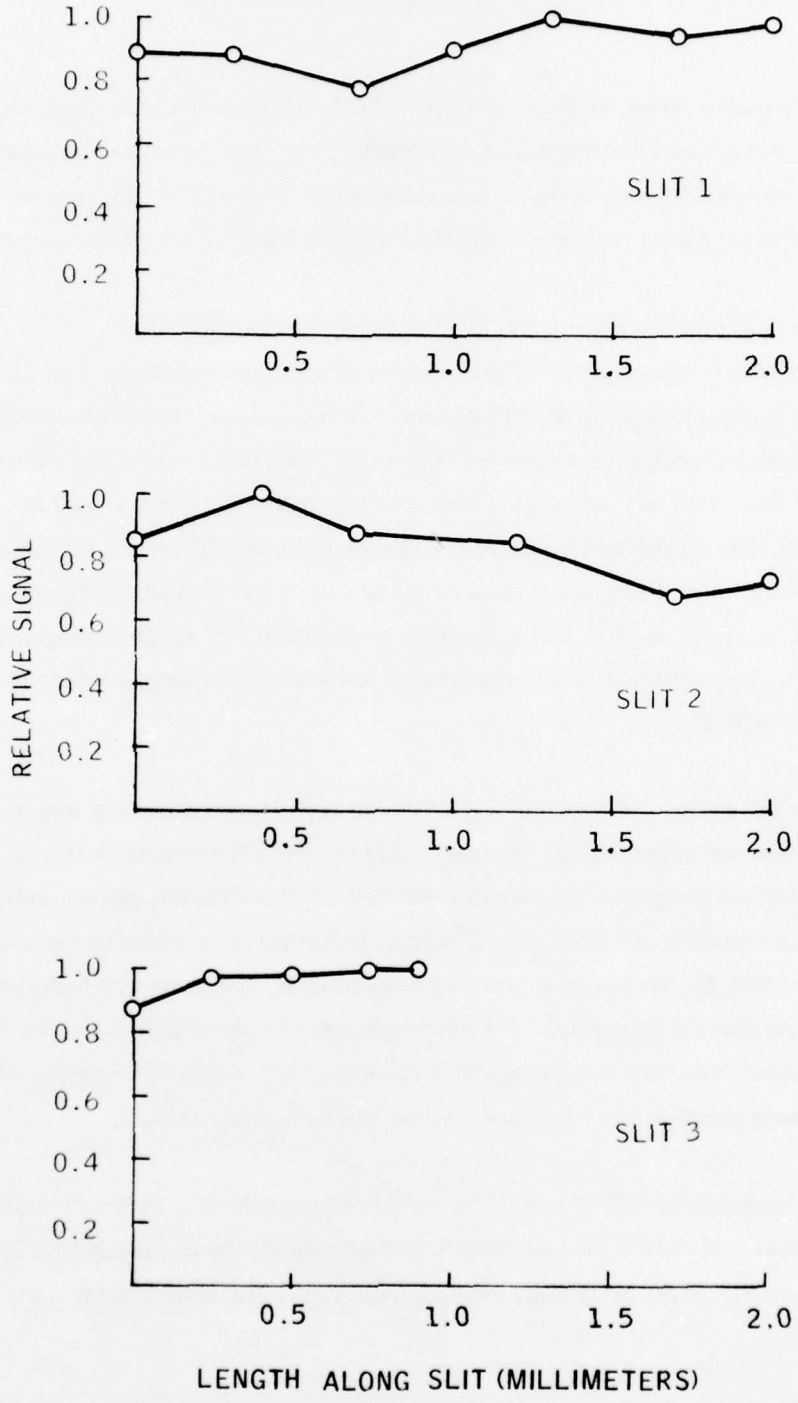


Figure 23. Spatial uniformity of the photosignal for three slits on LPE-11-69 GaP:Cu.

Figures 24 - 27 are a set of characteristic curves for LPE-23-117. As discussed in Section III B, the layers from LPE-23 exhibited a very good surface morphology. The layers were contacted in the slit configuration with a slit width of 0.002 cm. The electric field used in the measurement was $\sim 2 \times 10^3$ V/cm. This set of data represents the state of the art in GaP:Cu photoconductors.

Note that the spectral response (Figure 24) for this sample extends to 5.0 eV, with a photoconductive gain at 5.0 eV greater than 4×10^3. These samples have greater sensitivity into the near UV than samples from previous growth runs. This sample also exhibits a linear to sublinear transition in the photogain/photon flux intensity characteristic (Figure 25). The breakpoint occurs near 5×10^{11} photons/cm^2-sec. The frequency response is shown in Figure 26. Note that at 100 Hz, the signal is down by only 30%. The spatial uniformity of the photoconductors fabricated on this layer was acceptable, as evidenced by the data in Figure 27. These data were obtained from slits about 3-mm long and, over this distance, most of the data points were within 10% of the average. Although the sensitivity of these photoconductors was high, they were not neavily compensated. The resistance of the samples was $\sim 100\ \Omega$.

In the last growth run during this program (LPE-29), we experienced difficulty with the growth morphology, as discussed in Section III. We were unable to put slit contacts on the material, so we ohmically contacted the sample by alloying in small dots of In:1%Te. The photoconductive gain as shown in Figure 28 was $\sim 2 \times 10^5$ at $\sim 1.5 \times 10^3$V/cm. This is the most sensitive photoconductor we have fabricated thus far. However, as will be discussed later, sensitivity this high degrades the response time. Note that for this sample, the photosignal also remains high out to 5 eV. Figure 29 shows that the photoconductive gain/photon flux characteristic retains the same linear/sublinear shape of the previous samples. The break occurs near 10^{12} photons/cm^2-sec.

Sensitized photoconductivity will be thermally quenched at sufficiently high temperatures. We measured the photosignal in LPE-29-142 at 90°C and compared it with the signal at 20°C. The results are shown in Figure 30. Note that the signal does not degrade, but that there is a substantial increase in the noise.

It is also possible to optically quench sensitized photoconductivity by illumination with radiation whose energy is sufficient to excite holes out of the sensitizing centers. Figure 31 shows the result

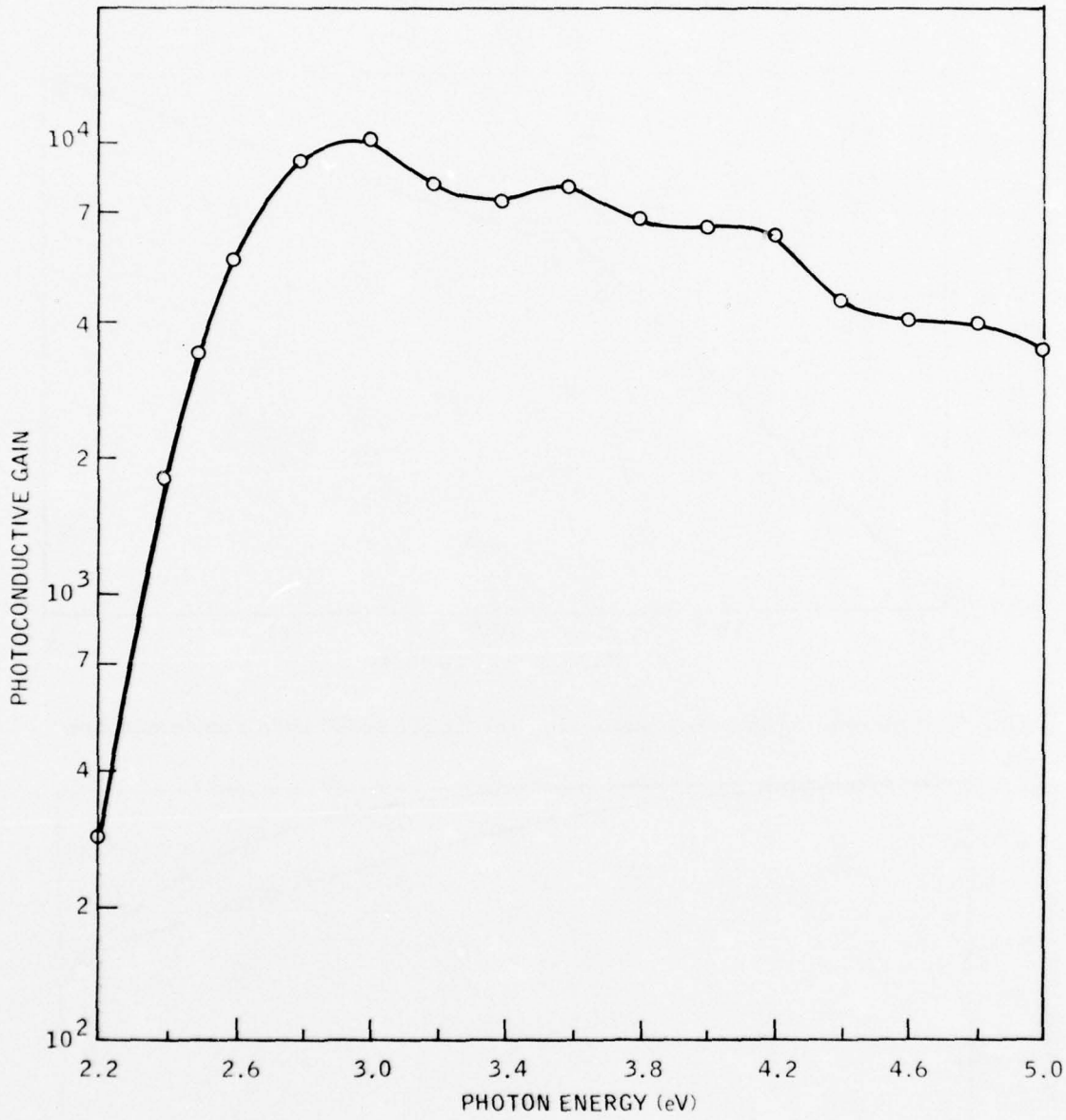


Figure 24. Photoconductive gain vs photon energy for LPE-23-117 GaP:Cu photoconductor.

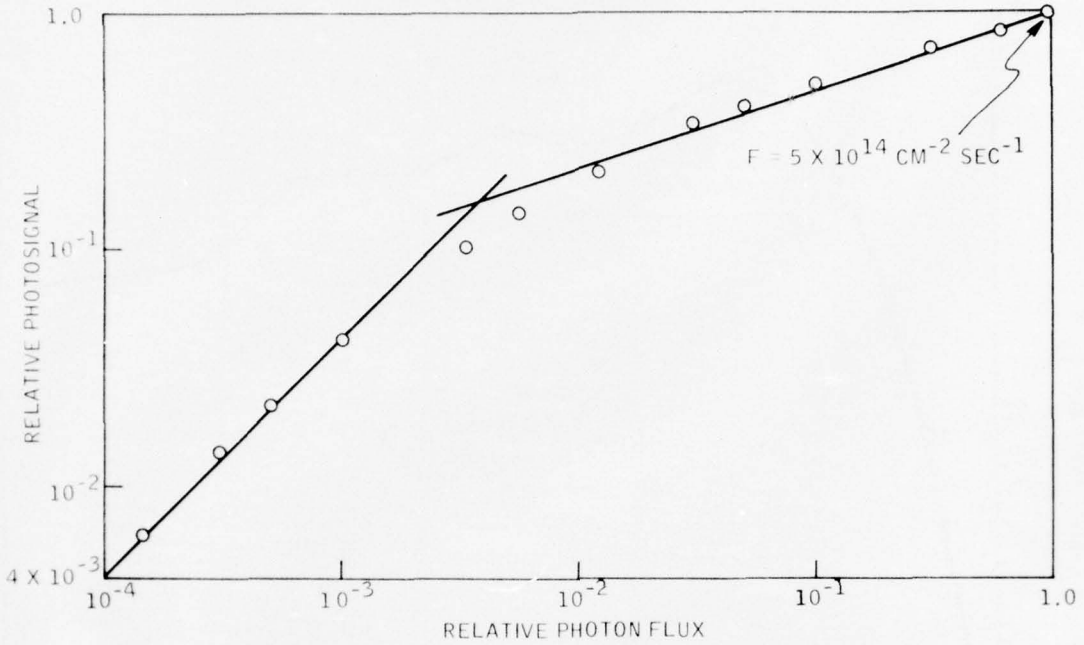


Figure 25. Photosignal vs photon flux intensity at 3.0 eV for LPE-23-117 GaP:Cu photoconductor.

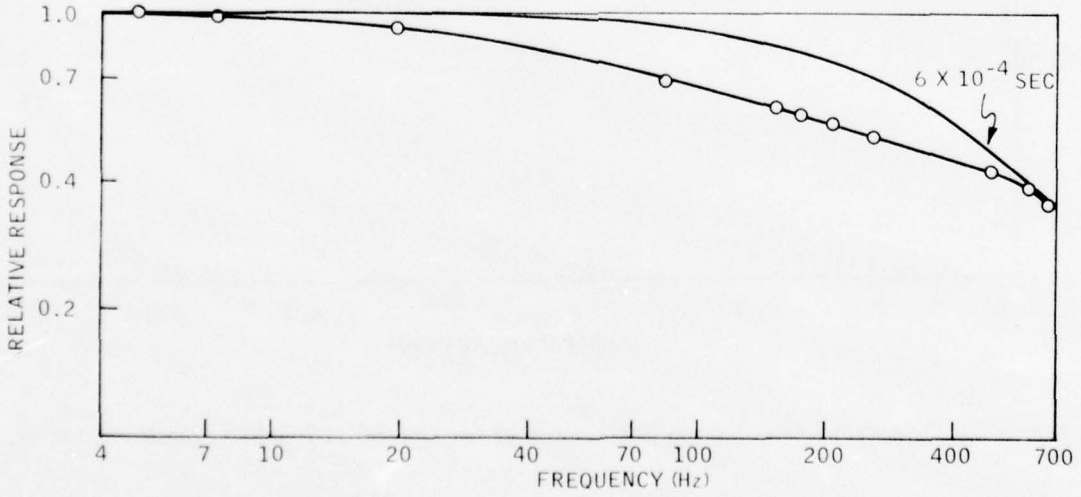
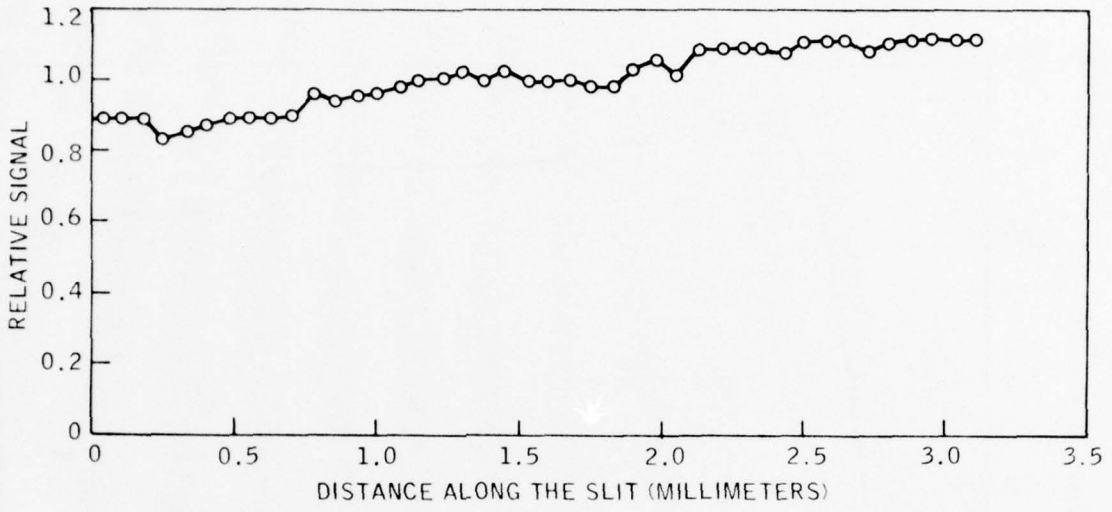


Figure 26. Frequency dependence of the photosignal of LPE-23-117 GaP:Cu.



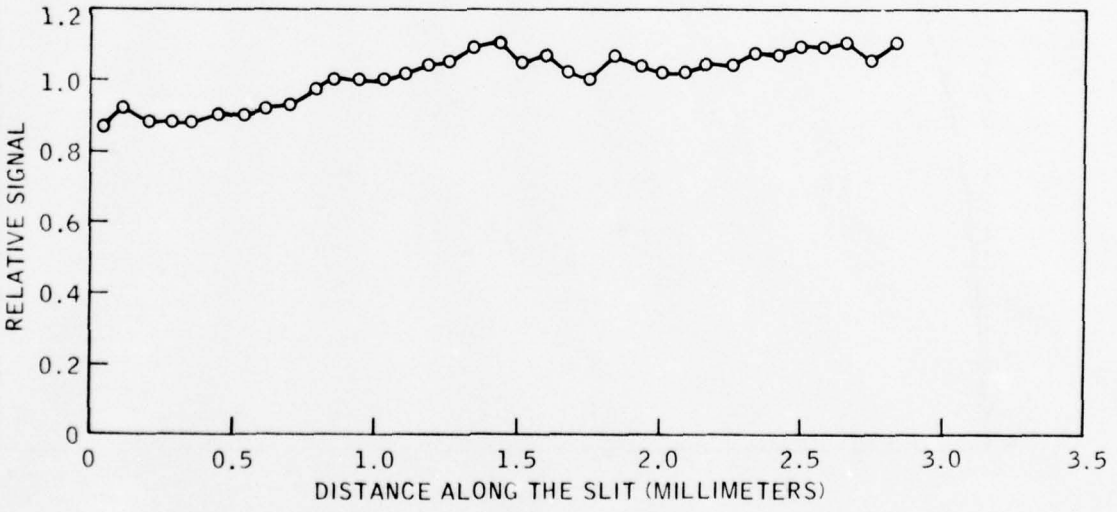


Figure 27. Spatial uniformity of the photosignal for two slits on LPE-23-117 GaP:Cu.

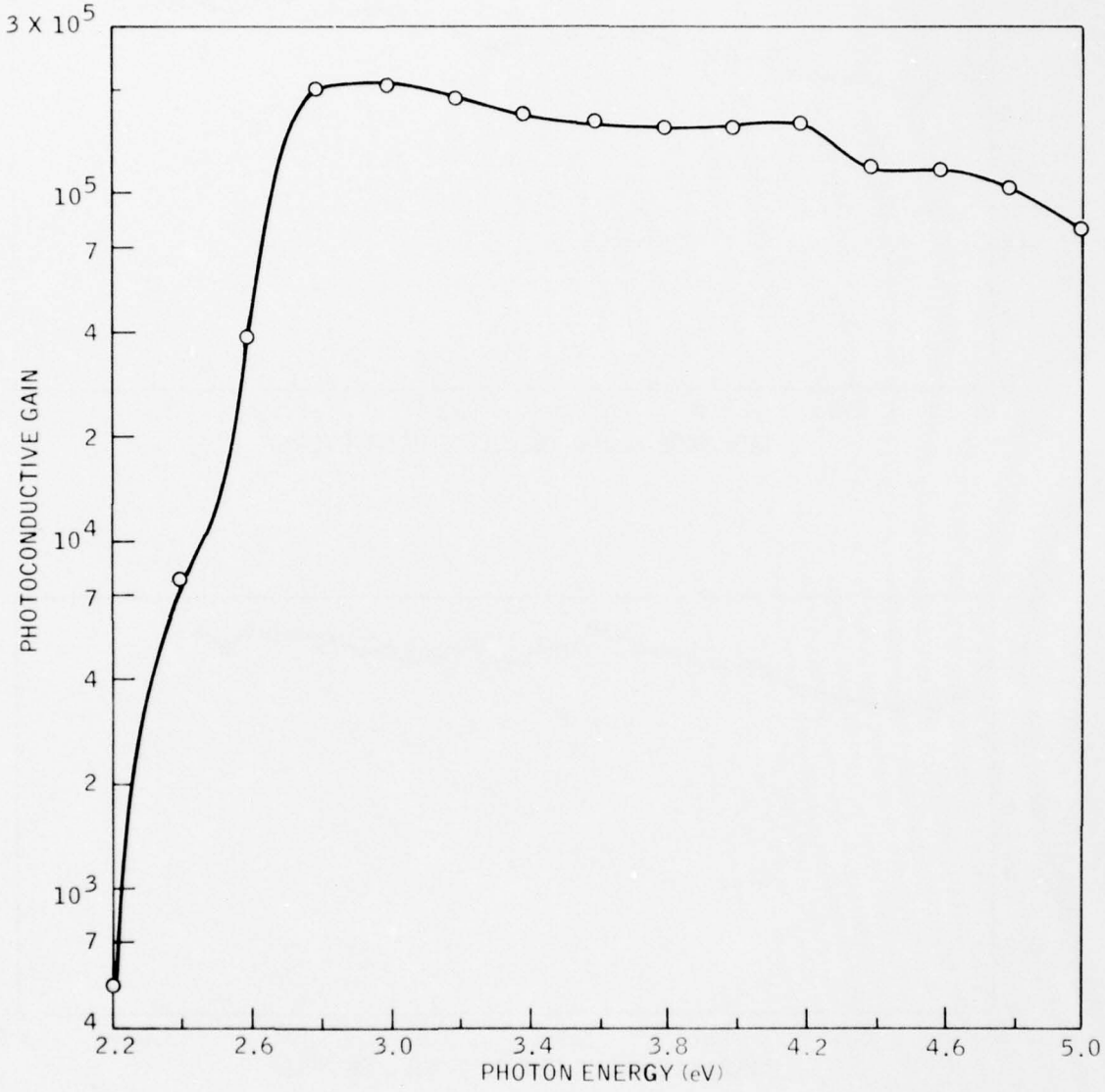


Figure 28. Photoconductive gain vs photon energy for LPE-29-142 GaP:Cu photoconductor.

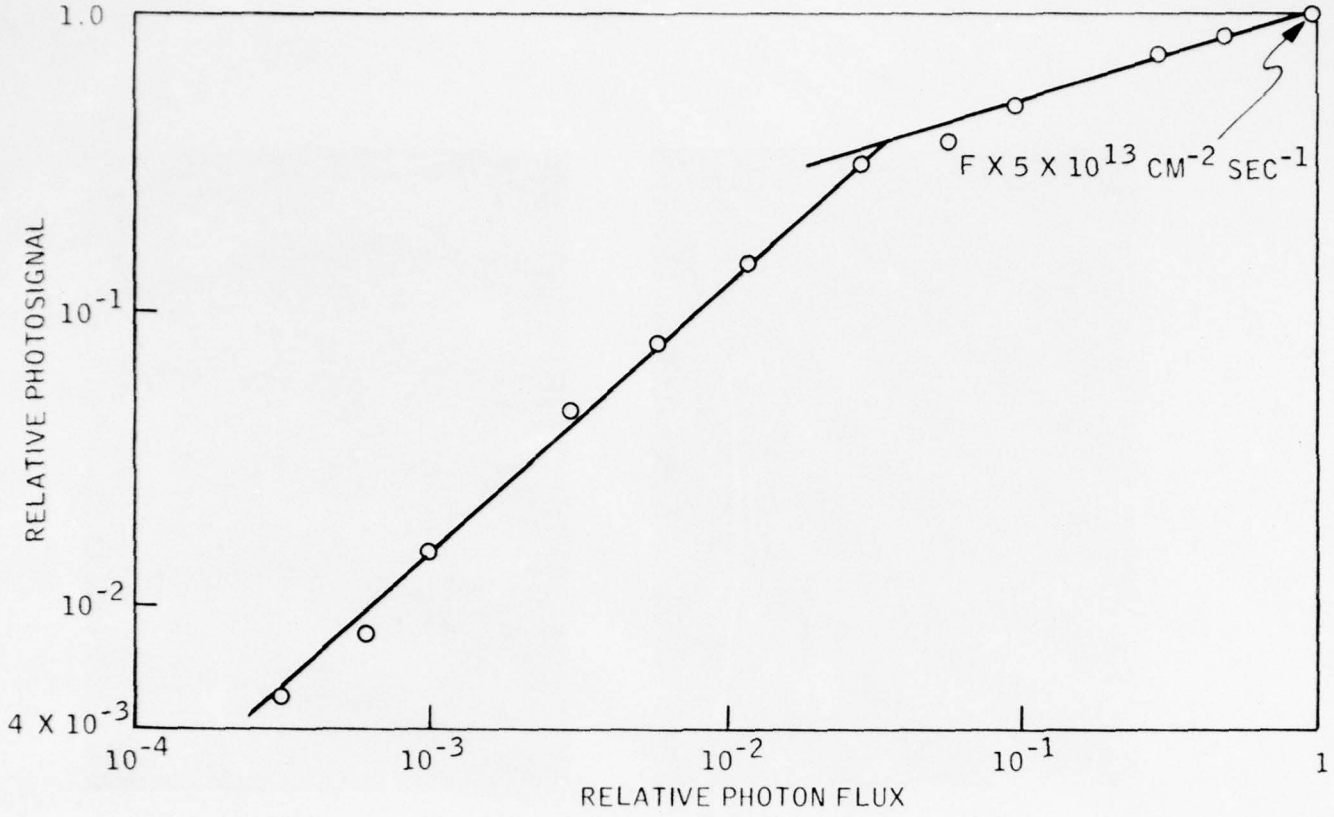
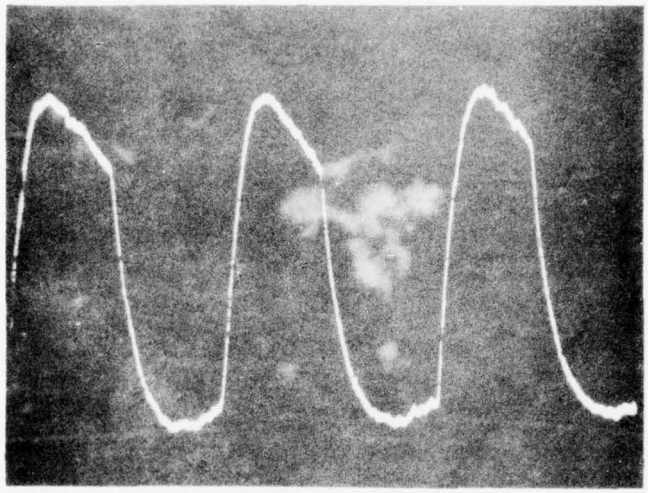
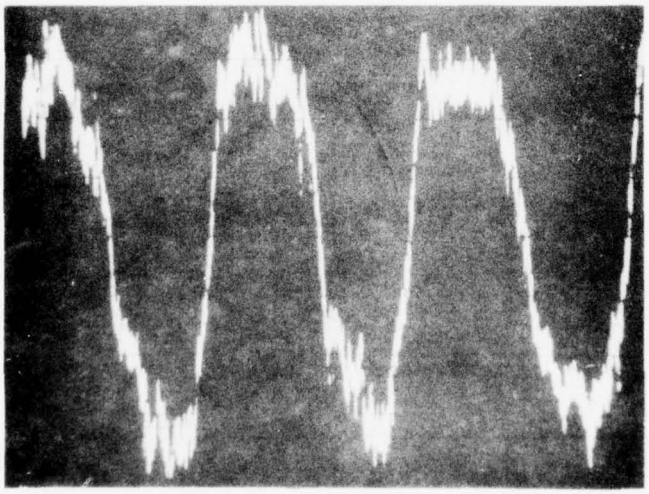


Figure 29. Photosignal vs photon flux intensity at 3.0 eV for LPE-29-142 GaP:Cu photoconductor.



a



b

Figure 30. Photosignal of LPE 29-142 at (a) 20°C and (b) 90°C. Scales are the same for both measurements.

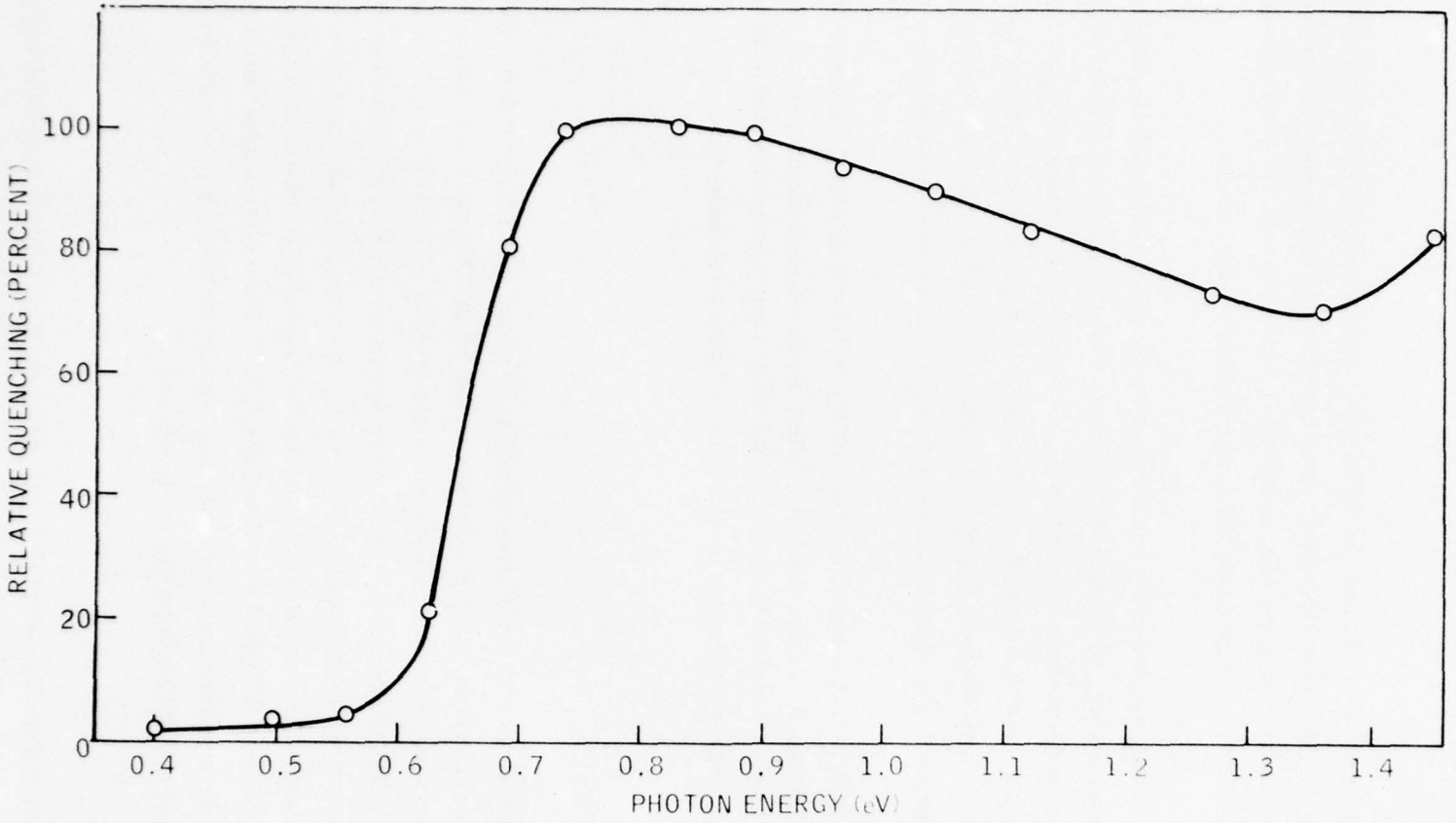


Figure 31. Optical quenching in LPE-18-95 GaP:Cu photoconductor.

of such an optical quenching experiment. An LPE GaP:Cu sample is illuminated with radiation of energy greater than the bandgap energy. At the same time, it is illuminated with less than bandgap energy photons whose energy is varied from 0.4 eV to~1.5 eV. Note that the quenching effect has an edge near 0.65 eV and then stays nearly constant for higher energy photons.

In Figures 21, 25, and 29, we plotted the relative photosignal for three LPE GaP:Cu samples. For each of these samples, the dependence initially was linear, with a transition to sublinear at higher flux intensities. Each of these samples had relatively low (~1000 Ω) resistance. In Figure 32, we show the photosignal photon flux intensity characteristic for a high resistance (~10^9 Ω) GaP: Cu sample. Note that the characteristic is decidedly superlinear, with a hint of linear dependence at the highest flux intensities. The significance of this result will be discussed in Section IV.

We routinely fabricated Schottky barriers on the LPE layers in order to profile the carrier concentration by C-V techniques. As we reported earlier, these diodes are photosensitive out to 5.5 eV[aa]. Figure 33 shows the relative spectral response of a Schottky barrier diode fabricated on an undoped LPE layer. The peak quantum efficiency for one of these diodes is typically~0.5.

2. Transport Measurements

Hall and resistivity analyses were routinely made on samples from each BSG growth run which yielded crystals large enough for this type of analysis. Most of the LPE layers were grown on heavily doped low-resistivity substrates, and hence it was not possible to perform Hall analysis on these samples. However, a few LPE layers were grown on compensated (Czochralski substrates and measurements were made on one of these layers. All of the Hall and resistivity data were taken using the van der Pauw technique. The samples were lapped flat and chemically polished in a hot potassium ferricyanide etch [0.5 mole % KOH, 1.5 mole % $K_3Fe(CN)_6$]. For n-type samples, ohmic contacts were achieved by alloying from small peripherial In:1%Te dots at 680°C. For p-type samples In:1% Zn dots were alloyed at 420°C to form the ohmic contacts.

[aa] The development of Schottky barrier GaP photodetectors is currently funded by Honeywell.

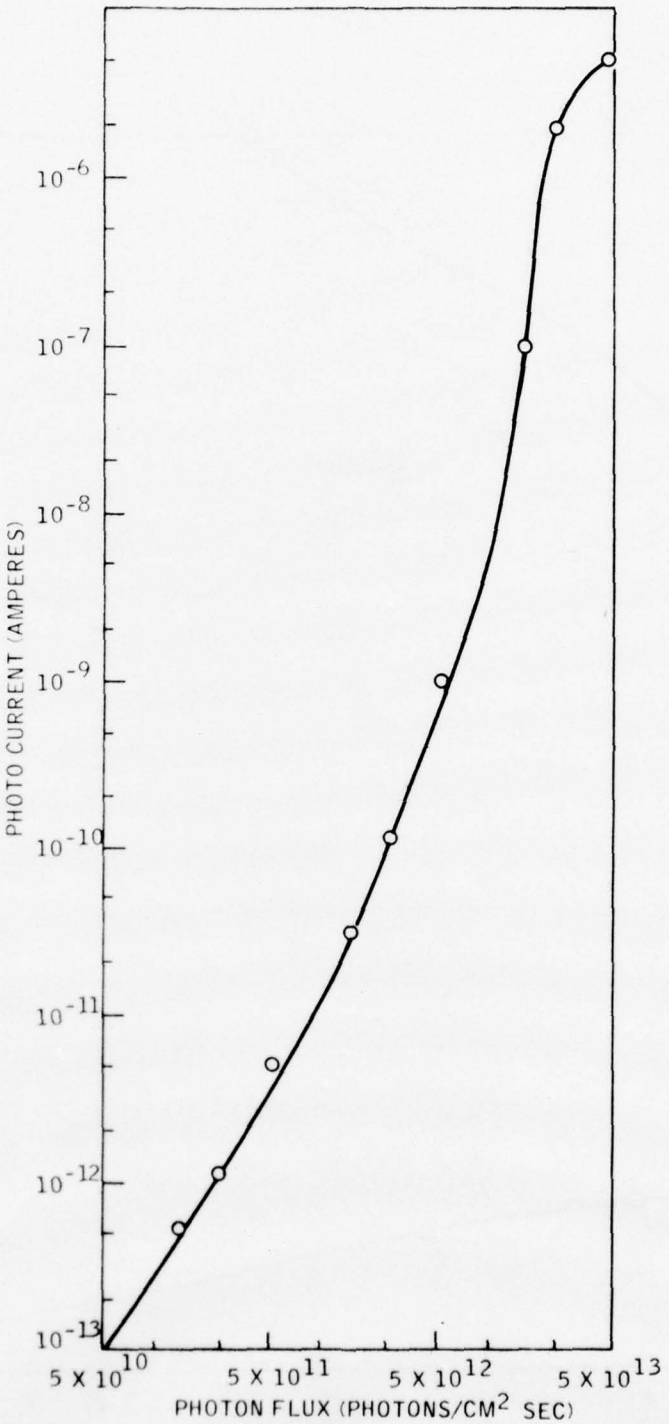


Figure 32. Photosignal vs photon flux intensity for a high resistivity (*LPE-18-95*) *GaP:Cu photoconductor.*

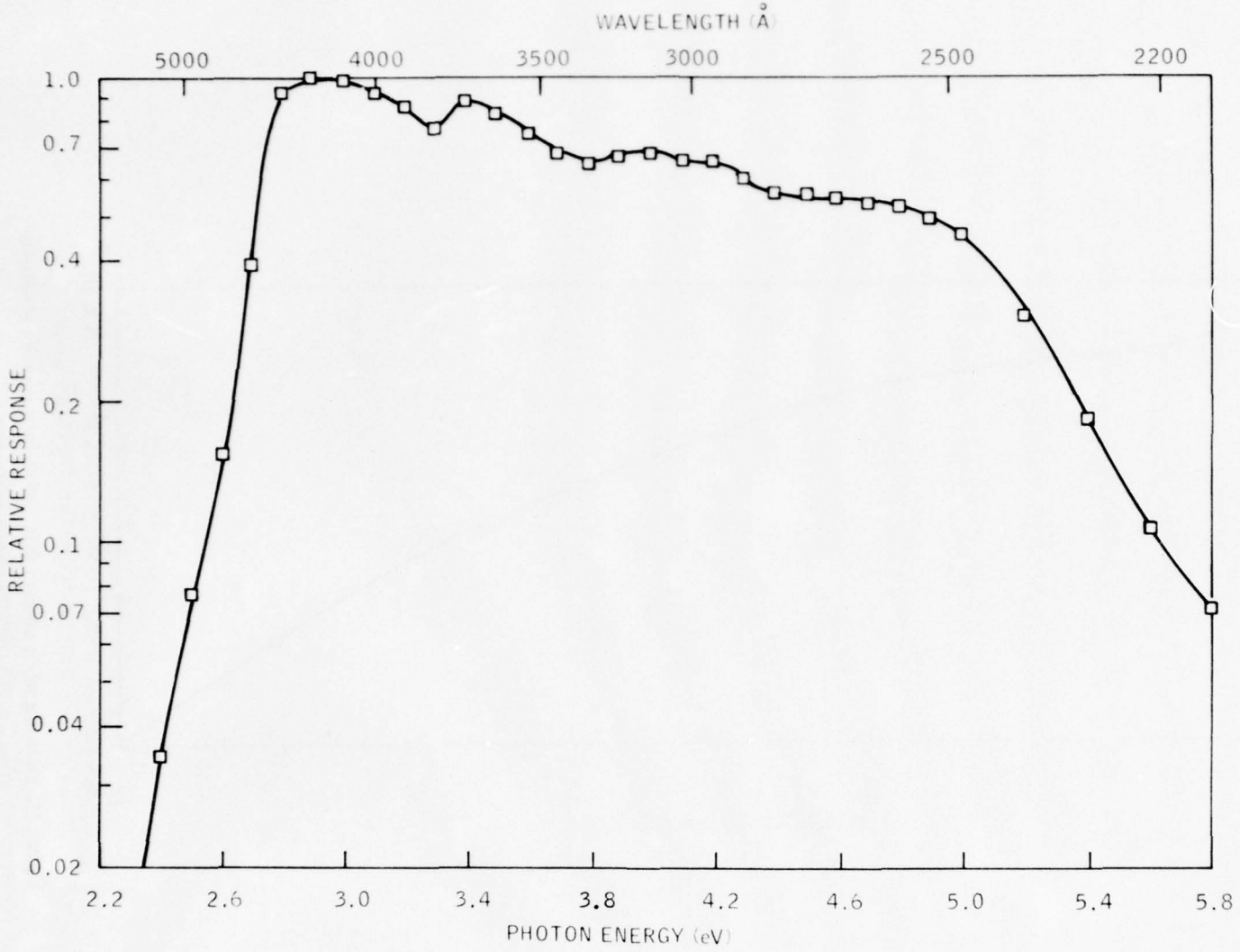


Figure 33. Spectral response of a Schottky barrier photodiode fabricated on LPE-13-76.

The material parameters which generally are available from Hall analysis are majority carrier type and concentration, majority carrier activation energy and the temperature dependence of the resistivity and majority carrier mobility. The first three of these parameters were of the most interest to us in evaluationg the material from these early growth runs. Table 5 tabulates these parameters for the BSG growth runs which were conducted during the first half of this program.

During the second half of the program, we became concerned with the carbon doping of the SSD growths. Consequently, for those runs, we began to investigate the degree of compensation and the low temperature scattering mechanisms which limit the mobility. In Table 6, we tabulate the Hall data for the bulk growth runs which were conducted during the second half of the program.

One of the reasons for developing the BSG growth technique was to obtain larger, more uniform solution-grown GaP crystals than were obtainable from the random nucleation solution growth process. Hall data from growth run BSG-10, which, as discussed earlier, produced large single crystals, demonstrate the uniformity of the BSG material. Two Hall samples, spaced about 0.3 cm apart, were cut from a single wafer. The carrier concentration over $T^{3/2}$ versus $10^3/T$ is plotted in Figure 34 for each of these samples. The carrier concentrations at each temperature for these two samples are within experimental error of being equal to each other.

In each of the Hall runs, the temperature dependence of the mobility was measured. Figures 35 and 36 are plots of the mobility as a function of temperature for two n-type BSG samples. Included are straight lines showing respectively the $T^{-3/2}$ and $T^{-1/2}$ temperature dependence of acoustic phonon and space charge scattering.

Figure 37 shows the temperature dependence of the mobility for three p-type BSG samples. The theoretical curves for optical phonon scattering and ionized impurity scattering are included.

Because of the persistence of carbon as an acceptor impurity in the BSG and SSD growth runs, we carefully examined the Hall data for the last several p-type growth runs. Figure 38 is a plot of $p/T^{3/2}$ versus T^{-1} for BSG 1→4. Note that there is a rather well defined freeze-out regime, so the activation energy is readily obtained. Figure 39 gives the temperature dependence of the Hall coefficient for the same four BSG growth runs. The significance of the roll-over in the Hall curve

TABLE 5.

TABULATION OF HALL DATA, First Half of Program

BSG Growth Run Number	Carrier Type	Room Temperature Carrier Concentration (cm^{-3})	Principal Donor/Acceptor Energy (eV)
1	Insufficient material for analysis	---	---
2	Polycrystalline material	---	---
3	No growth occurred	---	---
4	p	1×10^{17}	< 0.060
5	Insufficient material for analysis	---	---
6	p	$\sim 1.2 \times 10^{10}$	---
7	p	5×10^{16}	0.042
8	n	7×10^{17}	0.095
9	No growth occurred	---	---
10	n	3×10^{17}	0.093
11	Insufficient material	---	---
12	Polycrystalline material	---	---
13	p	9×10^{15}	< 0.060
14	Polycrystalline material	---	---
15	n	8×10^{17}	0.090
16	n	2.9×10^{18}	0.097
17	n	2.1×10^{17}	0.089
LPE-10-63	n	6.8×10^{17}	0.095

TABLE 6.

TABULATION OF HALL DATA, Second Half of Program

Growth Run Number	Carrier Type	Room Temperature Carrier Concentration (cm^{-3})	Principal Acceptor Activation Energy (meV)	Mobility at 300°C (cm^2/V-sec)	Mobility at 77°C (cm^2/V-sec)	Donor Concentration (cm^{-3})	Acceptor Concentration (cm^{-3})
BSG-18*	p	3.8×10^{16}	< 50	76	407	—	—
BSG-19	p	2.3×10^{16}	46	105	1621	5×10^{15}	3.2×10^{16}
BSG-20**	—	—	—	—	—	—	—
BSG-21	p	7.1×10^{16}	42	115	693	5.8×10^{16}	1.3×10^{17}
BSG-22	p	8.9×10^{17}	41	121	726	—	—
SSD-1	p	1.1×10^{17}	40.5	106	870	2.8×10^{16}	1.7×10^{17}
SSD-2	p	1.3×10^{17}	40.5	98	986	2.6×10^{16}	2.0×10^{17}
SSD-3	p	6.6×10^{16}	41.8	99	509	3.8×10^{16}	1.1×10^{17}
SSD-4	p	1.6×10^{17}	39.7	112	1373	2.4×10^{16}	2.3×10^{17}
SSD-5***	n	—	—	—	—	—	—

*This run was doped with copper.
**Polycrystalline growth — no data obtained.
***Polycrystalline growth — only carrier type obtained.

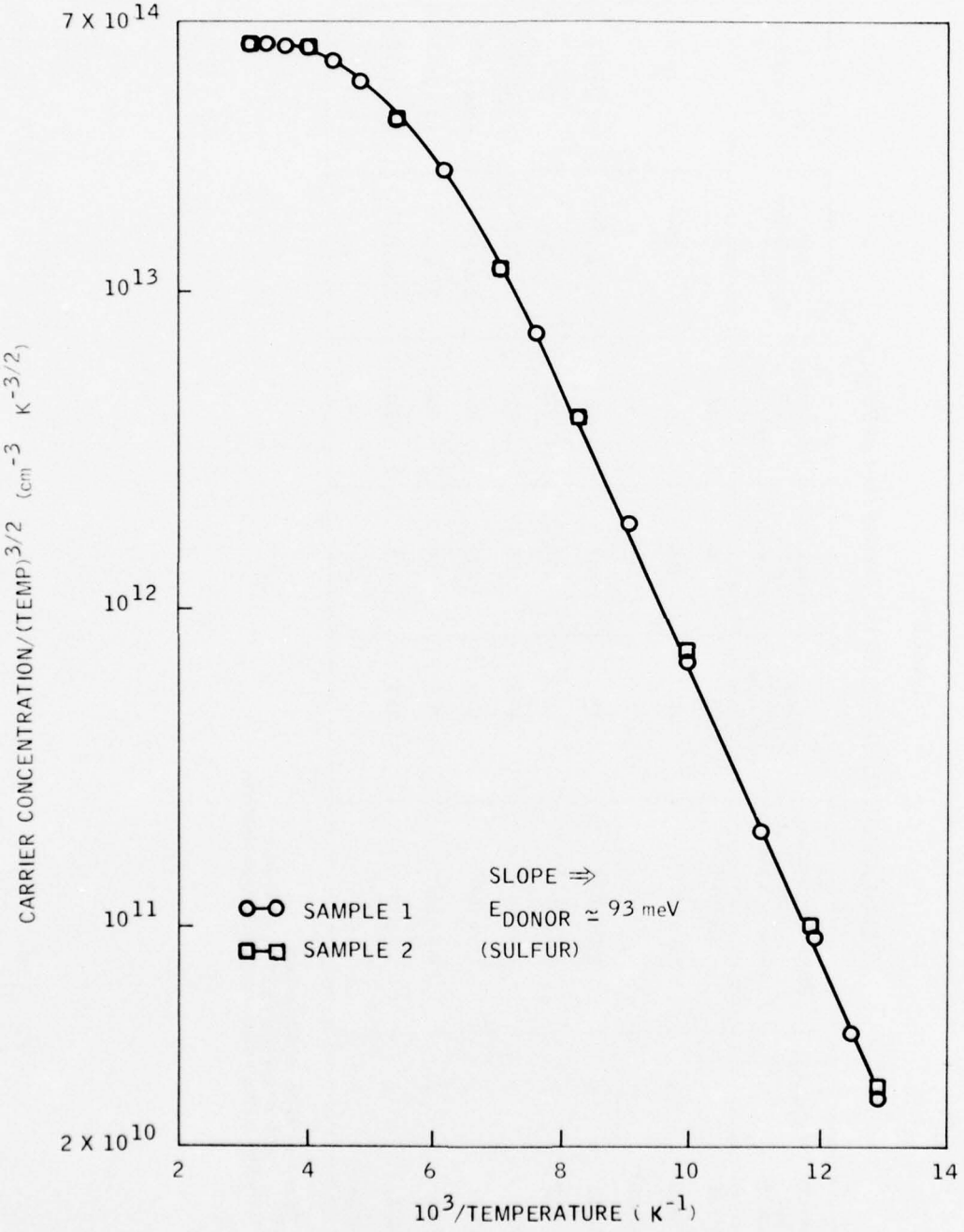


Figure 34. Carrier concentration divided by (temperature)$^{3/2}$ for two samples from BSG-10.

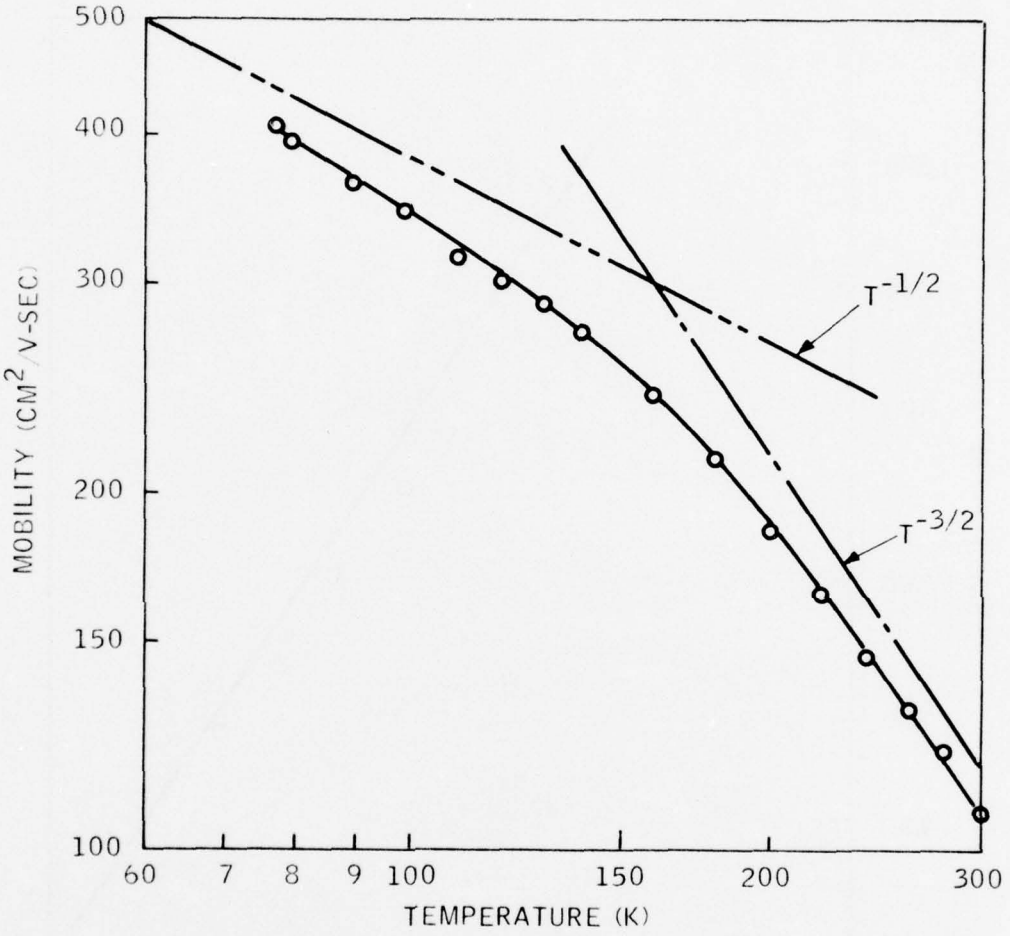


Figure 35. Temperature dependence of the mobility for an n-type sample from BSG-10 ($n = 3 \times 10^{17}$ cm^{-3}).

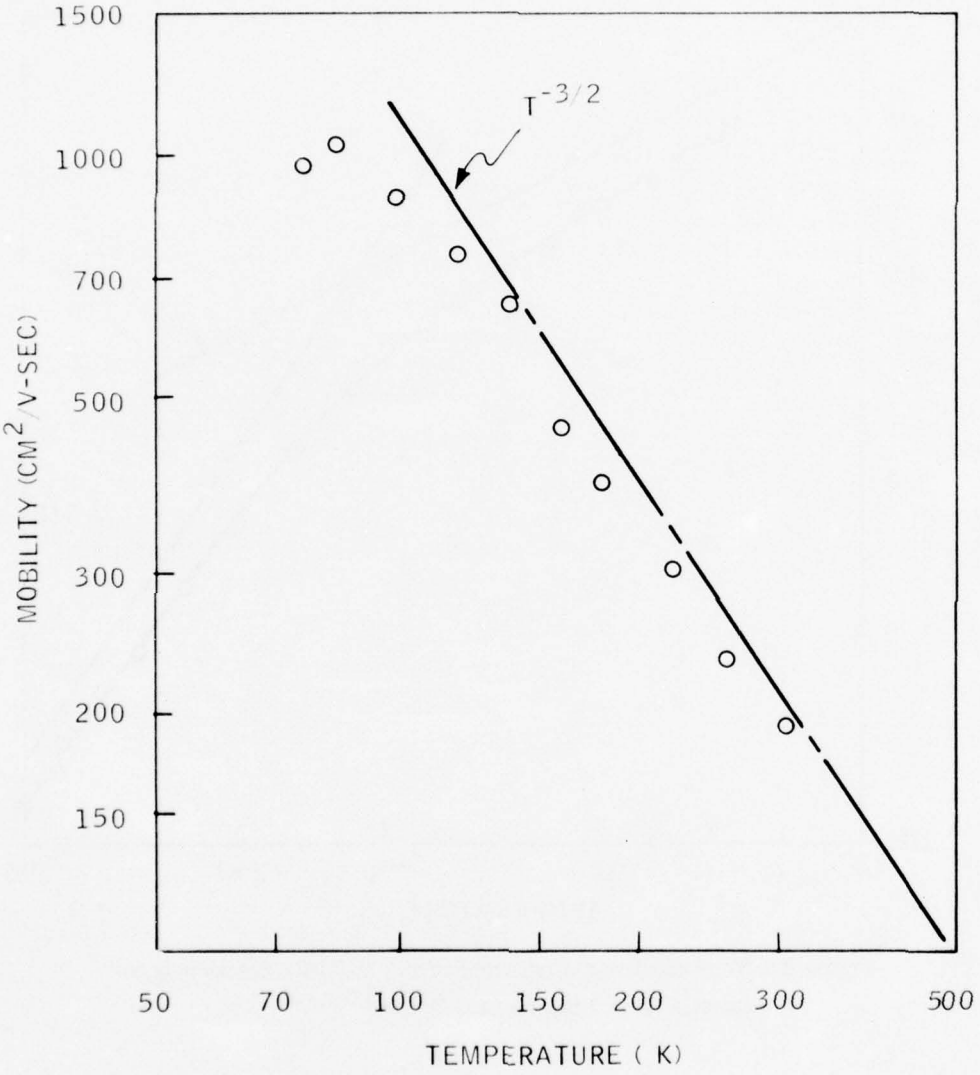


Figure 36. Temperature dependence of the mobility in an n-type sample from BSG-15 ($n = 8 \times 10^{17}$ cm^{-3}).

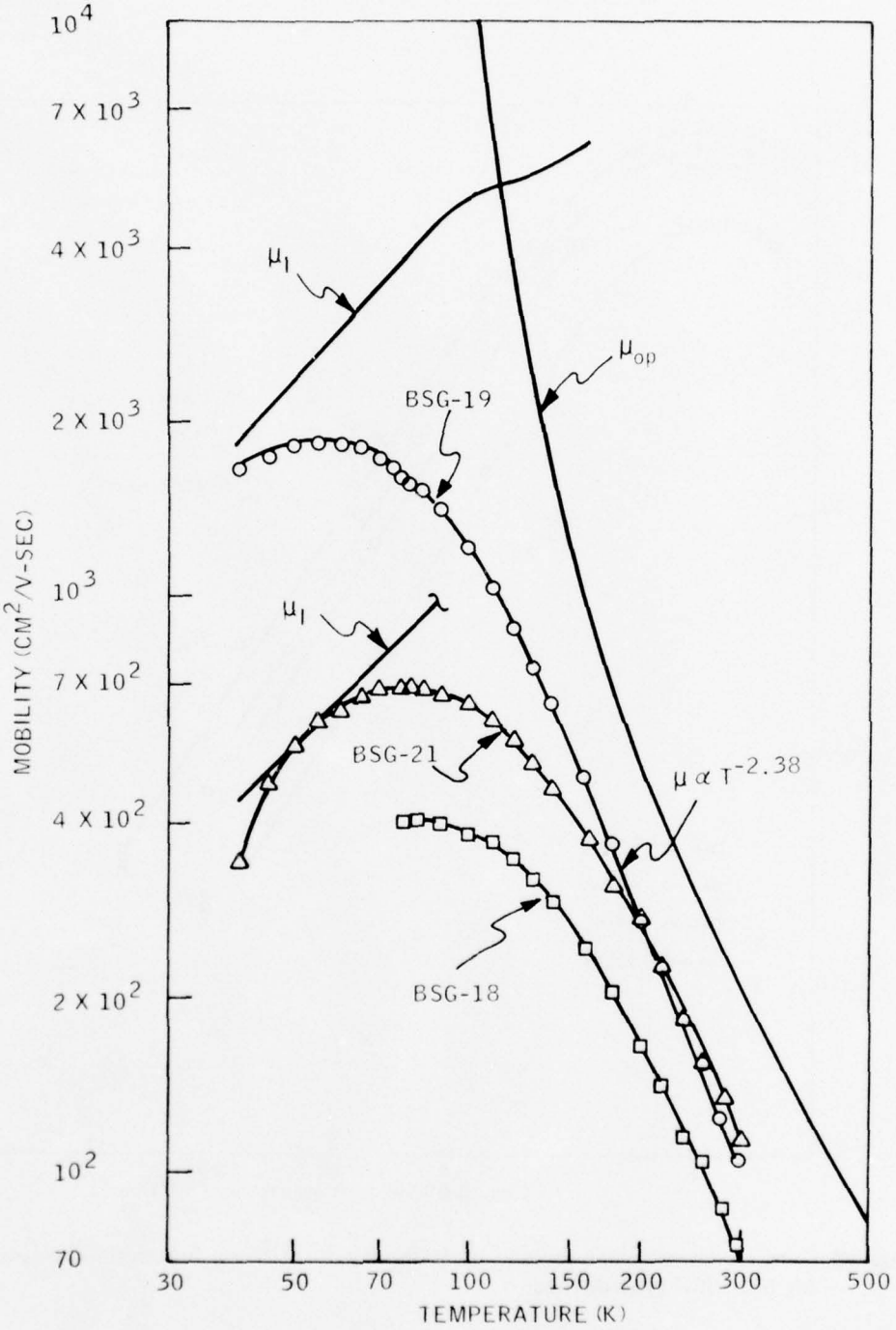


Figure 37. Mobility vs temperature for three BSG samples. The theoretical curves for optical phonon scattering and ionized impurity scattering are included.

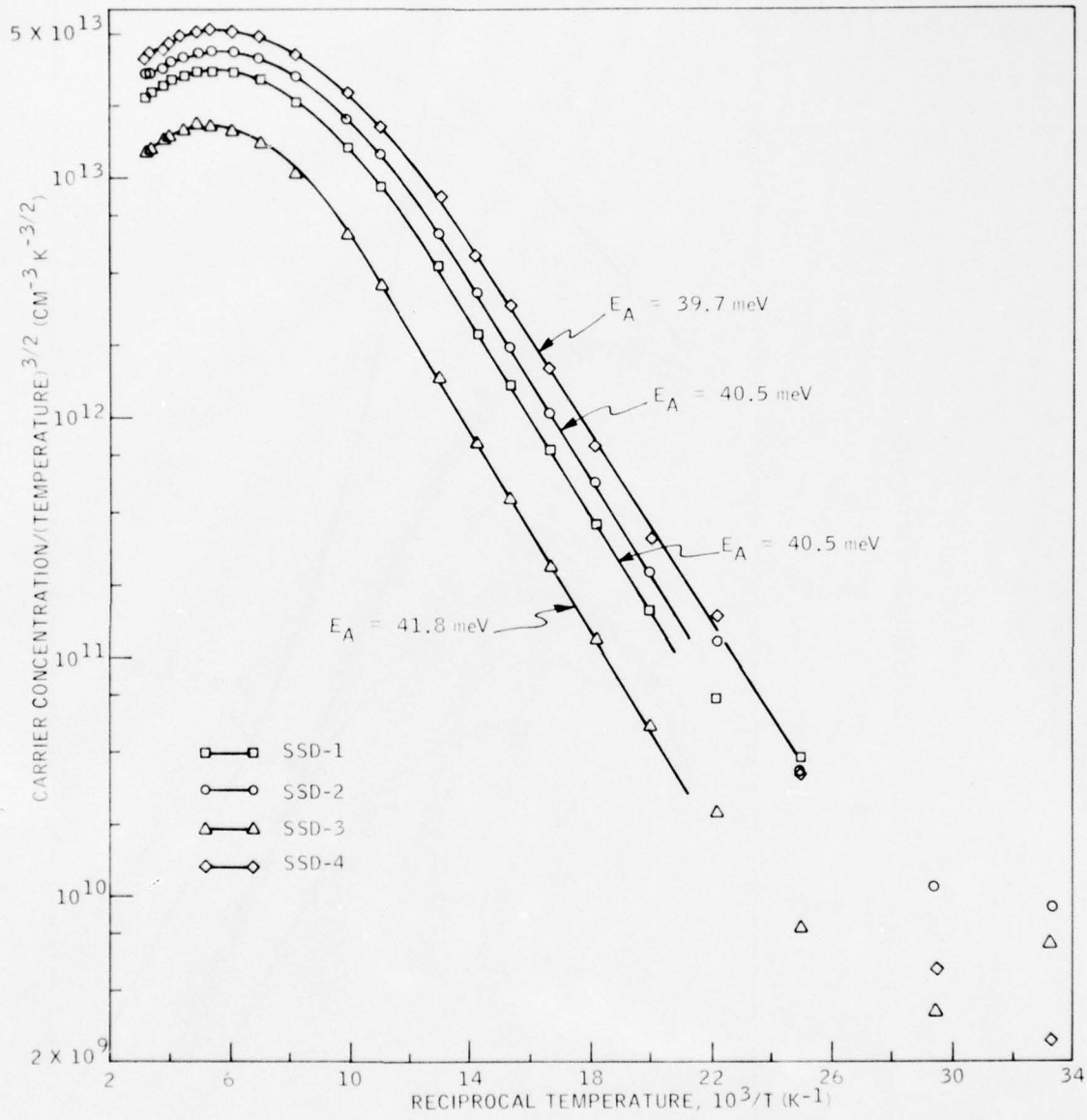


Figure 38. Carrier concentration divided by (temperature)$^{3/2}$ as a function of reciprocal temperature for four BSG growth runs.

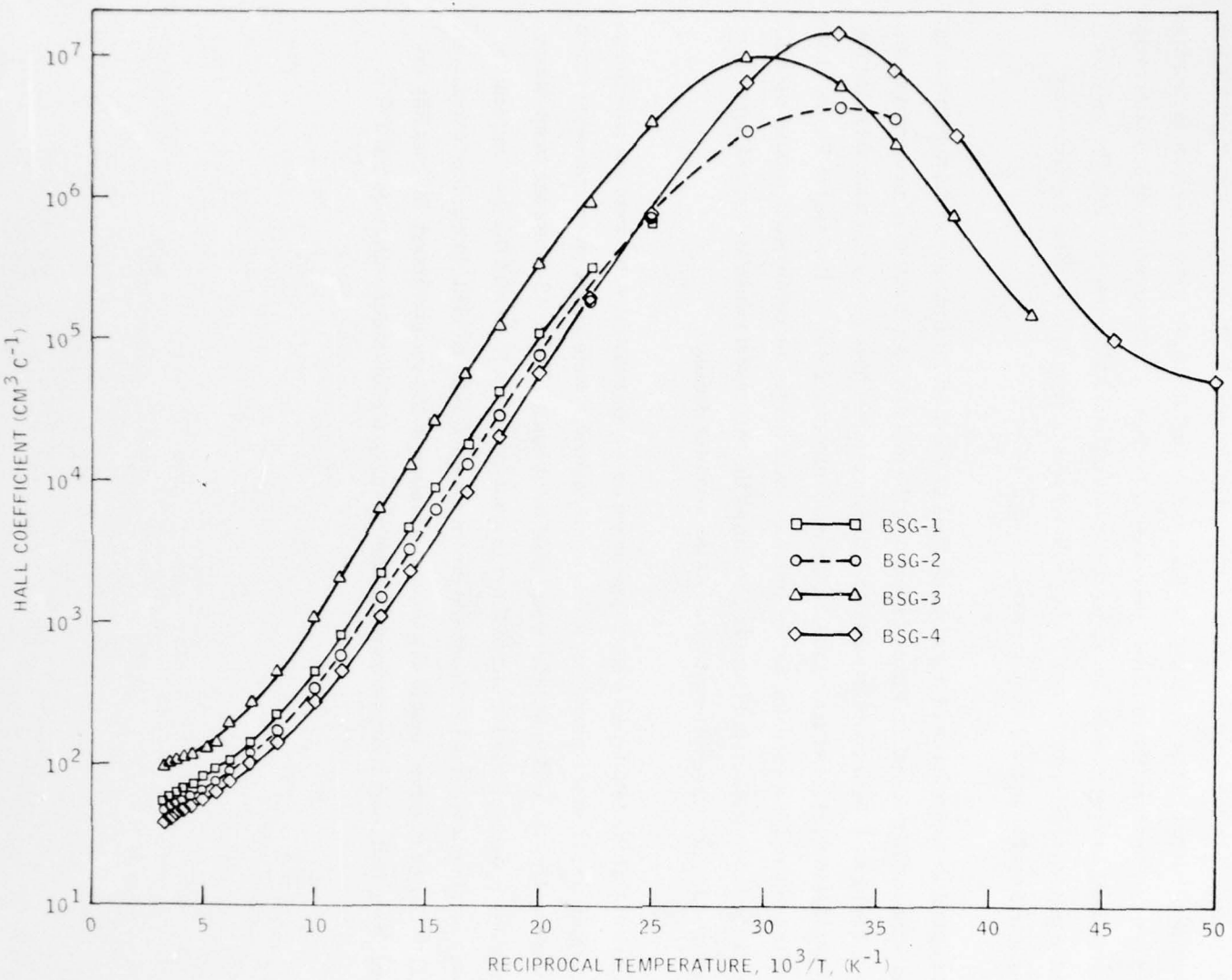


Figure 39. Hall coefficient vs. reciprocal temperature for four BSG growth runs.

which occurs at low temperatures will be discussed in Section IV. As shown in Figure 40 the temperature dependence of the resistivity has the same general shape. As the temperature is decreased from room temperature, the resistivity decreases. It reaches a minimum and then increases sharply with decreasing temperature in the carrier freeze-out regime. At low temperatures the restivity reaches a plateau and increases very slowly with decreasing temperature. This dependence is readily interpretable and will be discussed in Section IV.

The temperature dependence of the mobility gives us the most information about the scattering mechanisms in the material. In Figure 41, we plot the mobility as a function of temperature for samples BSG 1 to 4. Near room temperature, all four samples have nearly the same value for the mobility. However, at lower temperatures, the mobilities differ widely. Included in Figure 41 is a plot of the theoretical expression for the mobility when limited by combined non-polar optical and acoustic mode scattering. Figure 41 also shows the theoretical values for ionized impurity limited mobility for three different values of the acceptor density.

Because most of the LPE layers were n-type layers on n-type substrates, we were not able to make Hall measurements on these samples. A few layers, however, were grown on compensated Czochralski substrates; for these samples, Hall data could be obtained. Figure 42 shows the temperature dependence of the mobility for one of these LPE n-type layers. Note that the low-temperature mobility is rather low. This LPE layer was grown from a Cu-doped melt. In previous experiments with GaP:Cu, we observed that as the Cu concentration in the melt increased, the mobility decreased. Note that, near room temperature, the mobility for this sample also varies as $T^{-3/2}$.

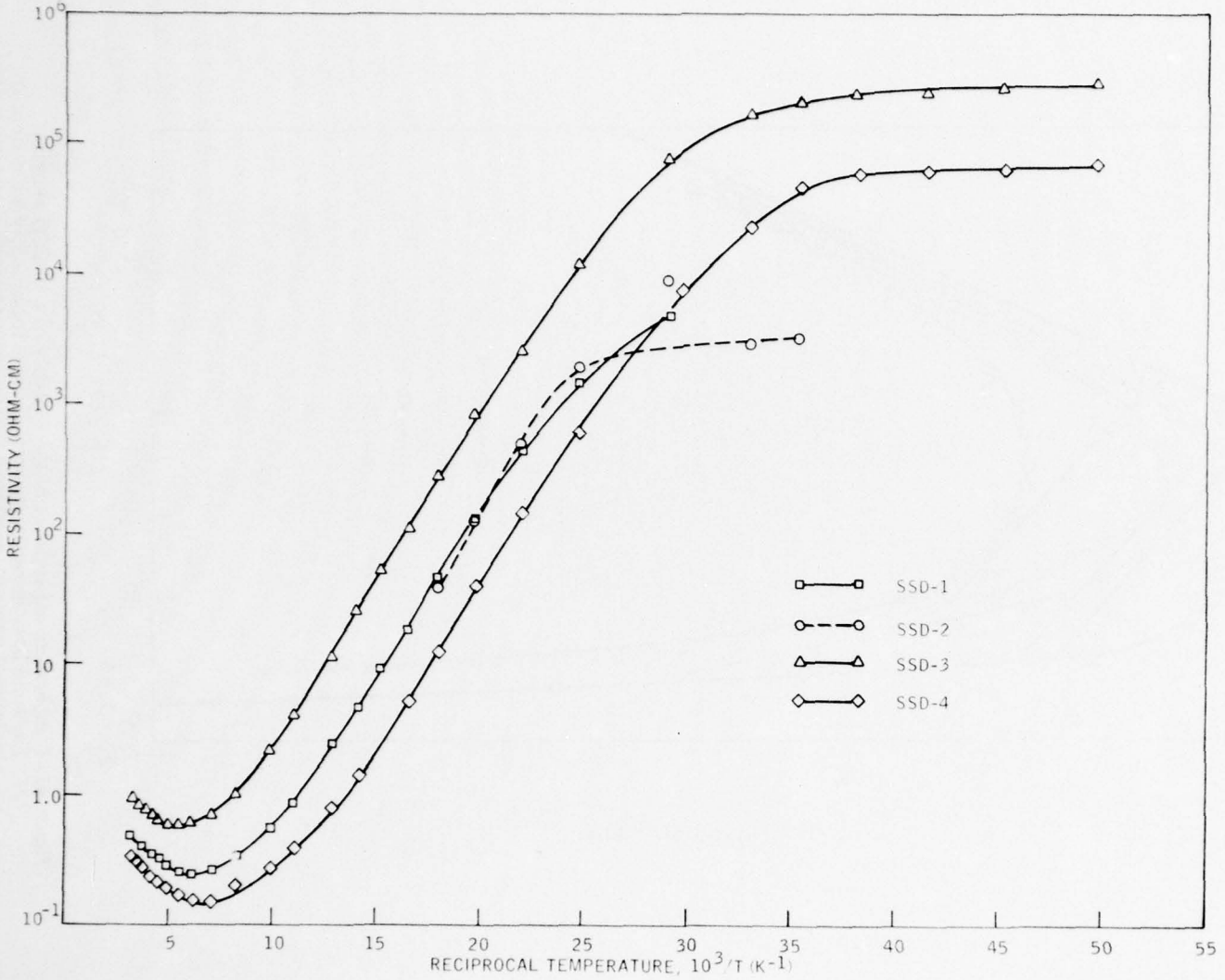


Figure 40. Resistivity vs reciprocal temperature for four BSG growth runs.

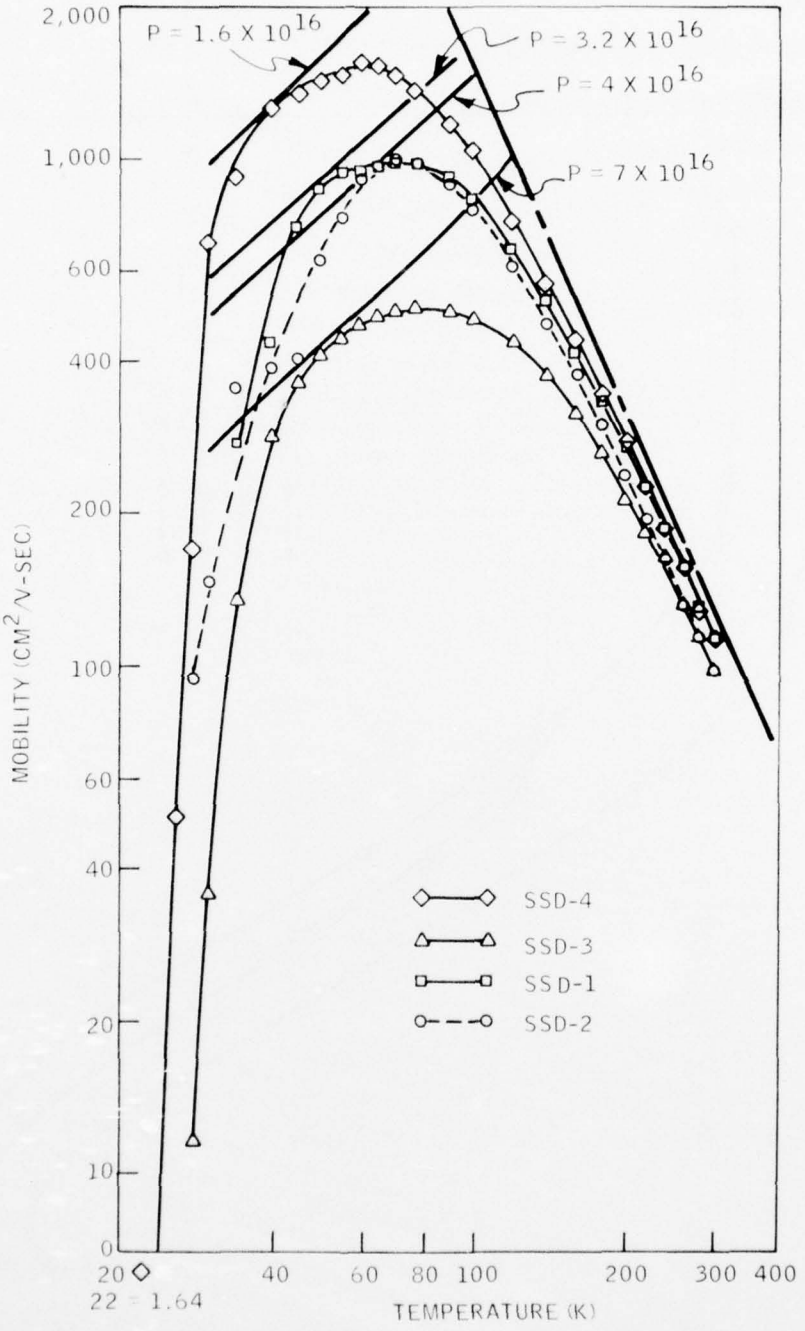


Figure 41. Temperature dependence of the mobility of four SSD samples. The solid lines show the theoretical value for mobility when limited by ionized impurity scattering for the indicated carrier concentrations. The broken line shows the theoretical value for the mobility when limited by combined acoustic and non-polar optical mode scattering.

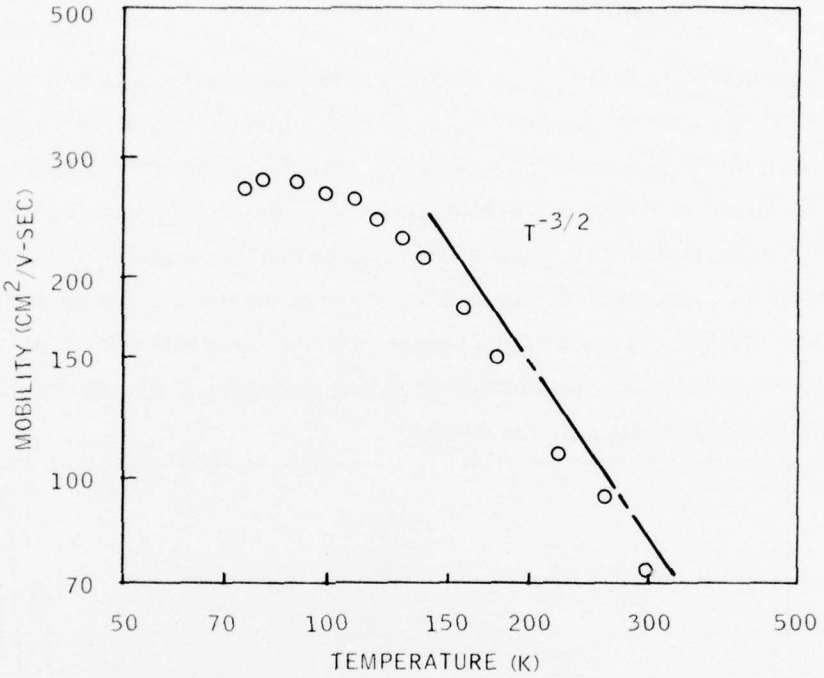


Figure 42. Temperature dependence of the mobility for an LPE 10-62 n-type sample.

3. IR Spectroscopy

As discussed in the previous section, carbon has turned out to be an important impurity in GaP for us to identify and characterize. IR spectroscopy has proven to be a useful technique in identifying shallow donors and has been adapted to identify acceptors in GaP. We have a unique capability at the Honeywell Research Center in our ability to measure IR spectra in semiconductors using a Fourier transform spectrometer. Because of the versatility of this instrument, we have been able to use three different phenomena to identify carbon in GaP. These rely on the measurement of:

The local mode absorption in n-type crystals.
The excitation spectrum of carbon in p-type crystals.
The extrinsic photoconductivity in p-type crystals.

In this section, the spectra which are measured in each of the three methods will be presented to illustrate the different methods of detecting the carbon impurities. In each case, only one spectrum

will be presented as an illustration.

a. Local Mode Absorption—A portion of the IR absorption spectrum of an n-type crystal is shown in Figure 43 to illustrate the method used to identify carbon in n-type crystals. This is a portion of the absorption spectrum of crystal BSG-10 taken with the sample at both 82 K and at 5 K. In the center of the figure, the strong absorption line is due to the $1s - 2p_0$ transition in sulfur. As can be seen, the intensity of this line increases dramatically when the sample is cooled from 82 K to 5 K. In fact, this line was totally absorbing at 5 K because of the thickness of the sample used in this measurement. Similarly, the sulfur lines between 700 cm^{-1} and 800 cm^{-1} were totally absorbing in this sample. Nevertheless, the presence of the strong absorption at 577 cm^{-1} clearly identified sulfur as the dominant shallow donor in this crystal.

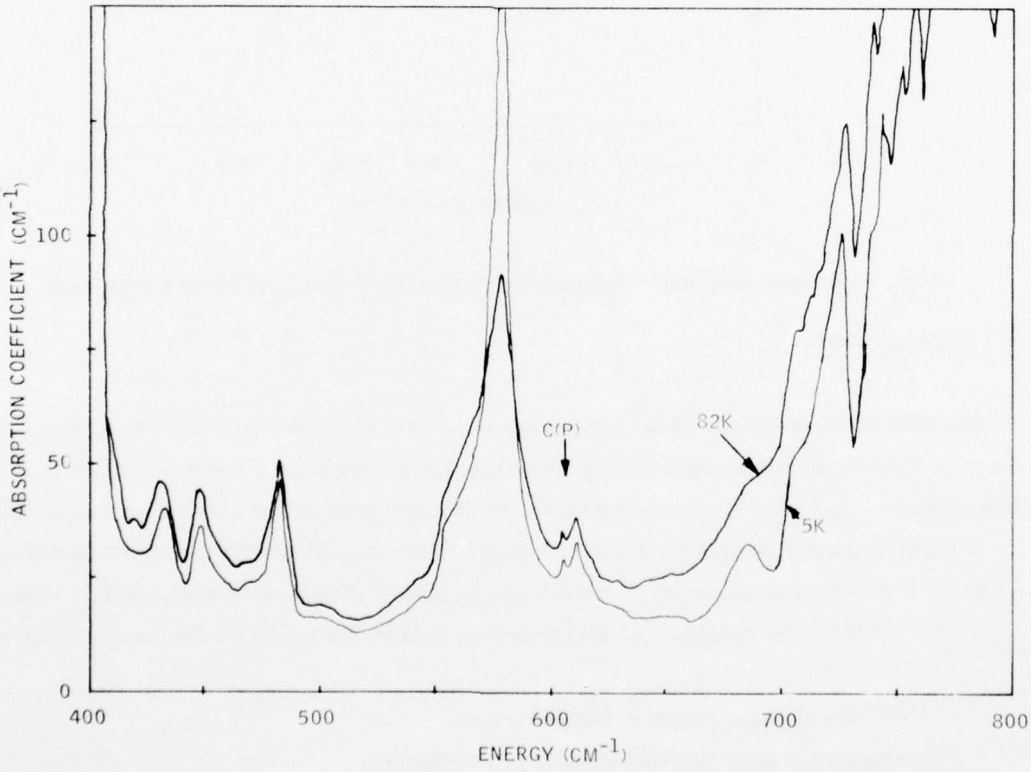


Figure 43. Absorption coefficient as a function of wave number for BSG-10 at 82K and 5K.

An additional absorption line at 606 cm^{-1} is observed at both 82 K and 5 K with no change in intensity. The fact that its intensity did not change with temperature indicates that it is a lattice

local mode vibrational line due to carbon on the phosphorus sites. Since the crystal is n-type, these impurities are compensated, so would not be directly measurable in electrical measurements.

b. Excitation Spectrum—The absorption spectrum of p-type crystal, SSD-3, is shown in Figure 44. The sample used had a room temperature carrier concentration of 6.6×10^{16} holes/cm^3 and had a freeze-out of the Hall coefficient corresponding to an activation energy of 38 meV, indicative of carbon. Two absorption lines due to carbon are observed, a strong line at 269 cm^{-1}, but this is also observed in n-type crystals, so it is assumed to be a lattice absorption line. The sample is opaque in the spectral region from about 310 cm^{-1} to 400 cm^{-1} because of the strong optical phonon absorption lines in this region (i.e., the reststrahlen region). The ordinate is expressed as an absorbance A, which is defined at $\log_{10}T$, where T is the transmittance of the sample.

c. Extrinsic Photoconductivity—The photoconductive response of crystal BSG-4 in the 400 to 4000 cm^{-1} spectral interval is shown in Figure 45. From Hall measurements, this crystal was determined to be p-type with a carrier concentration of about 3×10^{17}/cm^3. Note that there is response down to the reststrahlen band which extends from about 300 to 400 cm^{-1}. Since the lattice will be totally absorbing in the reststrahlen band, it is impossible to determine if the extrinsic edge lies within this region. Also, it should be noted that the photoconductive response is oscillatory in nature, with a period of about 400 cm^{-1}. The sharp structure in the 400 to 1000 cm^{-1} spectral region is not noise, but is due to lattice absorption. The oscillations are "damped out" at about 3000 cm^{-1}, but additional structure is observed at higher energies, indicating the presence of deeper impurity levels.

4. Junction Capacitance Studies

We have routinely measured the C-V characteristic of Schottky diodes formed on the sample surface in order to determine the impurity concentration in the GaP material which we have grown. The spatial uniformity of the carrier concentration $|N_a - N_d|$ can be determined by fabricating an array of Schottky barriers over the surface and measuring the bias dependence of the capacitance. The slope of the $1/C^2$ versus V gives the carrier concentration. Figures 46 and 47 show respectively the results of such a measurement on crystals from SSD-3 and LPE-17-94. The carrier concentration is indicated for each set of data points.

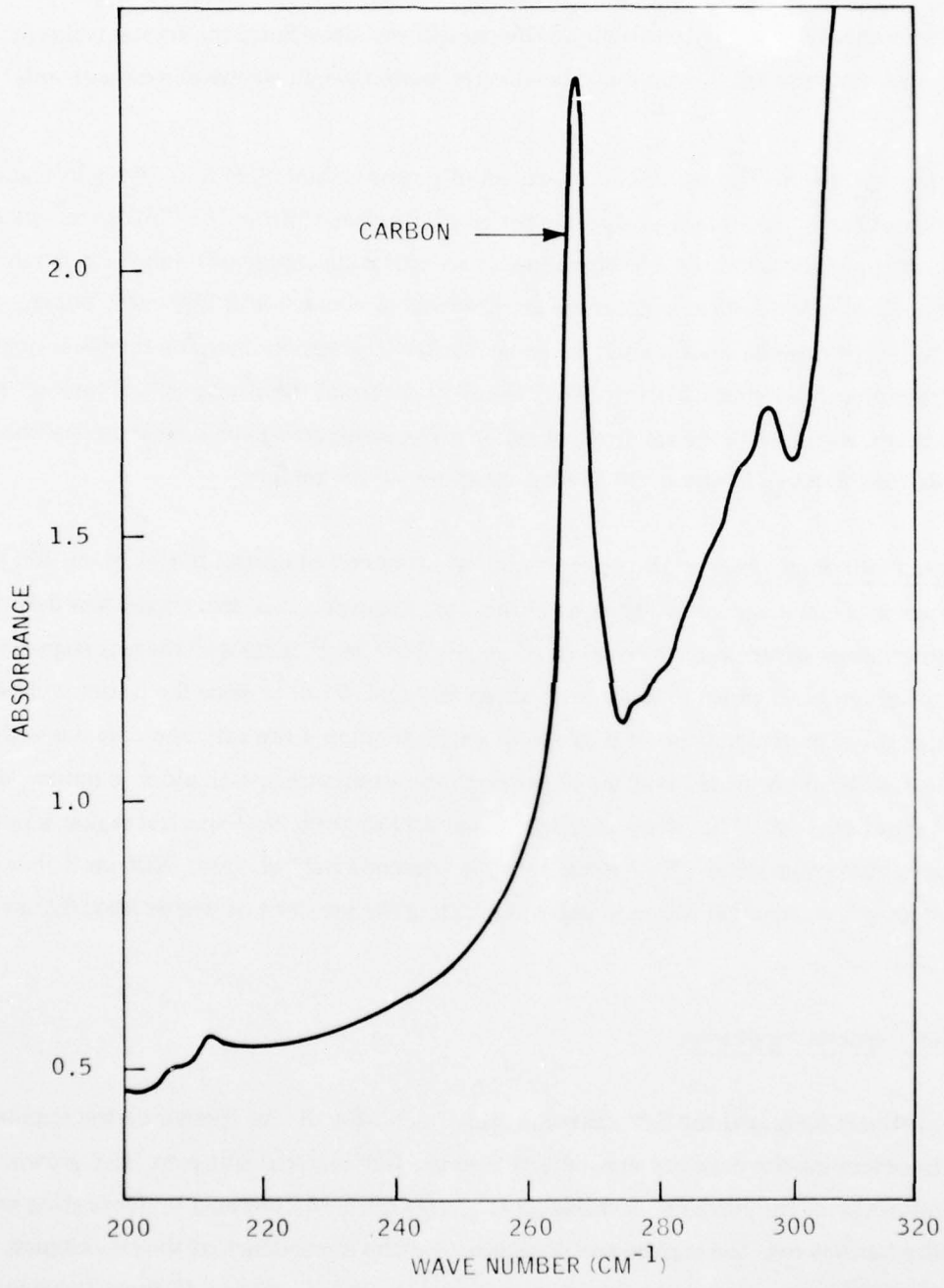


Figure 44. Excitation spectrum of carbon acceptors in GaP in the far infrared.

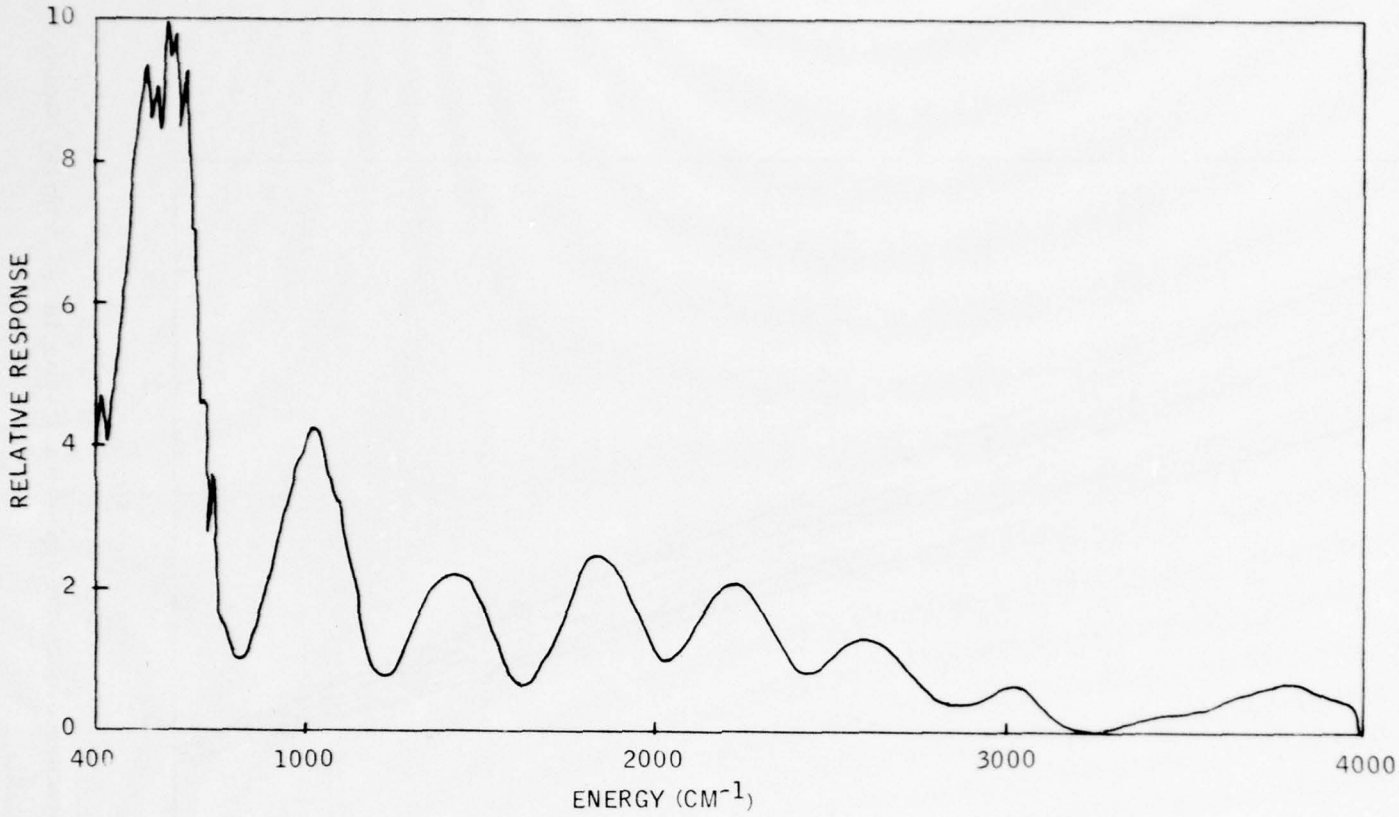


Figure 45. Relative photoconductive response as a function of wave number for BSG-4 at 7K showing the oscillatory behavior of the photoconductivity.

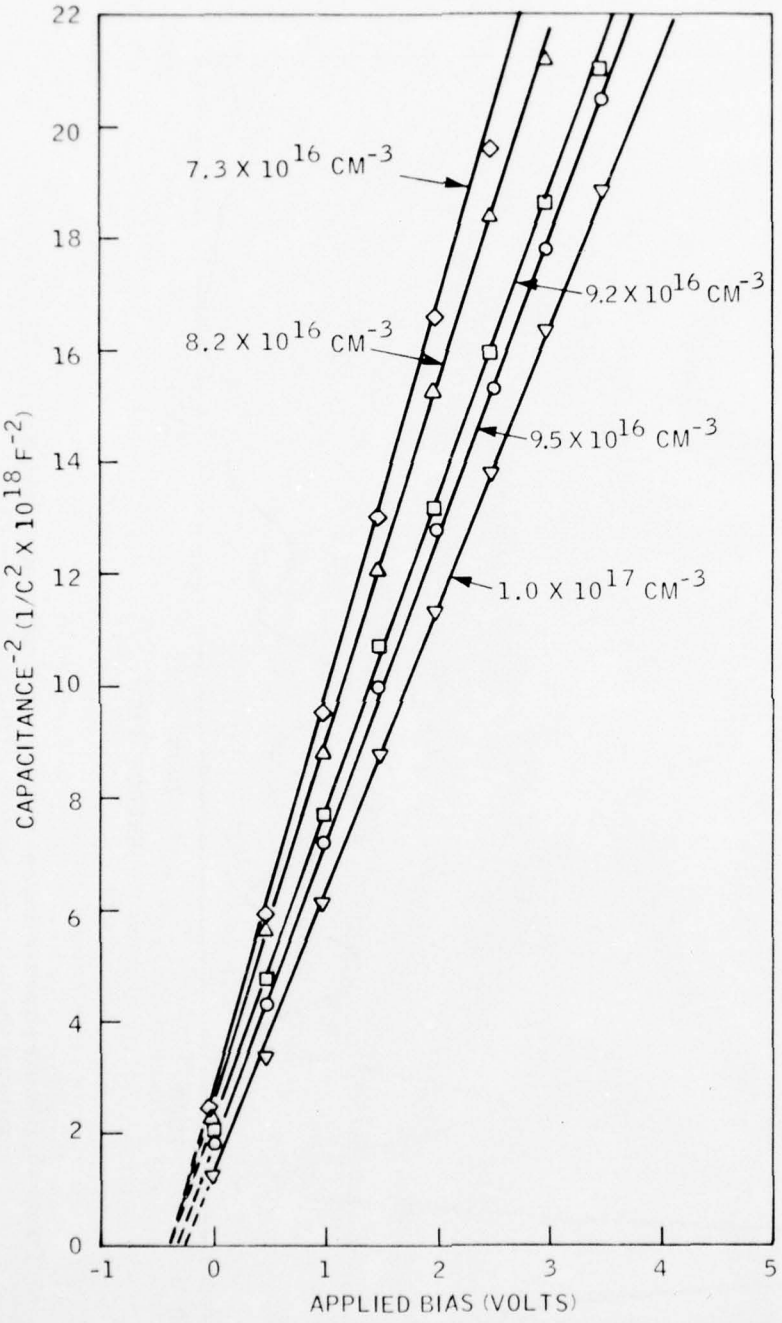


Figure 46. Inverse capacitance squared vs applied bias for five Au/GaP Schottky barriers on p-type SSD-3.

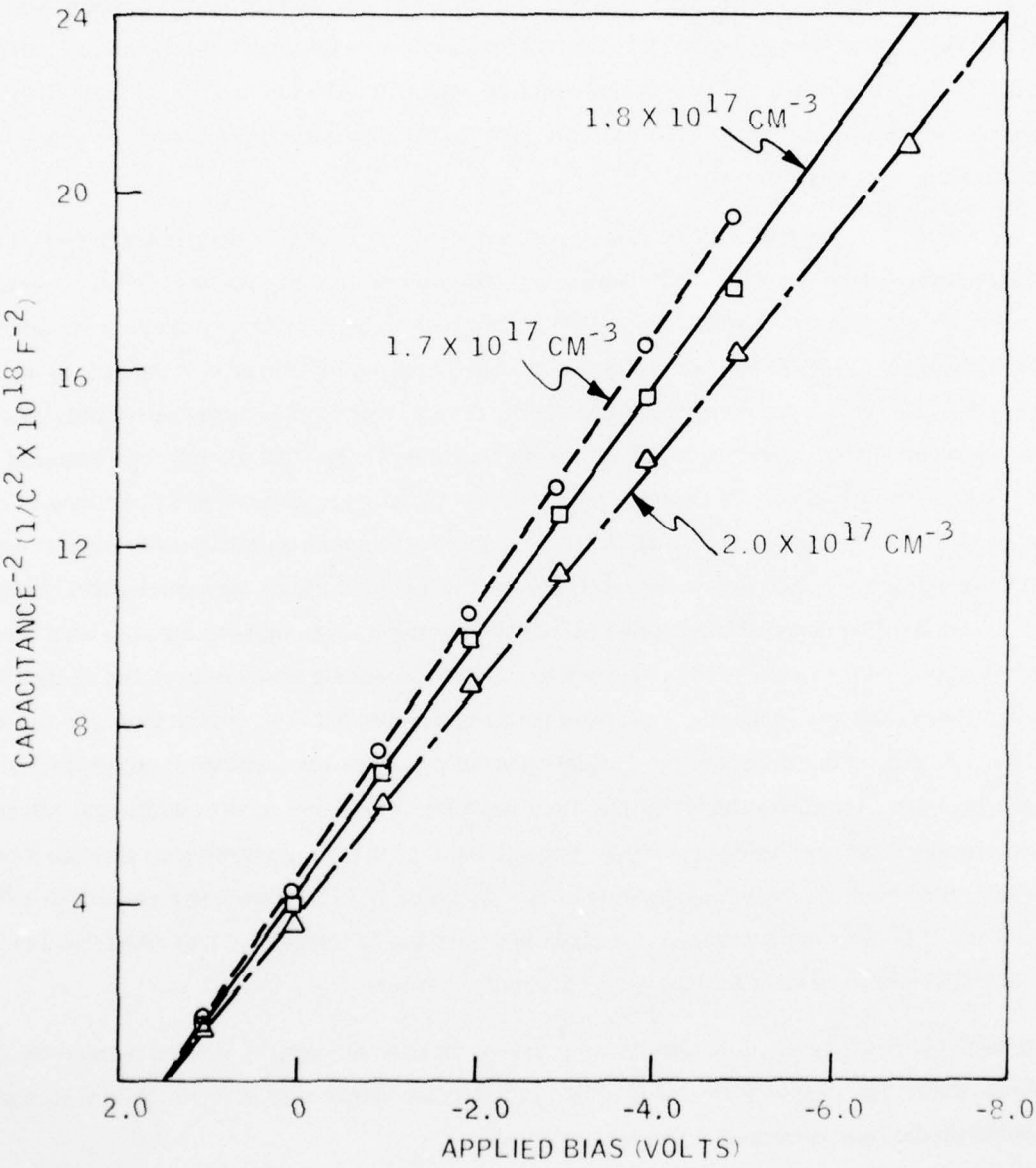


Figure 47. Inverse capacitance squared vs applied bias for three Schottky barriers on LPE-17-94.

Due to a malfunction in the growth apparatus, a thick ($\sim$60 μm) layer was grown in growth run LPE-29. The layer was angle lapped and Schottky barriers were fabricated on the lapped surface. The $1/C^2$ - V characteristic for two of these diodes, which were 15 μm and 50 μm from the growth interface, are shown in Figure 48. These data show that the carrier concentration increases with distance from the growth-interface.

During this program, two capacitive techniques were used to investigate deep levels in GaP. The first technique, which is termed "admittance spectroscopy of impurity levels in Schottky barriers," has been recently described by D.L. Losee[5]. In this technique, a small a-c voltage is applied to a Schottky barrier diode. As the bias voltage is changed, the quasi-Fermi level is swept through the various defect levels. As the Fermi level crosses the defect level, charge carriers are freed; this, in turn, alters the charge distrubution within the depletion layer. The differential capacitance is determined by the magnitude of the charge oscillation, $\delta\rho$, per voltage amplitude, δV. So long as the frequency of voltage oscillation is sufficiently low and the temperature sufficiently high so that the charge can move in and out of the level, the level will contribute to the capacitance. However, when either the frequency of the applied bias or the temperature changes so that the level cannot respond, there will be a change in the capacitance. At intermediate temperatures, the charge, $\delta\rho$, will lag the voltage, δV, and hence will produce a real component (i.e., conductance) to the admittance. For the situation where the frequency is fixed and the temperature is varied through the range where the level makes the transition, the capacitive component of the admittance will change monotonically from one value to another. Simultaneously, the conductance goes through a peak. A peak in the conductance will occur when $\omega\tau_k = 1$, where τ_k is the time constant for the k^{th} level. Thus, if G, the conductance, is measured as a function of temperature, at fixed frequency, a peak will be observed each time an $\omega\tau_k = 1$ condition is met.

We have measured G/ω as a function of temperature for several Schottky diodes formed on BSG GaP substrates. The results of one of these experiments are shown in Figure 49. Note that, for higher frequencies, the peak occurs at higher temperatures.

The second technique used to study defect levels in GaP is the double-source photocapacitance method. This technique has recently been discussed by White, Dean and Porteous[6]. The Schottky

[5] D.L. Lossee, J. Appl. Phys. 46, 2204 (1975).

[6] A.M. White, P.J. Dean and P. Porteous, J. Appl. Phys. 47 3230 (1976).

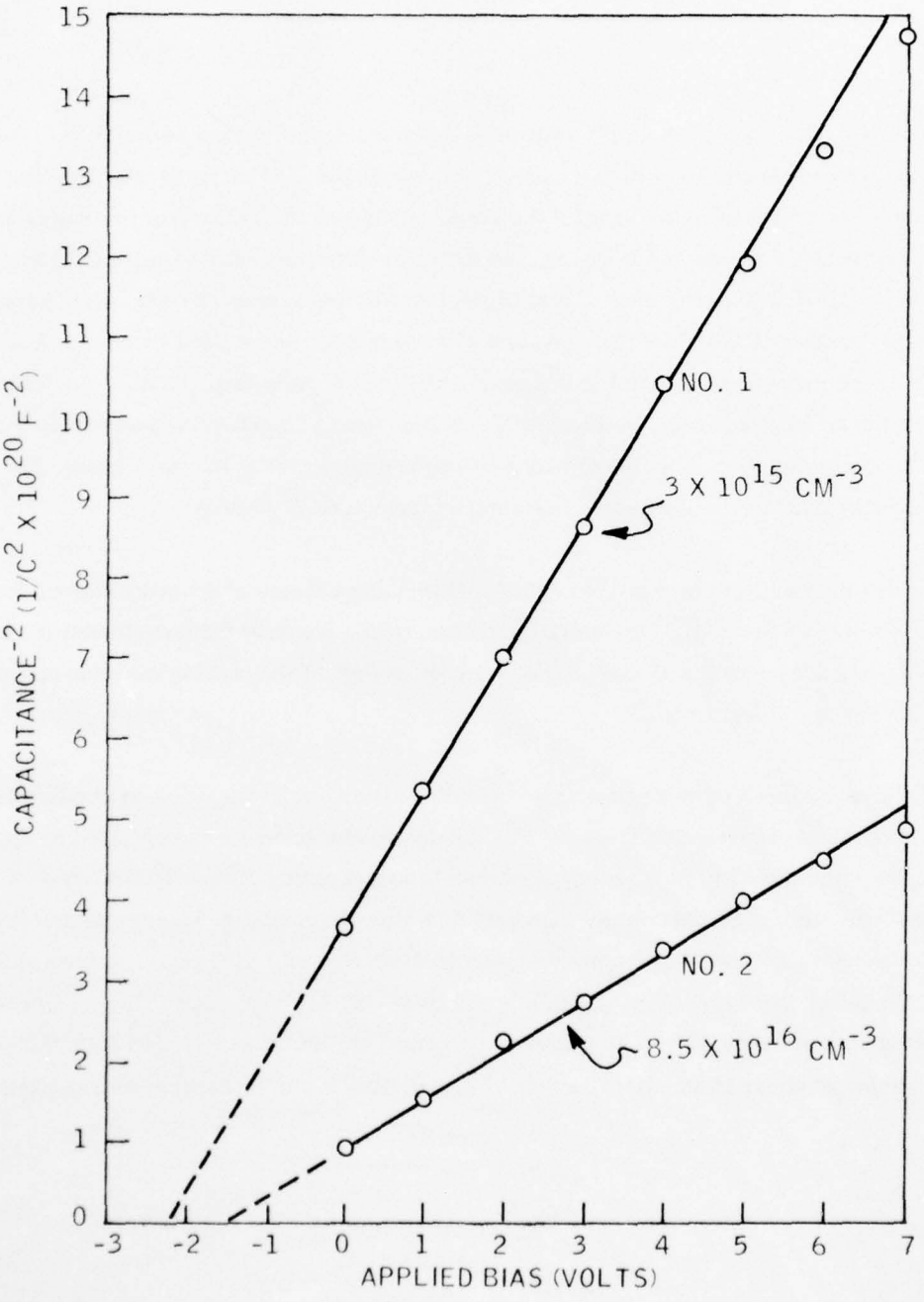


Figure 48. Inverse capacitance squared vs applied bias for two Au/GaP Schottky barriers on LPE-25-129 (diodes 1 and 2 are 15 μm and 50 μm from the growth interface, respectively).

barriers diodes are fabricated on the GaP substrate as described above by evaporating gold to form a thin semitransparent contact. A constant source of priming radiation of energy greater than the bandgap energy is maintained on the sample. A second, variable energy source (the probing radiation) is simultaneously directed on the sample, and the diode capacitance is measured as the energy of this source is varied. The steady level of priming radiation serves to create a steady-state population of electrons in traps above the Fermi level and of holes in traps below the Fermi level. Above the appropriate photon energy thresholds, the probe radiation upsets these populations by transfer of carriers to the nearest band edge. In the depletion region, these carriers are swept away by the field, and the charge distribution is altered with a corresponding change in the capacitance. The capacitance can be increased or decreased depending on the nature of the trap.

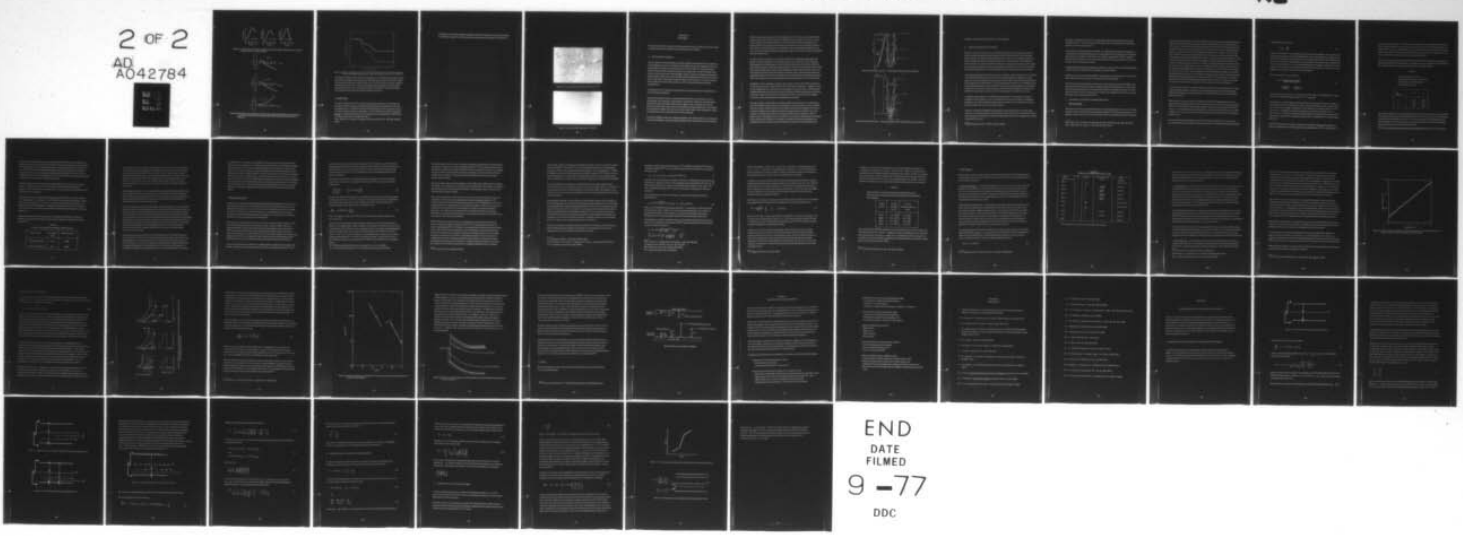
Figure 50 shows the result of our measurement of change in capacitance of Schottky barriers formed on a BSG substrate as a function of the probing radiation energy for three different measuring frequencies. The dependence of the photocapacitance on the energy of the probing radiation can give information about the defect levels.

Figure 51[a] shows the result of photocapacitance experiments on one of the Schottky diodes whose C-V characteristic was displayed in Figure 48[(bb)]. The dotted characteristic was obtained by first illuminating the diode cooled to 77 K with greater than band gap energy. This radiation upsets the equilibrium distribution of carriers on the energy levels within the band gap. This radiation is then turned off. Because of the low temperature, the time to thermalize all of the centers is long, and after about 15 minutes, the change in occupation of the levels changes very slowly. Then the probe radiation is turned on and after a 10 minute equilibration period, the energy is increased from 0.39 to 1.5 eV in a period of about 15 minutes. There is a clear decrease in the capacitance near 0.5 and 0.7 eV.

The experiments resulting in the data of Figure 51 were funded by Honeywell.

AD-A042 784 HONEYWELL CORPORATE RESEARCH CENTER BLOOMINGTON MINN F/G 20/3
ADVANCED DEVELOPMENT ON GALLIUM PHOSPHIDE MATERIALS FOR SATELLI--ETC(U)
APR 77 P E PETERSEN, R G SCHULZE, M W SCOTT F33615-75-C-5244
UNCLASSIFIED HR-47108 AFML-TR-77-37 NL

2 OF 2
AD
A042784



END
DATE
FILMED
9 -77
DDC

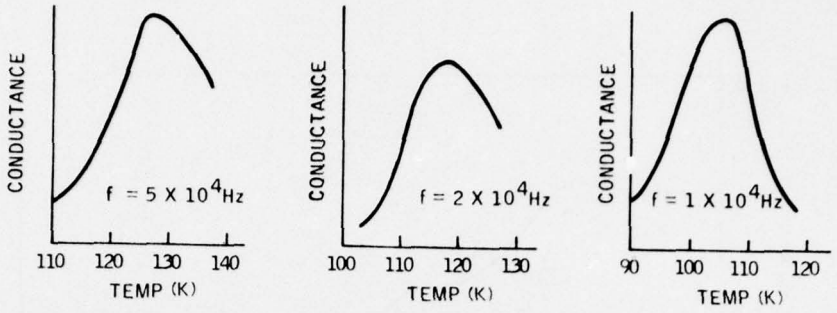


Figure 49. Conductance as a function of temperature at three different frequencies for a Au/GaP Schottky barrier on a BSG substrate.

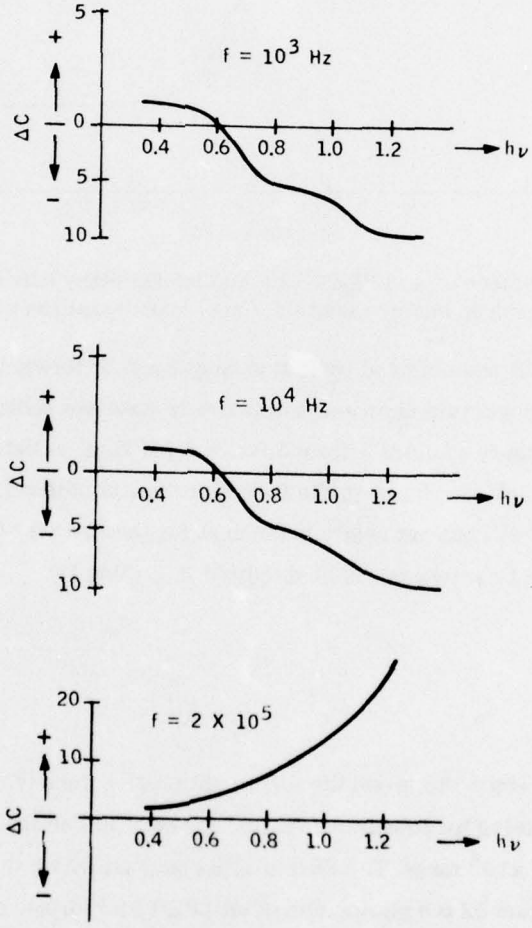


Figure 50. Dependence of the capacitance on the energy of the probe radiation at three frequencies in a Au/GaP Schottky barrier (the sample is simultaneously illuminated with 2.8 eV radiation).

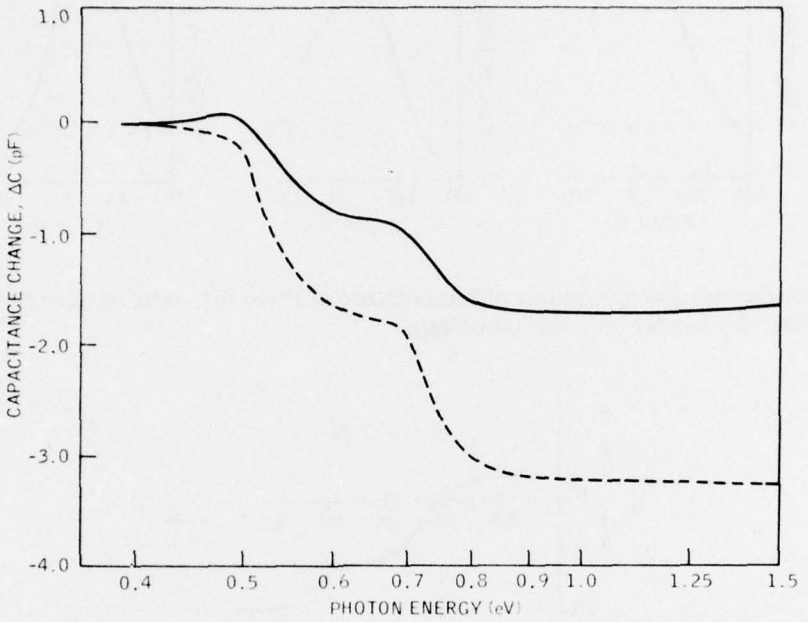


Figure 51. Change in capacitance of an LPE-25-129 Au/GaP Schottky barrier due to photoexcitation with less than bandgap energy radiation. Carrier concentration of the GaP= 3 x 10^{15} cm^{-3}.

The solid curve in Figure 50 was obtained by first passing 1 mA of forward current through the diode. Then 0.39 eV illumination was turned on and a near steady-state was achieved. The 0.39 eV illumination increased the capacitance of diode 1 from 3.0 to 4.5 pf. Then, as before, the probe energy was increased from 0.39 to 1.5 eV. As shown in the figure for these conditions, the capacitance still decreases near 0.5 and 0.7 eV, but not nearly as much as for the first set of conditions described above. The implications of thise results will be discussed in Section IV.

5. Etch Pit Density

We used the modified RC etch[7] to reveal the surface dislocation density in the Czochralski material which we have been using for substrates. We find the etch pit density (EPD) in the Czochralski material to be in 5 - 10x10^4 range. The EPD in LPE layers grown on these substrates was in the 3 - 9x10^4 cm^{-2} range. Figure 52 is a photograph of an LPE-17-93 surface in which the dislocations have been revealed with the modified RC etch. It appears from this data and that of others[8] that

[7] T. Iizuka, J. Electrochem. Soc. 118, 1190 (1971).

[8] W.A. Brantley, O.G. Lorimor, P.D. Dapkus, S.E. Haszko and R.H. Saul, J. Appl. Phys. 46, 2029 (1975).

dislocations in the substrate propagate through the LPE layer. Figure 53 shows the etch pit density in an SSD grown sample. The etch pit density for selected areas in this sample was $\sim 2 \times 10^3$ cm^{-2}.



Figure 52. Etch pits in GaP LPE-17-93 (EPD - 3×10^4 cm^{-2}).

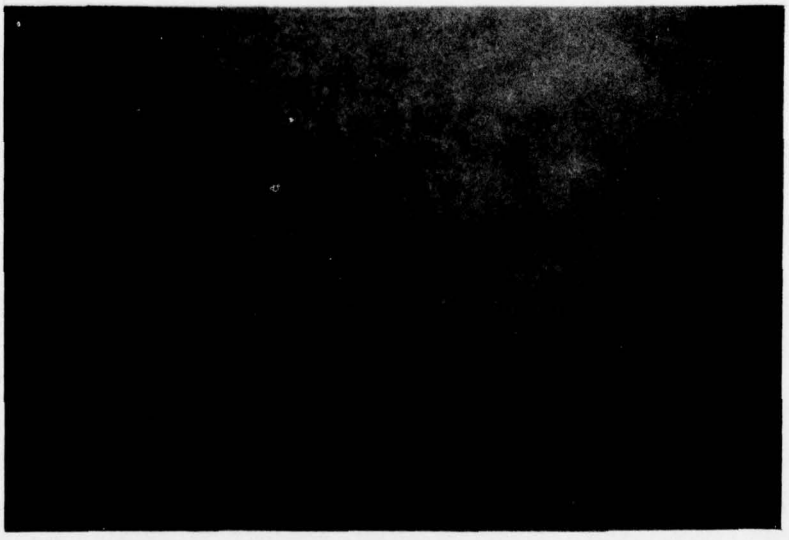


Figure 53. Etch pits in GaP SSD-3 (EPD - 10^3 cm^{-2}).

SECTION IV
DISCUSSION

This section discusses the experimental results presented in Section III. Where possible, the results are interpreted and their relevance to the program objectives is discussed.

A. BULK SOLUTION GROWTH

The two variations of the bulk growth process, BSG and SSD, were developed for the purpose (s) of providing large area GaP: Cu crystals and/or providing solution grown substrates for LPE. During the program, it became clear that LPE was the best way to grow GaP: Cu photoconductor material. Therefore, BSG Cu doping experiments were stopped after run BSG-18. Emphasis was placed on developing a process for growing large, uniform, inclusion-free, high-purity and low-dislocation-density crystals which could eventually provide substrates for LPE growth. This objective was achieved; single-crystal ingots were grown as large as 1.2 cm diameter x 1 cm long. The ingot from run SSD-3 was inclusion free and had a much lower dislocation density than typical Czochralski GaP.

An important part of the bulk growth development was the design of the growth apparatus so as to achieve single-crystal growth.

The liquid-solid interface which occurs during solidification from a melt (whether or not it is stoichiometric) will, in general, be perpendicular to the direction of heat flow. The ideal liquid-solid interface shape for the BSG system would be slightly convex. This shape promotes the growth of a single crystal for the reason that, since growth proceeds perpendicular to the interface, any crystal grain boundary that exists at the interface will be carried, as the crystals grow, toward the nearest point on the crucible wall where it will be terminated.

In trying to establish the maximum temperature gradient in the Ga-GaP solution, one would prefer to have a steep gradient in the furnace along the length of the crucible. However, the Ga metal is a

relatively good thermal conductor which is terminated on the cool end by a much poorer thermal conductor (the crucible and the quartz tube). This results in the Ga-GaP solution at the cool end of the crucible being somewhat hotter than the furnace environment directly alongside of the crucible. Heat flow thus acquires a radial component outward as well as a longitudinal component. This situation is illustrated in Figure 54. The results, in terms of crystal growth, range from a tendency to form a polycrystal rather than a single-crystal ingot, to the growth of a hollow-cone-shaped, very polycrystalline mass.

In order to obtain the preferred convex growth interface while maintaining a large temperature gradient, the growth apparatus was modified from that shown in Figure 54 to that of Figure 55. By generating the temperature gradient in the Ga solution with forced cooling of the crucible tip while using a flat furnace profile, the temperature in the Ga solution near the bottom of the crucible will actually be higher than the furnace tube temperature, which for this case is held constant. Any radial component of heat flow will therefore be inward and, when combined with the downward longitudinal component of heat flow, will produce convex isotherms. The increasingly single-crystal nature of the ingots from runs using this arrangement demonstrated that it was the correct design.

The graphite crucible is preferable to quartz. Ample evidence exists in the scientific literature that solution growth in quartz containers leads to silicon and oxygen contamination. A graphite crucible is easily configured to use a seed crystal. The seed crystal is an important asset in minimizing polycrystalline growth from the very start of growth and therefore maximizing the single-crystal volume of the ingot. Graphite also eliminates the bonding of the GaP to the crucible wall. The graphite crucible and quartz ampoule produced our largest single-crystal ingot.

The p-type behavior of early BSG runs in quartz crucibles was most likely due to contamination from the oil-diffusion vacuum pump. After switching to an evapor-ion vacuum system, run SSD-5, which used a quartz crucible, produced n-type material. We believe that persistence of p-type conductivity in GaP grown in the graphite crucible when using evapor-ion evacuation is due to the interaction of residual water vapor and/or oxygen (probably from the phosphorus) with the graphite crucible. Although the p-type conductivity is not necessarily a disadvantage if the material is to be used for LPE substrates, it can probably be eliminated by appropriate handling of the phosphorus. This may include such steps as obtaining the phosphorus in preweighed amounts

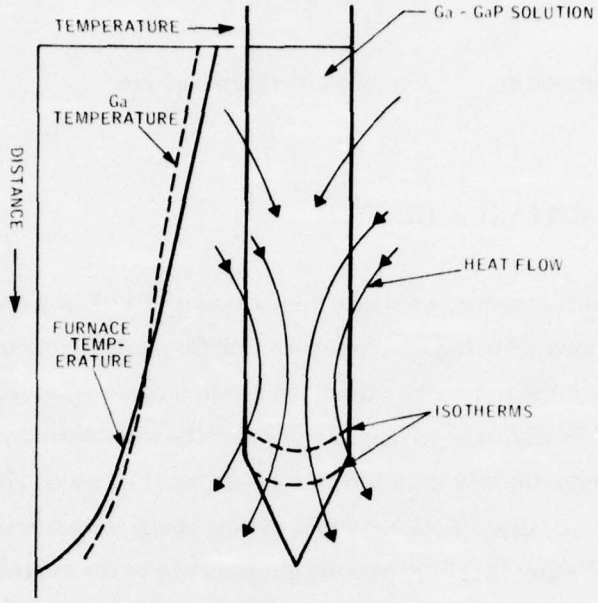


Figure 54. Bulk Solution Growth — Furnace gradient producing concave isotherms.

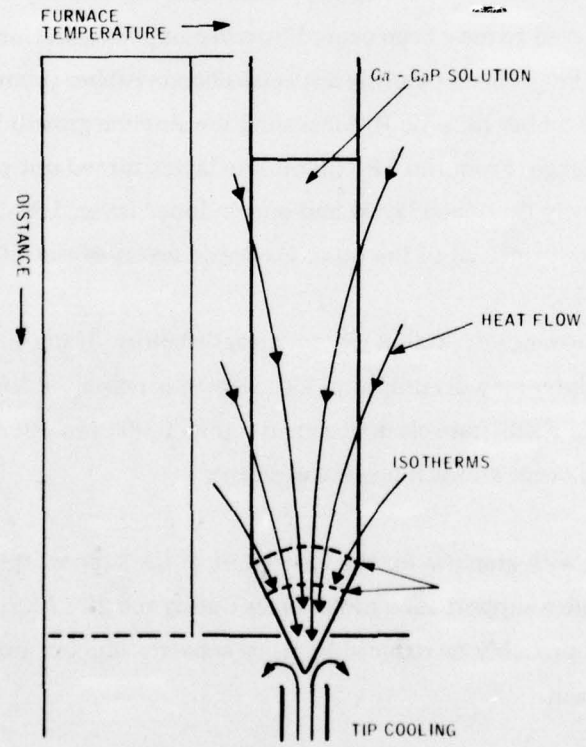


Figure 55. Bulk Solution Growth — Flat furnace profile with tip cooling producing convex isotherms.

suitable for a single growth and loading in an inert atmosphere.

B. LIQUID PHASE EPITAXIAL GROWTH

During the course of this program, we successfully developed LPE as a crystal growth technique capable of producing large-area, high-performance GaP:Cu photoconductors. The development proceeded from some initial feasibility experiments with a common source substrate apparatus to a slider technique and finally to an advanced version of the slider technique. With the advanced slider, we are able to reproducibly grow 0.6 cm^2 layers, most of which are smooth and flat enough for photoconductor fabrication. They are wiped almost completely free of Ga so that no cleaning process which might destroy the short-wave-length response of the as-grown surface is necessary.

A contamination problem which produced p-type conductivity in many of the layers in runs LPE-15, -19, -21 and -22 is believed to have been caused by a decomposing and/or leaking growth tube flange seal. We solved the problem by using a special silicone rubber primer (Dow-Corning 1200)[cc] and a two-part silicone rubber (Silastic E) for sealing the alumina growth tube to a redesigned water-cooled stainless steel flange. From run LPE-23 on, the layers turned out predictably n-type with the exception of a few heavily Cu doped layers and one undoped layer, LPE-24-118. The behavior of LPE-24-118 is anomolous since all of the other Cu-doped layers of run LPE-24 were n-type.

A substrate to slider clearance of ~0.002 was found satisfactory. If the clearance is much less, interference with the slider may occur if any ridge growth is present at the edge of the LPE layer. Although we never used a substrate clearance greater than 0.002 in., poor wiping action and even growth bin leakage can occur at much larger clearances.

Alumina is compatible with graphite for the tapered fit of the support tube into the slider base; quartz is not. The alumina support tube broke twice during the 20 LPE runs using slider mechanism 3. This breakage could probably be reduced by using separate support and cooling gas tubes, thereby reducing the load on each.

[cc]Dow-Corning Corporation, Midland, Michigan 48640.

The effect of substrate orientation was not exhaustively studied; we determined, however, that orientation errors of ~0.5 to 0.75 from the $\langle\bar{1}\bar{1}\bar{1}\rangle$ plane do not cause serious surface smoothness problems for a photoconductive device.

An appropriate operating temperature is 1050°C. It is sufficiently high so that small temperature increments give useful layer thicknesses, yet it is far enough below the melting point of GaP so that the Ga vacancy concentration is reduced by over 3 orders of magnitude [9]. Further decreases in growth temperature appear to result in reducing the amount of Cu incorporated into the crystal to the point where photosensitization ceases.

A palladium-diffused hydrogen atmosphere is preferred not only because it is a reducing atmosphere, but also because it is as high purity an atmosphere as is easily obtained.

Relatively low cool down rates were employed. The increase in cool down rate from 2.5 to 6.7°/hr. had no apparent effect on the growth. Faster growth rates may be possible.

Runs LPE-27 through LPE-29 which explored the precursor technique, but without substrate cooling, supports the importance of substrate cooling for good surface morphology in our slider system. The exact temperature difference across the growth interface with substrate cooling, as we successfully employed it, could not be measured. The cooling was accomplished with a He flow of 5 l/min. through the coaxial cooling gas-support tube.

C. ELECTRICAL AND OPTICAL PROPERTIES OF GaP

1. Photoconductivity

Discussions of our work on photoconductive effects in GaP:Cu grown from solution by the so-called random nucleation technique have been previously published [3]. This subsection discusses the most significant results of the photoconductivity experiments which were performed during this program.

---

[9] A.S. Jordan, A.R. Von Neida, R. Caruso and C.K. Kim, J. Electrochem. Soc. 121, 153 (1974).

[3] R.G. Schulze and P.E. Petersen, J. Appl. Phys. 45, 5307 (1974).

As previously discussed, there is a difference between the spectral response for samples fabricated on as-grown, solution-grown GaP:Cu surfaces and that for samples fabricated on surfaces which have been treated; i.e., lapped, polished or chemically etched. Figure 19 shows the spectral response for an as-grown surface and for a surface which had been dipped in HCl. HCl does not readily dissolve GaP, yet as can be seen, there is a marked difference between the two response curves. For both types of surfaces, there is a rather sharp edge to the low-energy photon response near the energy corresponding to the indirect bandgap in GaP ($\sim$2.24 eV). For samples on interior surfaces (i.e., those whose as-grown surface has been removed by lapping or polishing), the photosensitivity falls off for photon energies greater than about 2.8 eV, whereas for samples fabricated on as-grown surfaces, the response remains nearly flat out to 4.0 eV. The larger high-energy photon response observed on the as-grown surfaces suggests that the surface recombination rate is lower for these surfaces than it is for the surfaces which have been mechanically or chemically polished. Generally, in the random nucleation growth process, there exist relatively few as-grown surfaces which are useful for detector fabrication. If the spectral response in the region from 2.8 to 4.0 eV is important, it is desirable to have a growth process which yields large-area as-grown surfaces. LPE is, of course, such a process. In Section III we discussed the experiments on the Cu doping of GaP during LPE growth.

Growth run LPE-11 used the new slider mechanism 3 with substrate cooling. This growth run represented a significant advance, at that time, in the crystal quality and also in the photoproperties. Figures 20-23 summarize the photocharacteristics of LPE-11-69, which was one of the Cu-doped samples from this run.

Figure 20 shows that for this sample, the response has a rather soft leading edge around 2.2 eV (near the indirect band-gap energy of GaP); it reaches a peak just before the direct band-gap energy ($\sim$2.8 eV) and then falls off slowly for higher energies. The fact that the gain tails off for photon energies $>$ 2.7 eV suggests that surface recombination is affecting the response. However, the rolloff at energies $>$ 2.8 eV is not nearly as fast as in photoconductive samples fabricated on a lapped and polished surface.

The photoconductive gain, defined as the ratio of the majority carrier lifetime τ to transit time τ_d, is remarkably high in this sample. The gain is dependent on the applied voltage and the geometry

of the samples by the relation:

$$G = \frac{\tau}{\tau_d} = \frac{\mu\tau V}{\ell^2} \qquad (1)$$

where μ is the mobility, V is the applied bias, and ℓ is the contact separation. The $\mu\tau$ product is the factor which is important from a materials standpoint. For the sample described in Figure 20, $\mu\tau \sim 10^{-2}$. If we assume the mobility is 100 cm^2/V-sec, we find that the majority carrier lifetime is 10^{-4} sec. This is a long lifetime, indicating that the Cu doping has in fact acted to sensitize the photoconductor. The response time is, of course, ultimately limited by the majority carrier lifetime, so since response times $\sim$ milliseconds are desirable, the lifetime should be $\lesssim 10^{-4}$ sec. Hence, from a device standpoint, the majority carrier lifetime was nearly optimal.

The noise equivalent power is defined by:

$$NEP = \frac{\text{Power incident on sample}}{\text{Signal-to-noise ratio}} \qquad (2)$$

$$= \frac{(F)\,(h\nu)\,A}{eGF \cdot A/i_n} \qquad = \left(\frac{h\nu}{eG}\right)\left(i_n\right)$$

The noise current for this sample at 3 V bias and at 100 Hz was 2×10^{-10} amps/$\sqrt{Hz}$. For a gain of 2.5×10^4 at 4600 Å, this gives a NEP $\sim 2 \times 10^{-14}$ watts/$\sqrt{Hz}$.

The dependence of the photosignal on the incident photon flux intensity was shown in Figure 21 in the range from $10^{11} \rightarrow 10^{15}$ photons/cm^2-sec. The linear dependence which is observed at the lower flux intensities is highly desirable from a device standpoint. In the high resistivity ($>10^8$ Ω-cm) GaP:Cu, we usually find a superlinear dependence of the signal on the photon flux; i.e., $I_s \sim F^n$ where $n > 1$. However, in the low resistivity samples, we usually observe the linear dependence shown in Figure 21. We will discuss this aspect of the I-F characteristic in more detail later in this section.

Near 10^{13} photons/cm^2-sec, as shown in Figure 21, the signal-flux characteristic changes from a linear to a sublinear behavior, with the signal varying approximately as $F^{1/2}$. In the literature on

sensitized photoconductivity, a $F^{1/2}$ dependence is usually attributed to the presence of a distribution in energy of majority carrier traps below the conduction band. The physical picture proposed by Rose [10] to account for sublinear behavior is that as the light intensity is increased, the electron demarcation level moves toward the conduction band and electron traps are converted to recombination centers with a resulting decrease in the majority carrier lifetime.

The spatial uniformity of the photosignal of three samples from LPE-11-69 is shown in Figure 23. This represents a substantial improvement in uniformity over that of samples from the earlier growth runs. As shown in Table 7, the standard deviation in the photosignal was ~ 0.1.

TABLE 7

AVERAGE VALUE, $\bar{X}$, AND
STANDARD DEVIATION, S, FOR THE
PHOTOSIGNAL IN THREE GaP:Cu
PHOTOCONDUCTORS.

Slit Number	$\bar{X}$	S
1	0.90	0.082
2	0.83	0.11
3	0.97	0.061

The frequency dependence of the photosignal for a LPE GaP:Cu photoconductor is shown in Figure 22. Also shown are the characteristics for response times of 10^{-4} sec and 5×10^{-4} sec. The majority carrier lifetime for this sample was 10^{-4} sec. It is clear that the majority carrier lifetime does not limit the response time. The longer response time is due to the presence of majority carrier traps, which to date have not been fully characterized in GaP.

[10] A. Rose, Concepts in Photoconductivity and Allied Problems, Interscience, New York (1963).

From a growth morphology viewpoint, runs LPE-23 and LPE-24 were the most desirable. The photocharacteristics of samples from run LPE-23 were especially noteworthy. As shown in Figure 24, this sample exhibits a very broad spectral response. The measured gain at 5 eV (0.25 μm) is $\sim 4 \times 10^4$. This is by far the broadest spectral response which we have observed on GaP photoconductive samples. In previous samples, the photoresponse extended only to about 4 eV. We interpret this increased short wavelength response to an improvement of the as-grown surface with a resulting decrease in the surface recombination velocity.

The photosignal/photon flux characteristic (see Figure 25) shows the same linear to sublinear transition for LPE-23-117 which we observed in LPE-11-69. This sample had a rather low resistance ($\sim$100 Ω), however, it was also quite thin (<5 μm), so there is a shunt resistance across the sample due to the substrate.

The field at which these measurements were taken was about 10^3 V/cm. At photon energies of 3 eV, this translates to a $\mu\tau$ product of 3×10^{-2} cm^2/V. If we use 100 for the mobility, we find τ, the majority carrier lifetime, is $\sim 3 \times 10^{-4}$ sec. Figure 26 shows the frequency response for this sample, along with the characteristic for a single time constant of 6×10^{-4} sec. The response is close to the limit set by the majority carrier lifetime, which for a photoconductor, is a very short response time.

The spatial uniformity of the photoresponse for two samples from LPE-23-117 as shown in Figure 27 is fairly good. Table 8 shows that for these two samples, the standard deviation was less than 0.09.

TABLE 8.

SPATIAL UNIFORMITY OF SAMPLES FROM LPE-23-117

Sample Number	Slit Length (mm)	Standard Deviation
LPE-23-117 Number 1	3.15	0.085
LPE-23-117 Number 2	2.89	0.068

As discussed in Section III, the surface morphology of the last few growth runs did not permit us to place contacts in the slit configuration on the sample surface. We were, however, able to make ohmic contacts by alloying small In:1%Te dots on the surface. On these last growth runs we observed the largest photoconductive gains measured during the program. As shown in Figure 28, photoconductive gains greater than 10^5 were attained. For this sample, this translates to a $\mu\tau$ product of 4 cm^2/V, which, in turn, gives a majority carrier lifetime of 0.04 sec. Hence, this sample necessarily has a long response time. These results show that very-high-gain LPE GaP:Cu can be grown.

Sensitized photoconductivity can be either thermally or optically quenched. Figure 30 shows that up to temperatures of 90°C, the photosensitivity of LPE-23-117 was not reduced. The noise at 90°C, however, was substantially larger than it was at room temperature. The photoconductivity is, however, quenched by optical radiation whose energy is greater than the energy depth of the sensitizing center, but less than the band gap energy.

The percent quenching as a function of the energy of the quenching radiation is shown in Figure 31. When the energy of the quenching radiation equals or exceeds the difference in energy between the valence band and the sensitizing centers (deep acceptors), holes can be excited from these centers back to the valence band. The recombination traffic through the long electron lifetime sensitizing centers has effectively been blocked. The recombination then proceeds through the fast recombination centers, which have a much larger capture cross-section for electrons. The result is a shorter electron lifetime, and the photoresponse is correspondingly decreased. The photoresponse can be quenched for all photon energies larger than the energy difference between the valence band and the sensitizing center. The data in Figure 31 suggest that the Cu energy level lies approximately 0.65 eV above the valence band.

The photosignal versus photon flux intensity characteristic for three Cu doped LPE samples was shown in Figures 21, 25 and 29. These were all rather low resistivity samples. Figure 32 shows the photosignal/photon flux intensity characteristic for a high-resistivity LPE GaP:Cu sample. Note that for this sample, the characteristic is superlinear over many orders of magnitude and that there is a suggested linear dependence at the highest photon flux. We have observed this behavior in previous GaP:Cu samples. The superlinear behavior can occur when the light intensity is such that

the demarcation level is being moved through the sensitizing centers and converting them from electron traps. (See Appendix A for a discussion of photoconductivity in wide band gap materials.) After the sensitization is complete, the signal should again vary linearly with the light intensity. There are two possible explanations for the linear behavior seen in the photocurrent/photon flux characteristic for the low resistivity samples. The first is that because the samples are low resistivity, the carrier concentration is high enough so that the demarcation level lies below the Cu acceptor. The second is that, in the dark, the demarcation level lies above the acceptor, but that the transition occurs at radiation intensities below those at which our measurements were made. We believe that these data, especially the optical quenching and the superlinear dependence in the photocurrent photon flux characteristic, suggest that sensitized photoconductivity is the photomechanism in GaP:Cu.

2. Transport Measurements

A primary means of identifying and quantitatively measuring the impurities in a semiconductor is by Hall effect measurements. As discussed in Section III, we have taken Hall data on all of the BSG and SSD material and on one of the LPE layers. From the Hall data, we have (1) identified the principal impurities in the material we have grown, (2) identified the primary scattering mechanisms and (3) determined the degree of compensation (i.e., N_d and N_a) in some material. We will now discuss our interpretation of the Hall results.

The Hall data are summarized in Tables 5 and 6. As shown in the tables (see also Tables 1 and 2), all of the unintentionally doped runs were p-type with the exception of SSD-5. (The use of evapor-ion ampoule evacuation and a quartz crucible which resulted in n-type conductivity in SSD-5 was discussed earlier in this section.) The use of GaP:S starting material produced all of the other instances of n-type conductivity. The acceptor activation energy for all of these p-type samples was near 0.040 eV (see Figure 38). These data, along with the optical absorption data discussed in the next section, establish that carbon is the acceptor impurity in this material.

In some of the growth runs (see Table 3), the starting material was sulfur-doped Czochralski. The samples so doped were low resistivity n-type with a carrier concentration in the mid 10^{17} cm^{-3}

range. The sulfur donor activation energy, determined from the Hall data, was ~0.095 eV. The optical absorption data showed that these samples were carbon doped to a greater extent than the starting material. Hence, we concluded that carbon was inadvertently being introduced during the growth process. In Section IV-A, we discussed our current understanding of the source of carbon in GaP growth.

The Hall data were analyzed in a straightforward manner according to the statistics for single donor and acceptor levels and nondegenerate carrier densities[11]. For a p-type sample, these conditions give:

$$\frac{(p)\,(p+N_d)}{(N_a-N_d-p)} = \frac{N'_v}{g}\,T^{3/2}\exp\left(-\frac{E_a}{kT}\right) \tag{3}$$

where p is the temperature-dependent hole concentration, N_a and N_d are the acceptor and donor concentrations respectively, $N'_v T^{3/2}$ is the density of states in the valence band, g is a degeneracy factor which depends on the nature of the impurity state and the band edge and E_a is the acceptor activation energy. In the "freeze-out" region ($p << N_d$):

$$\frac{p}{T^{3/2}} \propto (\text{CONST})\exp\left(-\frac{E_a}{kT}\right) \tag{4}$$

Hence, the straight-line region of a $p/T^{3/2}$ versus T^{-1} plot gives the activation energy, E_a, as seen in Figure 38.

N_d and N_a can be obtained by fitting the Hall data to Equation 3 over the whole temperature range. We use a similar approach, which is adequate for our purpose. The ratio $N_d/(N_a - N_d)$ can be computed directly from Equation 3 if E_a and (N'_v/g) are known. The analysis preceeding Equation 4 gives the activation energy. The work of van der Does de Bye and Peters[12] gives $4.2 \times 10^{14} \leq N'_v/g \leq 1.1 \times 10^{15}$. $N_a - N_d$ can be obtained by extrapolating the Hall coefficient versus reciprocal temperature characteristic to zero. Hence, N_a and N_d are obtained to within about a factor of two. The values of N_d and N_a, so calculated, for two BSG runs and four SSD runs are tabulated in Table 6.

11 J. S. Blakemore, Semiconductor Statistics, Pergamon Press, New York (1962).

12 J. A. W. van der Does de Bye and R. C. Peters, Phillips Res. Repts. 24, 210 (1969).

One of the expected benefits of these two growth processes is an improvement in the uniformity of the material. In Figure 34, the carrier concentration times $T^{-3/2}$ versus reciprocal temperature was plotted for two samples from growth run BSG-10. The fact that the data from each of these samples are equal to within experimental error demonstrates uniformity in majority carrier concentration for this growth run. Hence, we have demonstrated that the BSG process can be used to grow spatially uniform material.

The photoconductive gain is linearly dependent on the mobility of the majority carrier. In addition, the mobility can give information on the quality of the material. Hence, the mobility is an important material parameter. We now proceed with a discussion of the mobility in both n- and p-type GaP which was grown during this program.

The temperature dependence of the electron mobility for a typical n-type BSG sample was shown in Figure 35. Note that near room temperature, the mobility varies approximately as $T^{-3/2}$. combined intervalley and acoustic mode scattering result in near $T^{-3/2}$ dependence for the electron mobility. However, the theory predicts a room temperature mobility ~200 cm^2/V-sec when these mechanisms limit the mobility. The room temperature mobility for the sample described in Figure 35 is ~110 cm^2/V-sec. The reason for the room temperature mobility being less than 200 cm^2/V-sec is attributed by some authors to ionized impurity scattering. We now briefly discuss the mobility in n-GaP near room temperature.

Rode[13] has shown theoretically that at room temperature, ionized impurity scattering can lower the mobility for carrier concentrations $> 10^{17}$ cm^{-3} in uncompensated material and for carrier concentrations $\gtrsim 10^{15}$ cm^{-3} in heavily compensated material. He also shows that experiment does not agree with the theory, presumably due to the breakdown of the spherical band approximation in the calculated ionized impurity scattering. Our results generally show that the higher the carrier concentration, the lower the room temperature mobility, but there are exceptions. In Figure 36, we show the temperature dependence of the mobility for a rather heavily doped uncompensated n-type sample, which should be compared with the data of Figure 35. Note that the mobility of the more heavily doped sample is considerably higher than that for the lighter

[13] D. L. Rode, Phys. Stat. Sol. 53, 245 (1972).

doped samples. Other investigators have found similar discrepancies. See, for example, the work of Hara and Akasaki[14] and Craford[15], et.al. The data suggest that another, yet undetermined mechanism is influencing the mobility near room temperature. At lower temperatures (< 100 K), the mobility for the n-type BSG-10 sample shown in Figure 35 varies as $T^{-1/2}$. We have frequently observed this behavior in Cu doped GaP. Our preliminary assessment is that the mobility in this region is limited by the scattering of electrons by space charge regions, as discussed by Weisberg[16].

We now proceed with an interpretation of the Hall data for p-type material. Figure 38 plots $p/T^{3/2}$ versus $10^3/T$ for four SSD p-type samples. Note the linear region, which is clear evidence of carrier freezeout, thus permitting determination of the activation energy. The leveling out at low temperature occurs when impurity hopping begins to influence the charge transport, and the simple theory breaks down.

The temperature dependence of the resistivity for these four BSG samples is shown in Figure 40. Near room temperature, the resistivity decreases with decreasing temperature because the mobility is increasing faster than carriers are being emptied from the valence band. In the carrier freeze-out regime, the decrease in carrier concentration with temperature is the dominant influence and the resistivity increases sharply with decreasing temperature. At the low temperatures, the carrier concentration becomes so low that impurity conduction becomes important. In this region, the resistivity has a much weaker temperature dependence. Impurity conduction occurs when holes hop from occupied to unoccupied acceptors with the aid of phonons.

The three most prevalent scattering mechanisms which limit the mobility in a semiconductor are lattice scattering, impurity scattering, and scattering due to inhomogeneities or local space charge regions. We now consider these mechanisms in p-type GaP.

---

14 T. Hara and I. Akasaki, J. Appl. Phys. 39, 285 (1968).

15 M. G. Craford, W. O. Groves, A. H. Herzog and D. E. Hill, J. Appl. Phys. 42, 2751 (1971).

16 L. R. Weisberg, J. Appl. Phys. 5, 1817 (1962).

We will first consider lattice scattering. Casey, et.al.[17] evaluated the familiar $T^{-3/2}$ expression of Bardeen and Shockley[18] for the mobility for scattering by acoustic phonons and found the following for GaP.

$$\mu_{AC} = 5.6 \times 10^7/(m^*/m_o)^{5/2} E_1^{2} T^{3/2} \text{ cm}^2/\text{V-sec} \tag{5}$$

Here, E_1 is the volume deformation potential in eV and m* the effective mass. For a deformation potential of 1.0, Equation 5 yields a room temperature mobility greater than 10^4 cm^2/V-sec. The data of Figures 37 and 41 show that at room temperature, the mobility in p-type GaP is ~100 with a temperature dependence $\propto T^{-2.4}$. Hence, acoustic phonon scattering is not a limiting mechanism.

The expression for the mobility when limited by optical phonon scattering as derived by Ehrenreich[19] is:

$$\mu_{op} = 2.4 T^{1/2} \left(\frac{m_o}{m^*}\right)^{3/2} \left[\exp\left(\frac{\theta}{T}\right) - 1\right] F\left(\frac{\theta}{T}\right) \text{ cm}^2/\text{V-sec} \tag{6}$$

where ω_l is the longitudinal optical phonon frequency, $\theta = h\omega_l/k$ and F is a function obtained from Ehrenreich's paper. In Figure 37, we plot μ_{op} according to Equation 6 as a function of temperature. While the fit of this expression is not perfect, it appears that optical phonon scattering plays a role in determining the mobility for temperatures greater than 150 K.

Ionized impurity scattering is frequently found to be the limiting scattering mechanism in semiconductors at moderately low temperatures. Blatt[20] expresses the mobility when determined by ionized impurity scattering as:

$$\mu_I = 3.3 \times 10^{15} \frac{T^{3/2}}{N_I} \left(\frac{m_o}{m^*}\right)^{1/2} \left(\frac{k}{\epsilon_o}\right)^{2} \times \left\{ \ln\left[1.2 \times 10^{14} \frac{T^2}{n'} \left(\frac{k}{\epsilon_o}\right)\left(\frac{m^*}{m_o}\right) - 1\right]\right\}^{-1} \tag{7}$$

---

[17] H. C. Casey Jr., F. Ermanis and K. B. Wolfstirn, J. Appl. Phys. 40, 2945

[18] J. Bardeen and W. Shockley, Phys. Rev. 80, 72 (1950).

[19] H. Ehrenreich, J. Phys. Chem. Solids 8, 130 (1959).

[20] F. J. Blatt, Solid State Phys. 4, 344 (1957).

where k is the dielectric constant, $N_I = p + 2N_d$ is the concentration of ionized impurities and $n' = p + (p + N_d)\,[\,1 - (p+N_d)/N_a\,]$. At temperatures low enough that $p \ll N_d$, $T^{3/2}$ dominates the temperature dependence of this expression. Note that μ_I is strongly dependent on the density of the compensating donors, which, of course, is determined from the Hall data.

In Figure 37, we plot the calculated values of μ_I for two samples, BSG-19 and BSG-21, using the experimentally determined values tabulated in Table 6 and an effective mass ratio of 0.4. The hole effective mass of GaP is generally believed to be ~0.5. However, our method of determining N_d and N_a could result in an error in these quantities which would, of course, alter μ_I to some degree. Note from Table 6 that as N_d decreases, μ(77 K) generally increases as expected if ionized impurity scattering is a dominant mechanism.

Neutral impurity scattering is another mechanism which can limit the mobility at low temperatures. The expression derived by Erginsoy[21] for mobility when limited by this mechanism is:

$$\mu_N = \frac{1.4\times10^{22}}{N_N}\ \frac{m^*}{m_o}\ \frac{\epsilon_o}{k}\quad (cm^2/V\text{-}sec) \tag{8}$$

where $N_N = (N_a - N_d) - p$ is the neutral impurity concentration. μ_N, according to Equation 8, has its lowest value at low temperatures where $p < N_a - N_d$. For these conditions, $\mu_N \approx$ CONST $\approx 7 \times 10^{20}/(N_a - N_d)$. Only for rather heavily doped samples ($\gtrsim 10^{18}$ cm^{-3}) will neutral impurity scattering be significant in determining the mobility.

In Figure 41, we show the temperature dependence of the mobility for the same four SSD samples which we discussed earlier. The characteristic shape is the same as that for the BSG samples discussed above. However, for these samples, we have better low temperature data and we see that for temperatures below 30 K, the mobility drops precipitously with decreasing temperature. In SSD-4, the mobility dropped to a value less than unity. These low values of the mobility are characteristic of conduction by the phonon-assisted hopping of holes from neutral to ionized acceptors.

---

21 C. Erginsoy, Phys. Rev. 79, 1013 (1950).

In Figure 41, we also plot the calculated values of μ_I for four different donor densities. In calculating these expressions, we used $m_h^* = 0.4$ and $N_v'/g = 4.2 \times 10^{14}$. In order to obtain a reasonable fit to the experimental data, we adjusted the donor density. In Table 9, we compare the value of the donor density obtained from the Hall measurement to the value obtained by fitting the theoretical expression for μ_I to the experimental data for the mobility. The lack of agreement is probably due to our approximate method for determining N_d for the Hall data.

TABLE 9

COMPARISON OF THE DONOR DENSITY DETERMINED FROM THE HALL DATA AND FROM THE IONIZED IMPURITY EXPRESSION FOR MOBILITY.

Sample Number	N_d from Hall Data (cm^{-3})	N_d from Mobility Expression (cm^{-3})
SSD-1	2.8×10^{16}	3.1×10^{16}
SSD-2	2.6×10^{16}	4.0×10^{16}
SSD-3	3.8×10^{16}	7.0×10^{16}
SSD-4	2.4×10^{16}	1.6×10^{16}

Wiley and Di Domenico[22] have discussed the lattice mobility of holes in the III-V compounds. They claim that in the III-V materials, scattering by nonpolar optical phonons is more important than the scattering by polar modes. In Figure 41, we compare their theoretical expression for combined acoustic and polar mode scattering with the experimental data. The agreement is fairly good for temperatures greater than 120 K.

---

22 J. D. Wiley and M. DiDomenico, Phys. Rev. B2, 427 (1970).

3. IR Spectroscopy

IR spectroscopy on GaP crystals has turned out to be especially valuable for the characterization of carbon in GaP. In this section, we will discuss the results of the three types of measurements which were presented in Section III.

a. Local Mode Absorption -- Normally, IR absorption in an ionic crystal is at a maximum when the frequency of the IR radiation is in resonance with the motion of the atoms in the crystal. In the case of GaP, this corresponds to the condition when neighboring Ga and P atoms are in motion toward each other giving rise to an electric dipole which can strongly interact with the radiation at the same frequency. This occurs at an optical frequency of 360 cm^{-1} in GaP and gives rise to the reststrahlen band in this frequency range.

Introducing a point defect into an otherwise perfect crystal modifies the modes of vibration of the crystal. Usually, the introduction of a lighter atom into the lattice, such as C on a P site, causes new modes of vibration at higher frequencies than occur in the perfect crystal. These new modes occur only at the defect center and are characteristic of the mass and binding of this new atom in the crystal and therefore give a measure of the density of these defects. The introduction of a heavier atom into the lattice, such as S or Se on a P site, usually introduces a lower frequency mode of vibration which is indistinguishable from the lattice itself. As a result, this technique is applicable to the lighter atoms which can be introduced into a crystal.

From the absorption spectrum shown in Figure 44, it is clear that carbon is present in the crystals being measured. The question is, can the concentration be determined from these measurements? Thompson and Newman[23] have correlated the absorption coefficient of this line with the carbon concentration and have arrived at an order-of-magnitude estimate:

$$[C]/\alpha = 3 \times 10^{16}/cm^3 \qquad (9)$$

---

23 F. Thompson and R. C. Newman, J. Phys. C., S.S.Phys. 4, 3249 (1971).

TABLE 10.
SUMMARY OF IMPURITIES FOUND IN GaP

Crystal	Type	Impurities	Concentration (cm^{-3})	Method
General Electric (GE)	n	S	$7x10^{17}$	Absorbance
BSG-4	p	C Si(p)?		Photoconductivity
BSG-8	n	C S	~ $2.5x10^{16}$ $4x10^{17}$	Absorbance
BSG-10	n	C S	~ $1x10^{17}$ > $2x10^{17}$	Absorbance
BSG-11	n	C S	~ $5x10^{16}$ $2.5x10^{17}$	Absorbance
BSG-12	n	C	~ $1x10^{17}$ > $3x10^{17}$	Absorbance
AD-9*	p	Si(?) Cu		Photoconductivity
AD-20	p	C Si (?) Cu		Photoconductivity
AD-26	?	C	~ $5x10^{16}$	Absorbance
AD-27	p	C	~ $2.5x10^{16}$	Absorbance
SSD-3	p	C	?	Absorbance

* The crystals labeled AD were grown from solution during a previous program.

with a possible error of about a factor of 3. A summary of the carbon concentrations observed in a number of crystals is shown in Table 10. Crystals BSG-8, -10, -11 and -12 in addition to crystals AD-26 and AD-27 all have carbon concentrations about mid $10^{16}/cm^3$, as determined from measurements of the local mode absorbance.

b. Excitation Spectra – The introduction of impurity atoms into semiconductors is known to create energy levels in the forbidden energy gap which are associated with the impurities. Electronic transitions can occur from the ground state of the impurity to the various excited state levels associated with the impurity, giving rise to a sharp line absorption spectrum. These transitions are well defined in energy and are characteristic of a particular impurity in a semiconductor. The absorption spectrum is then an unambiguous fingerprint of the particular impurity. This fact has been used extensively to identify impurities in Si and Ge, and we have used this procedure successfully to identify shallow donors in GaP[24].

The infrared absorption spectrum of carbon has not been previously published; in fact, only the spectrum of Cd in GaP has been reported[25]. From luminescence experiments in carbon-doped GaP[26], the position of a number of excited states have been determined and agree with our measurements to within 2 cm^{-1}. The line at 272 has been tentatively identified as a $1s_{3/2}$ transition, and the line at 297 has been labeled as a $1s_{3/2}$ - $2p_{5/2}$ transition.

These measurements have been made only in sample SSD-3, but have shown that this technique is a feasible means of identifying carbon in p-type GaP. In addition, by correlating the absorption intensity of these lines with electrical measurements, the optical measurements can be made quantitative as well as unambiguous. The results of these measurements are also listed in Table 10.

c. Photoconductivity – The oscillatory behavior of the photoconductivity shown in Figure 45 results from the interaction of the optically excited carriers with the longitudinal optical (LO) phonons. The occurrence of these dips in the photoconductivity can be understood as follows.

---

24 W. Scott and J. R. Onffroy, Phys. Rev. 13, 1664 (1976).

25 W. Berndt, A. A. Kopylov and A. N. Pikhtin, JETP Lett 22, 284 (1975).

26 R. A. Street and W. Senske, Phys. Rev. Lett 37, 1292 (1976).

The onset of extrinsic photoconductivity at low temperatures occurs when the photon energy equals the ionization energy, E_i, of the impurity. As the photon energy increases beyond the ionization energy, the photocurrent per excited carrier generally increases. This is due to the increased lifetime of the optically excited carriers since their probability of capture by the ionized centers decreases as the kinetic energy of the carriers increases. Stocker, et.al.[27] have shown that when the energy of the carriers injected into the band satisfies the condition $E(n) = E_i + n\hbar\omega_{LO}$, where E(n) is the energy of the carrier, then the injected carriers can decay rapidly to the bottom of the band, emitting phonons of energy $\hbar\omega_{LO}$. This results in a decreased average lifetime for the carriers at these injection energies and results in dips in the photoconductivity spectrum.

The ionization energy of the impurity can be obtained from the photoconductivity spectrum using the above expression for the energies of the minima. Plotting the energy of the minimum versus the minimum number, as shown in Figure 56, we see forms a straight line. The slope of the line is about 400 cm^{-1}, corresponding to the LO phonon frequency in GaP, and the intercept gives an ionization energy of about 400 cm^{-1} (50 meV). The fact that E_i and $\hbar\omega_{LO}$ are approximately the same is purely coincidental. The ionization energy of carbon is reported to be 48 meV, so this is consistent with the 50 meV required to give the observed oscillations in the photoconductivity.

Sample BSG-4, listed in Table 10, contained carbon as an impurity as identified by this technique. Since photoconductivity measurements are not quantitative, the carbon concentration could not be determined. The presence of carbon was unambiguously verified in this crystal.

In conclusion, three methods involving infrared spectroscopy were developed to identify the presence of carbon in GaP. The techniques rely on (1) optical absorption due to lattice local mode lines introduced by the carbon, (2) optical absorption due to electronic transitions within the carbon energy levels and (3) photoconductivity due to the excitation of the carbon impurity centers.

With these three techniques, we have been able to identify carbon as an impurity in both n-type and p-type GaP. These results are summarized in Table 10.

---

[27] H. J. Stocker, H. Levinstein and C. R. Stennard, Phys. Rev. 150, 613 (1966).

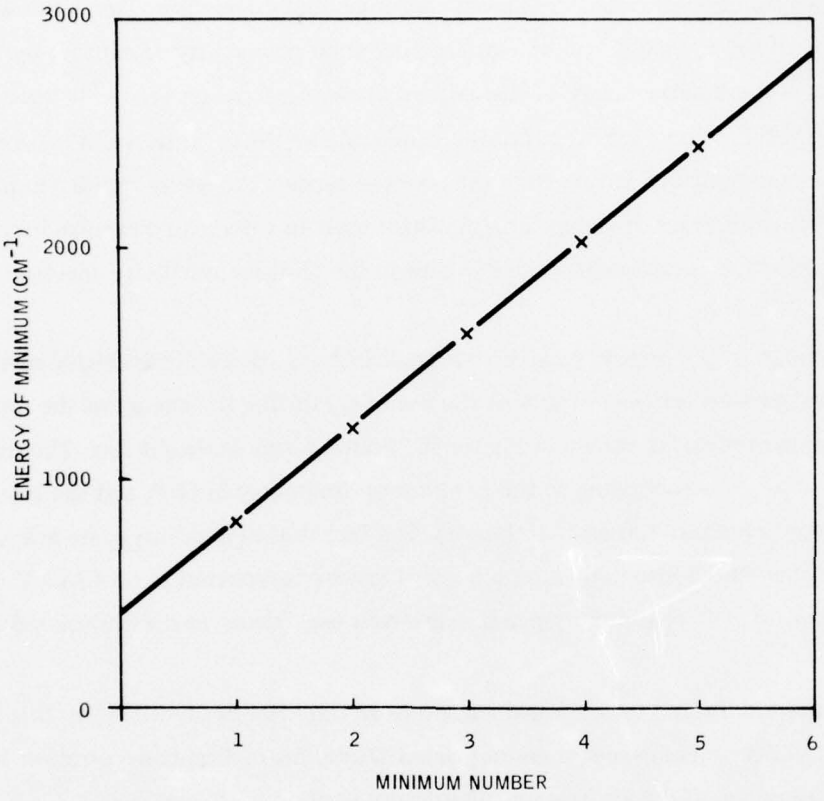


Figure 56. Energy of the photoconductivity minima as a function of the minimum number (the intercept at 400 cm^{-1} gives the impurity ionization energy).

4. Junction Capacitance Measurements

It is well known that the majority carrier impurity distribution can be determined from the bias dependence of the junction capacitance. The capacitance of a Schottky barrier on an n-type substrate varies with voltage according to the expression

$$\frac{1}{C^2} = 2(\phi_D + V)/(A^2 e\, \epsilon_o \epsilon)\, n\,(w) \qquad (10)$$

where A is the area of the junction, e the electron charge, ϵ_o is the permitivity of free space, ϵ the dielectric constant, $n(w) = N_d - N_a$ is the carrier concentration at the edge of the depletion width, ϕ_D is the junction diffusion potential and V the applied bias. Figures 46 and 47 showed $1/C^2$ versus V plots at room temperature for a Schottky barrier fromed on a SSD substrate and on an LPE layer. The linear dependence of the characteristics indicates that $N_d - N_a$ does not vary with distance throughout the depletion width of these junctions. For the SSD sample, the carrier concentration varied by about 12% and for the LPE layer by about 15%. Note that the slope of the $1/C^2$-V characteristic varies with the fourth power of the diameter of the diode, so small errors in determining the diameter have a large influence on the determination of the carrier concentration.

$1/C^2$ vs V was plotted in Figure 48 for two Schottky barriers on an angle-lapped surface of LPE-10-63. Diodes 1 and 2 are approximately 15 and 50 μm respectively, from the growth interface. Note that the carrier concentration increases with distance from the surface; i.e., the material near the surface is less compensated. This material was inadvertently grown over a large temperature range; the closer to the surface, the lower the growth temperature. This suggests, in agreement with our BSG Cu doping experiments, that more Cu is incorporated into GaP at higher than at lower temperatures. This is an expected result. The main purpose of presenting these results is to demonstrate the usefulness of C-V measurements for determining carrier concentrations.

Schottky barrier capacitance measurements can also be used for the study and characterization of deep levels in semiconductors. The manner in which deep levels can influence the junction capacitance is illustrated in Figure 57. This figure shows the equilibrium band bending and space charge density as a function of distance from the surface in a Schottky barrier formed on an n-type

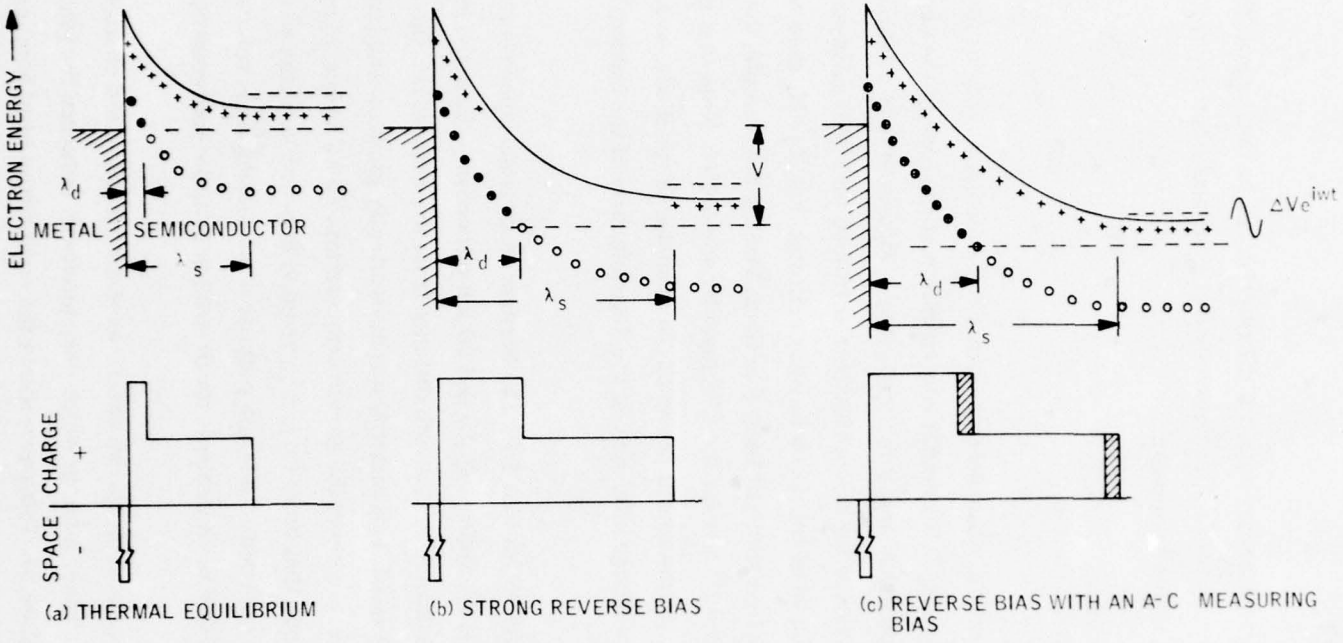


Figure 57. Band schematic of a Schottky barrier and the corresponding space charge distribution for three different bias conditions.

semiconductor with shallow and deep donor levels. When the junction is reversed biased, the space charge width, of course, widens with additional states, both shallow and deep, being ionized. The incremental space charge ΔQ which is introduced by an incremental change ΔV in the potential is shown in the shaded area of Figure 57. In general, the capacitance of a planar Schottky diode is given by $\epsilon\epsilon_o A/x_{cg}$, where ϵ is the low frequency dielectric constant. A the diode area and x_{cg} the center of gravity of the ΔQ distribution. Hence, if by altering the reverse bias voltage, the Fermi level can be moved through the deep defect level, and if the frequency of the ac measuring voltage is low enough so that the population of the deep levels can follow, the deep levels will affect, in some way, the junction capacitance.

As discussed above, we have utilized two techniques for deep level studies in GaP. The first is the admittance spectroscopy technqiue. Figure 49 shows the temperature dependence of the conductance for several frequencies in a Au/GaP Schottky diode which was fabricated on a BSG-4 substrate. The theory for this mechanism predicts that:

$$\frac{\omega}{T_{peak}^{3/2}} \simeq \exp\left(-\frac{E_t}{kT_{peak}}\right) \tag{11}$$

where T_{peak} is the temperature of the peak and E_t is the energy depth of the level below the conduction band. In Figure 58 we have plotted $(\omega)\,(T_{peak})^{-3/2}$ as a function of the reciprocal temperature for two samples. The slope of these data give $E_t \simeq 0.14$ eV. Note that one of the points does not fit the straight line. We have not identified the source of this defect.

With the admittance spectroscopy technique, we have not been able to identify any other levels in GaP than the one discussed above. In fact, we have encountered difficulty in reproducing results using this technique. We believe that the double-source photocapacitance DSP technique, the results of which are discussed below, is a more useful method for deep-level investigation in GaP. The DSP technique has recently been discussed by White, Dean, and Porteous[6].

---

[6] A. M. White, P. J. Dean and P. Porteous, J. Appl. Phys. 47, 3230 (1976).

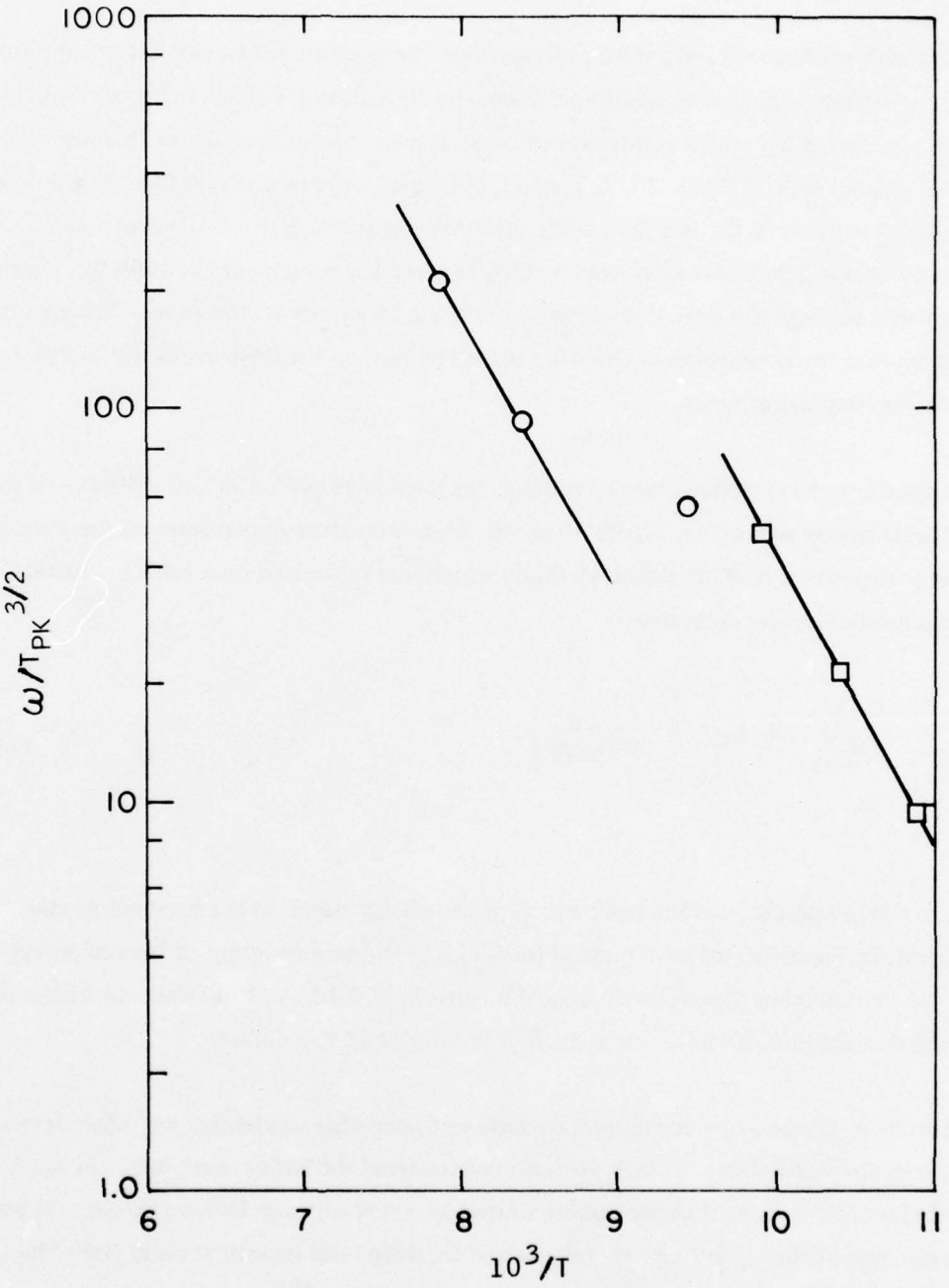


Figure 58. Frequency divided by (temperature)$^{3/2}$ as a function of reciprocal temperature for two Au/GaP Schottky Barriers.

Figure 50 shows the result of our measurement of change in capacitance of Schottky barriers formed on BSG substrates as a function of the probing radiation energy for three different measuring frequencies. These data can be interpreted by assuming a deep donor and a deep acceptor as is shown in Figure 59. The priming radiation acts to fill the donor levels with electrons and the deep acceptors with holes. When the probe radiation energy is between 0.4 and 0.6 eV, it acts to depopulate the electron traps with a resultant increase in capacitance. At frequencies less than 10^4 Hz and for probe radiation energy greater than 0.6 eV, the capacitance is decreased because the principal effect is to depopulate the hole traps. At the highest frequency (2×10^5 Hz), the capacitance increases monotonically with increasing probe radiation energy. This change in behavior, we believe, is due to the measuring frequency being too high for the deep acceptor to follow. Hence, this technique can be used to characterize both the energy location of the defect level and its time constant. Although intentional doping experiments have yet to be done to positively identify the levels, the deep acceptor is most likely Cu. The electron trap ($E < 0.4$) is not yet identified.

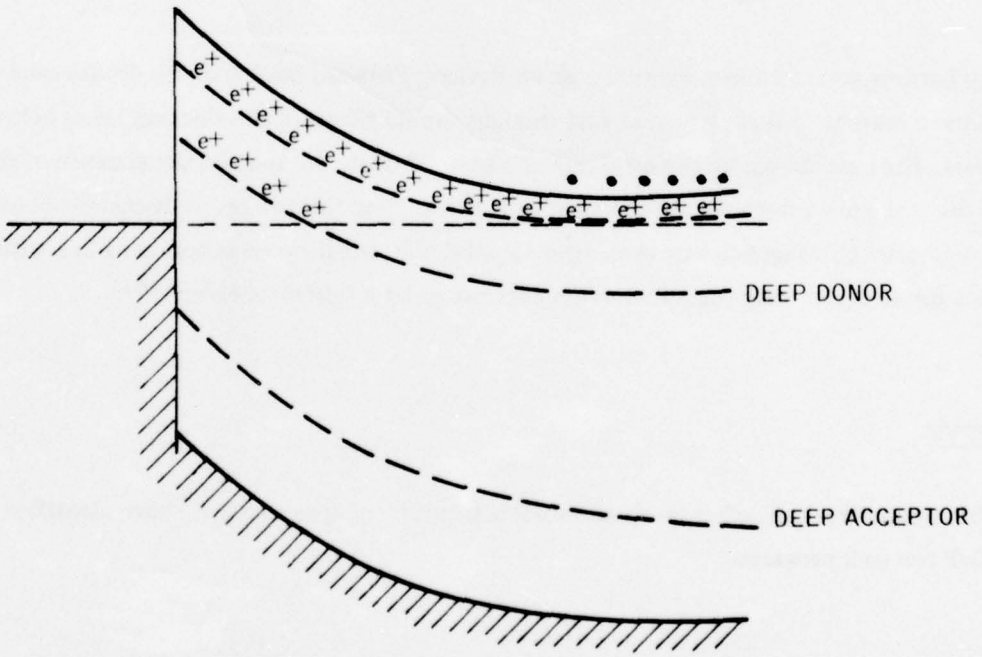


Figure 59. Equilibrium band schematic of a Schottky diode on an n-type substrate with deep donor and acceptor states.

The results of photocapacitance measurements on an LPE GaP:Cu layer are shown in Figure 51. When the sample is illuminated with greater than bandgap radiation, all transitions into and out of the defect levels are permissible. Hence, for each level some steady-state population will be achieved. The degree to which a center is filled or empty will depend on the capture cross-sections for the transition. The samples were cooled to 77 K so that after the radiation is turned off, the time for the deep levels to return to equilibrium is long. Consequently, some of the electron states below the Fermi level which in equilibrium would be filled are empty, and electrons can be optically excited from the valence band to these states. Introducing negative charge in the depletion region of an n-type sample will cause the capacitance to decrease while the introduction of positive charge will cause the capacitance to increase.

The data in Figure 51 show two distinct acceptor-like levels near 0.5 and 0.7 eV. The 0.7 eV level is the Cu acceptor which has also been detected by the optical quenching of photoconductivity. The 0.5 eV level is believed to be another Cu related acceptor state. We have also seen evidence of this level in the IR spectroscopy experiments.

Schottky barriers are, of course, majority carrier devices. Forward biasing of the diodes causes a large electron current to flow, which at first thought should fill all of the electron levels below the Fermi level. The data shown by the solid line in Figure 51 show the spectral dependence of the photocapacitance just after a forward current of 0.1 mA. Note the two levels discussed above are still detected. This suggests that even after forward bias, the deep acceptors are filled with holes either as a result of minority carrier injection currents or by a tunneling effect[dd].

5. Summary

Figure 60 summarizes the defect levels and their activation energies which we have identified in our GaP research program.

[dd] We wish to thank Professor C. T. Sah for helpful discussions in interpreting these data.

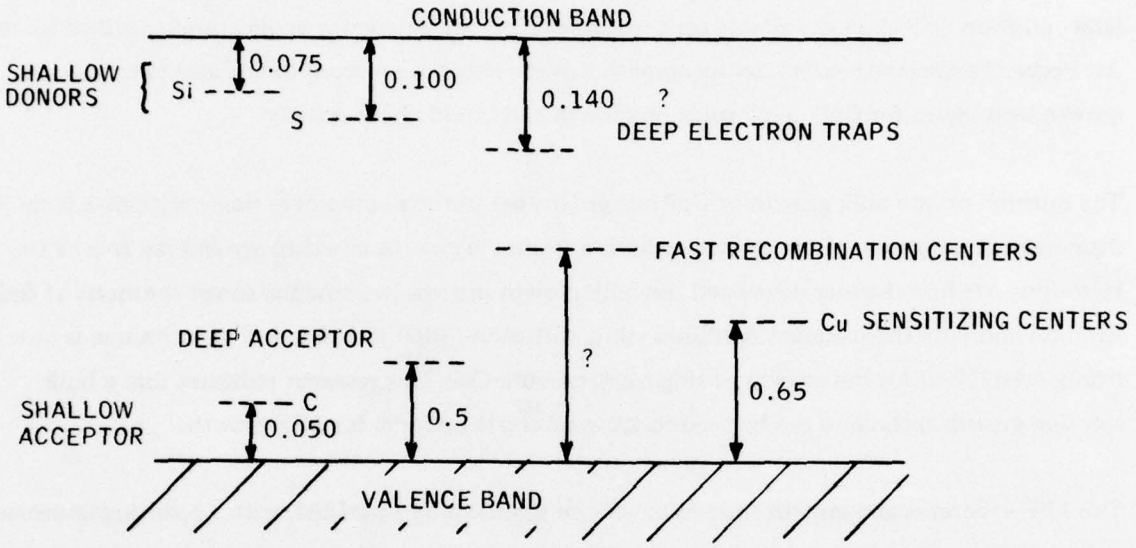


Figure 60. Defect levels in gallium phosphide.

SECTION V
PROGRESS AND ACCOMPLISHMENTS

The objective of this research effort was to develop a crystal growth program which could produce large, uniform GaP crystals suitable for the high-performance detector applications specified by the Air Force. As discussed earlier, to accomplish this objective, we elected to advance two solution growth techniques for GaP - bulk solution growth and liquid phase epitaxy.

The research on the bulk growth of GaP has progressed to the point where single crystals 1.0 cm in diameter can be grown. These crystals exhibit a favorable growth morphology and are free of Ga inclusions. We have further developed the bulk growth process to allow the direct synthesis of GaP from Ga and P by the so-called synthesis-solute-diffusion (SSD) technique. This technique is now firmly established for the growth of single-crystal bulk GaP. Our research indicates that a bulk solution growth technique can be used to grow substrate material for LPE growth.

The LPE apparatus and growth process have been significantly upgraded, with a resulting improvement in the quality of the grown layers. Large-area, high-gain, uniform photoconductors have been grown by this technique. The benefits which we anticipate from the further development of the solution growth processes for GaP have been largely realized.

Following is an abbreviated list of the significant accomplishments achieved during this program:

- Improved the LPE growth apparatus to achieve:
  - —Improved surface morphology
  - —Increased area of LPE layers to 5 mm x 12 mm.

- *Demonstrated* that sensitized Cu-doped GaP can be grown by LPE:
  - —Extended short-wavelength (0.25 μm) response observed on as-grown LPE GaP:Cu layers
  - —High sensitivity LPE GaP:Cu has been grown (photoconductive gains $10^4 \rightarrow 10^5$)
  - —Short response time (1→10 msec) observed in LPE GaP:Cu material
  - —Spatial uniformity of photoresponse $< \pm 10$ percent over 3 mm slit width.

Designed and constructed new growth apparatus for BSG:

—1.0-cm-diameter crystals grown by BSG technique

—Growth rate ~1 mm/day achieved

—Uniformity of majority carrier concentration in BSG GaP < 10 percent.

Developed SSD technique for the growth of GaP:

—1.2-cm-diameter crystals grown by this technique

—Uniformity of majority carrier concentration ~15%

—Low dislocation density ($\sim 10^3$ cm^{-2}) in some material.

Measured principal defects in GaP:Cu:

—Shallow donors

—Electron trap

—Shallow acceptors

—Deep acceptors.

Determined primary scattering mechanisms in GaP:C:

—Lattice scattering near room temperature

—Ionized impurity scattering near 77 K

—Impurity conduction near 30 K.

Advanced materials evaluation capability for GaP.

—Employed Fourier transform spectroscopy for defect studies in GaP

—Employed oscillatory photoconductivity for defect studies in GaP

—Utilized double source photocapacitance technique for deep level studies in GaP

—Developed van der Pauw and high resistivity capability for Hall and resistivity studies in GaP.

SECTION VI
REFERENCES

1. AFML-TR-76-79 Report "Advanced Development on Gallium Phosphide Materials for Satellite Attitude Sensors," Contract F33615-75-C-5244.

2. H. Nakatsuka, A. J. Domenico and G. L. Pearson, Solid-State Electron. 14, 849 (1971).

3. R. G. Schulze and P. E. Petersen, J. Appl. Phys. 45, 5307 (1974).

4. P. E. Petersen and R. G. Schulze, United States Patent No. 3,976,872, Gallium Phosphide Photodetector having an As-Grown Surface and Producing an Output from Radiation having Energies of 2.2 to 3.8 eV.

5. D. L. Lossee, J. Appl. Phys. 46, 2204 (1975).

6. A. M. White, P. J. Dean and P. Porteous, J. Appl. Phys. 47, 3230 (1976).

7. T. Iizuka, J. Electrochem. Soc. 118, 1190 (1971).

8. W. A. Brantley, O. G. Lorimor, P. D. Dapkus, S. E. Haszko and R. H. Saul, J. Appl. Phys. 46, 2029 (1975).

9. A. S. Jordan, A. R. Von Neida, R. Caruso and C. K. Kim, J. Electrochem. Soc. 121, 153 (1974).

10. A. Rose, Concepts in Photoconductivity and Allied Problems, Interscience, New York (1963).

11. J. S. Blakemore, Semiconductor Statistics, Pengamon Press, New York, (1962).

12. J. A. W. van der Does de Bye and R. C. Peters, Phillips Res. Repts. 24, 210 (1969).

13. D. L. Rode, Phys. Stat. Sol 53, 245 (1972).

14. T. Hara and I. Akasaki, J. Appl. Phys. 39, 285 (1968).

15. M. G. Craford, W. O. Groves, A. H. Herzog and D. E. Hill, J. Appl. Phys. 42, 2751 (1971).

16. L. R. Weisberg, J. Appl. Phys. 5, 1817 (1962).

17. H. C. Casey Jr., F. Ermanis and K. B. Wolfstirn, J. Appl. Phys. 40, 2945 (1969).

18. J. Bardeen and W. Shockley, Phys. Rev. 80, 72 (1950).

19. H. Ehrenreich, J. Phys. Chem. Solids 8, 130 (1959).

20. F. J. Blatt, Solid State Phys. 4, 344 (1957).

21. C. Erginsoy, Phys. Rev. 79, 1013 (1950).

22. J. D. Wiley and M. DiDomenico, Phys. Rev. B2, 427 (1970).

23. F. Thompson and R. C. Newman, J. Phys. C., S.S. Phys. 4, 3249 (1971).

24. W. Scott and J. R. Onffroy, Phys. Rev. 13, 1664 (1976).

25. W. Berndt, A. A. Kopylov and A. N. Pilchtin,JETP Lett. 22, 284 (1975).

26. R. A. Street and W. Senske, Phys. Rev. Lett. 37, 1292 (1976).

27. H. J. Stocker, H. Levinstein and C. R. Stannard, Phys. Rev. 150, 613 (1966).

APPENDIX A

PHOTOCONDUCTIVITY IN WIDE BANDGAP MATERIALS

There are two possible mechanisms for the enhancement of photoconductivity which occurs in n-type material when it is doped with a deep acceptor. The first is the sensitization which can occur if the recombination traffic is diverted through the added deep acceptor. We will refer to this mechanism as "sensitization by addition of recombination centers." The second mechanism is the enhancement which can occur if the added centers act only as minority carrier traps. We will refer to this as "sensitization by minority carrier trapping." In this section, we will compare these two photo-enhancement mechanisms.

1. SENSITIZATION BY THE ADDITION OF RECOMBINATION CENTERS.

Consider first recombination in a material with a single recombination center, labeled A in Figure A-1. N_A is the density of the A-centers. σ_A^e is the cross-section for electron capture by an empty A-center. σ_A^h is the cross-section for hole capture by a filled A-center. For sake of simplicity, we assume that the photo-induced carrier concentrations Δn and Δp are large compared to the equilibrium values.

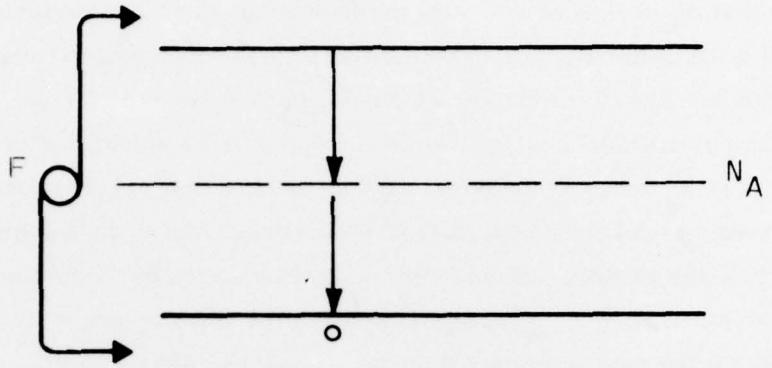


Figure A-1. Band schematic for a single combination center.

The rate equation for the electrons becomes:

$$\frac{d\Delta n}{dt} = F - (\Delta n)\,(N_A - n_A)\,\gamma_A^e \tag{1}$$

where F is the electron-hole generation rate and $\gamma_A^e = \sigma_A^e\,\nu_{th}^e$; ν_{th}^e = the electron thermal velocity. In the steady state:

$$\Delta n = F\,\tau_e,\ \tau_e = \frac{1}{(N_A - n_A)\gamma_A^e} = \left(\frac{\gamma_A^h + \gamma_A^e}{\gamma_A^e\ \gamma_A^h}\right) N_A^{-1} \tag{2}$$

Equation 2 requires that the density of recombination centers be small enough so that they do not affect the charge neutrality condition; i.e., $\Delta n = \Delta p$. Then, $\tau_e = \tau_h$ is constant and the photosignal varies linearly with photon flux.

Now we introduce a second set of recombination centers N_B with the characteristic $\sigma_B^e << \sigma_A^e$. We

now argue that introduction of these additional recombination centers can increase the majority carrier lifetime. It is not intuitively obvious that adding recombination centers can increase the majority carrier lifetime. The situation is depicted in Figure A-2. The B-centers are very deep and hence in the absence of radiation are filled with electrons. For levels of illumination such that the hole demarcation level E_d^h lies above the B-centers, they function only as hole traps. If the presence of the B-centers does not substantially affect the population of the A-centers, then for low levels of illumination, the majority carrier lifetime will not be altered by the presence of the B-centers. Later we will show how the B-centers can affect the majority carrier lifetime when acting as traps, but for this part of the discussion, we assume that effect is small.

As the light intensity is increased, the hole demarcation level moves downward toward the valence band. We now consider the situation where the demarcation level has moved through the B-centers. Therefore, the B-centers act as recombination centers rather than as hole traps. The allowed electron transitions for this situation are shown in Figure A-3.

Although we do not know the exact nature of the A-center, consider the following situation. The A-centers are neutral when empty; they carry a negative charge when filled with an electron. Consequently, σ_A^e is most likely $< \sigma_A^h$, where σ_A^e is the cross-section of an empty (neutral) A-center and σ_A^h is the cross-section for hole capture by a filled (negatively charged) A-center. The B-center when filled with electrons carries a double negative charge; it is singly negatively charged when it loses an electron (i.e., gains a hole). Because the B-center is negatively charged when it is occupied by a hole, $\sigma_B^e << \sigma_A^e$. In addition, assume that the density of the A-centers is much less than the density of the B-centers. Our assumptions thus far are:

$$\begin{aligned} \sigma_A^e &>> \sigma_B^e \\ \sigma_A^e &<< \sigma_A^h \\ N_B &>> N_A \end{aligned} \tag{3}$$

Before we calculate the lifetime, we should think through the process. Create electron-hole pairs. Because $\sigma_A^e >> \sigma_B^e$, as long as there are empty A-centers, the electrons will be captured primarily by the A-centers. The B-centers are all filled initially and are greater in density. Since all of the

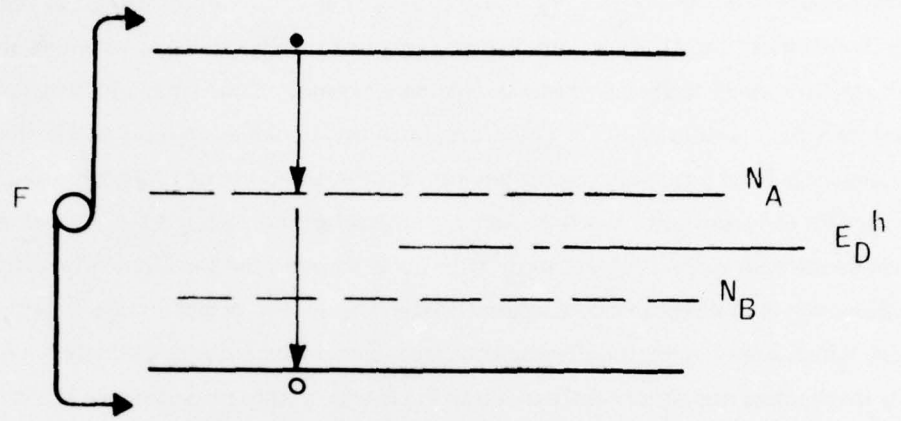


Figure A-2. Band schematic for a single recombination center and a single hole trap.

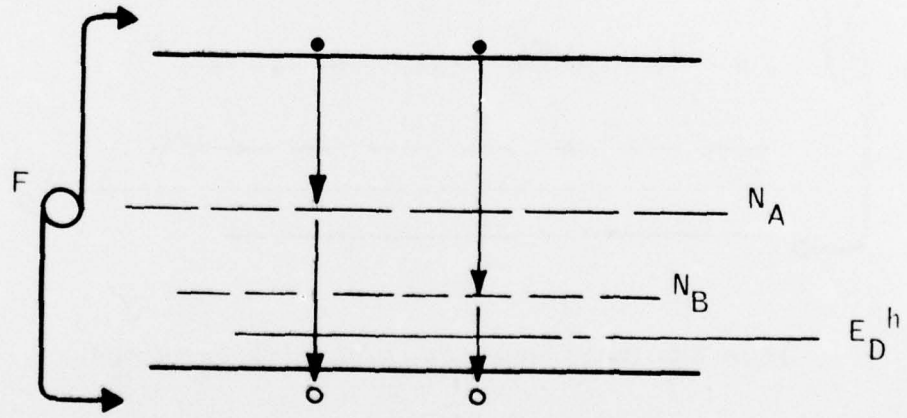


Figure A-3. Band schematic with two recombination levels.

B-centers are initially filled and $N_B >> N_A$ and $\sigma_B^h > \sigma_A^h$, most of the holes will go to the B-centers. Holes going to A-centers constitute recombination. On the other hand, holes which are captured by the B-centers are less likely to recombine with electrons because of the small cross-section which the B-centers have for electron capture. Therefore, once the demarcation level moves through the B-center, changing it from a trap to a recombination center, the B-centers fill with holes and the A-centers fill with electrons until the A-centers become saturated. After the A-centers are saturated, electrons then recombine primarily with holes through the B-centers. The effect of adding the B-centers is to block recombination through the A-centers and force recombination through the B-centers, which have a much smaller capture cross-section than do the A-centers. Since $\tau \propto \sigma^{-1}$, this mechanism can significantly increase the electron lifetime and hence the sensitivity. The situation after the A-centers are saturated is shown in Figure A-4.

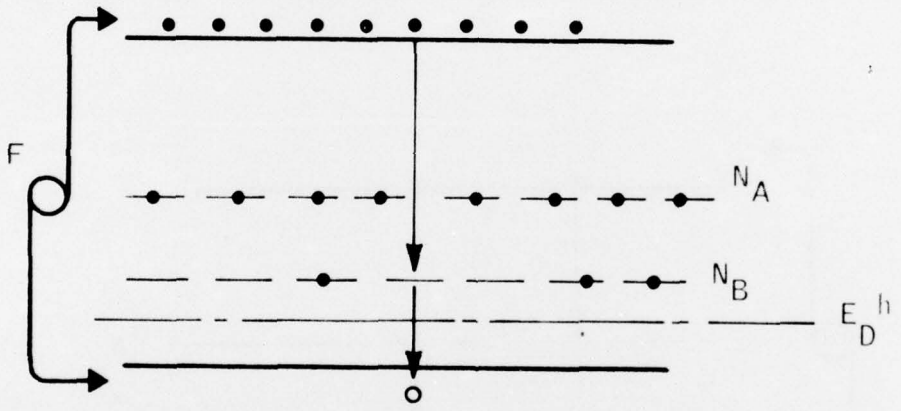


Figure A-4. Band schematic for a sensitized photoconductor.

We now present an analytical treatment similar to that of Rose to support the above model.

The rate of change of the electron density is:

$$\frac{dn}{dt} = F - (n)(N_A - n_A)\,\sigma_A^e v_{th} - (n)(N_B - n_B)\sigma_B^e v_{th} = F - \frac{n}{\tau_e^s} \qquad (4)$$

where τ_e^s is the lifetime for the sensitized case. Hence:

$$\tau_e^s = \frac{1}{\left[(N_B - n_B)\,\sigma_B^e v_{th}\right]\left[\frac{N_A - n_A}{N_B - n_B}\;\;\frac{\sigma_A^e}{\sigma_B^e} + 1\right]} \tag{5}$$

In the steady state, the rate at which electrons and holes are captured must be equal for both the A-centers and B-centers:

$$(n)\,(N_A - n_A)\;\sigma_A^e v_{th} = (p)\,(n_A)\;\sigma_A^h v_{th}$$

and

$$(n)\,(N_B - n_B)\;\sigma_B^e v_{th} = (p)\;(n_B)\;\sigma_B^h v_{th} \tag{6}$$

Equation 6 gives:

$$\frac{N_A - n_A}{N_B - n_B} = \left(\frac{n_A}{n_B}\right)\left(\frac{\sigma_A^h}{\sigma_B^h}\right)\left(\frac{\sigma_B^e}{\sigma_A^e}\right) \tag{7}$$

Now, as the A-centers saturate, as they must since $\sigma_A^e >> \sigma_B^e$ and $N_B > N_A$, $n_A \rightarrow N_A$ and $N_B - n_B \rightarrow N_A$. If the density of the B-centers is large, $n_B \simeq N_B$. These three approximations, along with Equation 7 when substituted into Equation 5, give:

$$\tau_e^{(s)}\;\;\frac{1}{\left[N_A\;\sigma_B^e\;v_{th}\right]\left[\frac{N_A\;\sigma_A^h}{N_B\;\sigma_B^h} + 1\right]} = \frac{1}{N_A\;\sigma_B^e\;v_{th}} \tag{8}$$

If the lifetime in the unsensitized case is given by Equation 2, then the ratio of the lifetime when sensitized to that when unsensitized is given by:

$$\frac{\tau_e^{(s)}}{\tau_e} = \frac{\sigma_A^e}{\sigma_B^e} \tag{9}$$

This ratio can be large (10^4 or greater) so the effect, according to this mechanism, of adding the B-centers as recombination centers can greatly enhance the photosensitivity.

2. SENSITIZATION BY MINORITY CARRIER TRAPPING

Consider now the situation where the B-centers act only as hole traps. The allowed electron transitions are shown in Figure A-2. In the steady state, the rate for the electrons is:

$$F = (\Delta n)\ (N_A - n_A)\ \gamma_A^e = \frac{\Delta n}{\tau_e} \tag{10}$$

As before, we have assumed $\Delta n \simeq n$ and $\Delta p \simeq p$. The steady-state equations for transitions into and out of the A-centers and B-centers respectively are:

$$(\Delta n)\ (\gamma_A^e)\ (N_A - n_A) = \Delta p\ \gamma_A^h\ n_A \tag{11}$$

and

$$\frac{\Delta p_B}{\Delta p} = \frac{N_B - \Delta p_B}{N_{v,B}} \simeq \frac{N_B}{N_{v,B}} \tag{12}$$

where $\Delta p_B = N_B - n_B$ and $N_{v,B}$ is the reduced density of states for the thermal transitions from

the B-centers to the valence band. The approximation in Equation 12 assumes that illumination is not strong enough to markedly change the population of the B-centers. If the density of the A-centers is low enough so that changes in n_A do not affect the charge neutrality condition, then:

$$\Delta n = \Delta p + \Delta p_B \tag{13}$$

Equation 10-13 are four equations with four unknowns. With a moderate amount of algebra, these equations can be solved to give:

$$\tau_e^m = \tau_e \left[1 + \left(\frac{\sigma_A^e}{\sigma_A^e + \sigma_A^h} \right) \left(\frac{N_B}{N_{v,B}} \right) \right] \tag{14}$$

where τ_e, given by Equation 2, is the lifetime where there are no B-centers present. We have assumed $\sigma_A^e << \sigma_A^h$. Therefore, Equation 14 shows that with the mechanism under consideration, enhancement of the majority carrier lifetime can occur if the following ratio is appreciable:

$$\left(\frac{\sigma_A^e}{\sigma_A^h} \right) \left(\frac{N_B}{N_{v,B}} \right)$$

3. COMPARISON OF THE TWO MECHANISMS

In order to facilitate this discussion, we retain the nomenclature used above; i.e., τ_e^s is the majority carrier lifetime when the B-centers act as recombination centers and τ_e^m is the lifetime when the B-centers act as hole traps.

Note first of all that τ_e^m is independent of photon flux. Therefore, for the situation where the B-centers act solely as hole traps, the photoconductive signal should vary linearly with photon flux. The photoconductive signal is given by I = GF, where:

$$G = \frac{\mu\tau V}{L^2} \tag{15}$$

where μ is the mobility, τ the lifetime, V the applied bias and L the contact spacing.

For the case where the B-centers can act as recombination centers, one has to consider three different regimes of photon flux intensity. For low levels of illumination, the hole demarcation level $E_D{}^h$ lies above the E_B level, the photoconductor is unsensitized and $\tau_e{}^s \rightarrow \tau_e{}^m$. As the flux intensity is increased, $E_D{}^h$ moves through E_B, and when $E_D{}^h$ lies below E_B, the photoconductor is fully sensitized and $\tau_e{}^s$ is given by Equation 8. If $\sigma_A{}^e >> \sigma_B{}^e$, $\tau_e{}^s$ can be much longer than τ_e^m. Hence, the photoconductive signal in the so-called sensitized regime is much larger than in the unsensitized regime. In both of these regimes, the lifetime is constant so the signal varies linearly with photon flux. In the transition region between these two regimes, the signal must vary superlinearly with photon flux. A schematic of these three regimes is shown in Figure A-5. This is the only model we know of which yields a superlinear dependence in the photosignal — photon flux characteristic.

Consider now the position in the energy band of the hole demarcation level. A hole located at the demarcation level has the same probability of recombining with a free electron as of being thermally excited to the valence band. By equating these two probabilities, one obtains:

$$(E_D{}^h - E_v) = (E_c - E_f{}^e) + kT\,\ell n\left(\frac{\sigma_B{}^h\ m_h}{\sigma_B{}^e\ m_e}\right) \tag{16}$$

where E_c and E_v are the energies at the conduction and valence band edges, $E_f{}^e$ is the electron quasi-fermi level and m_h and m_e represent the hole and electron effective mass, respectively. These levels are shown in Figure A-6. Note that there is a different demarcation level for each defect center. Note also that as the electron population increases, the quasi-fermi level moves toward the conduction band edge and the hole demarcation level moves correspondingly closer to the valence band. Consequently, for low resistivity material, the demarcation level can lie near the valence band edge. In order to estimate the importance of the cross-section-dependent term in Equation 16,

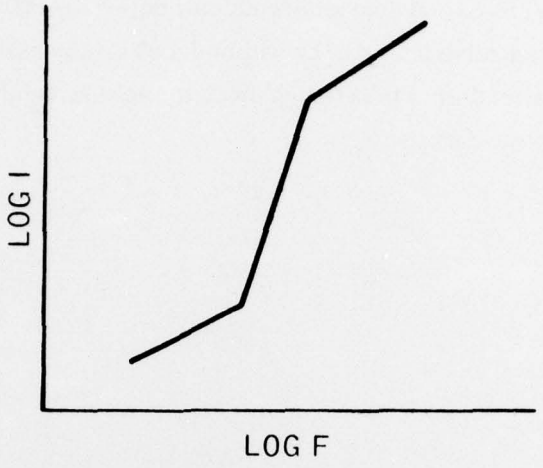


Figure A-5. Photocurrent versus photon flux intensity for a sensitized photoconductor.

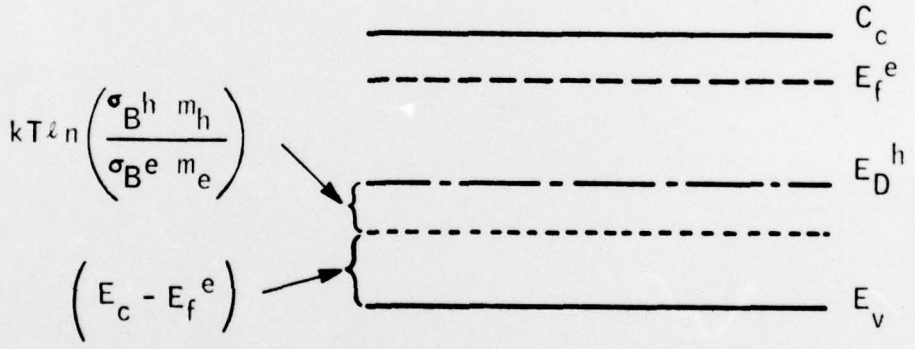


Figure A-6. Band schematic showing electron and hole demarcation levels.

assume that $m_h = m_e$ and $\sigma_B{}^h/\sigma_B{}^e = 10^3$. For these values and for $T \simeq 300$ K, the second term of Equation 16 equals 0.17 eV. For a GaP-like semiconductor doped to $\sim 10^{15} cm^{-3}$ and with $\sigma_B{}^h/\sigma_B{}^e = 10^3$, the hole demarcation level will lie within 0.4 eV of the valence band. Hence, for moderate doping levels, all centers deeper than 0.4 eV from the valence band will act as recombination centers, even in the dark.

☆ U. S. GOVERNMENT PRINTING OFFICE: 1977 — 757-001/525